

Structural and Dynamical Crossovers in Dense Electrolytes

Daehyeok Kim^a, Taejin Kwon^{b,†}, and Jeongmin Kim^{c,*}

^aDepartment of Energy Engineering, Korea Institute of Energy Technology (KENTECH), Naju 58330, Republic of Korea

^bDepartment of Chemistry and Cosmetics, Jeju National University, Jeju 63243, Republic of Korea

^cDepartment of Chemistry Education and Graduate Department of Chemical Materials,
Pusan National University, Busan 46241, Republic of Korea

(†tjkwon@jejunu.ac.kr)

(*jeongmin@pusan.ac.kr)

(Dated: January 19, 2026)

Electrostatic interactions fundamentally govern the structure and transport of electrolytes. In concentrated electrolytes, however, electrostatic and steric correlations, together with ion–solvent coupling, give rise to complex behavior, such as underscreening, that remains challenging to explain despite extensive theoretical effort. Using molecular dynamics simulations of primitive electrolytes with and without space-filling solvent particles, we elucidate the structural and dynamical crossovers and their connection that emerge with increasing salt concentration. Explicit-solvent electrolytes exhibit a screening transition from a charge-dominated dilute regime to a density-dominated concentrated regime, accompanied by dynamical crossovers in ion self-diffusion and ion-pair lifetimes. These dynamical crossovers display a marked discontinuity, unlike the smoother variation of the screening crossover, which originates from short-range ion–counterion structures. The pronounced growth of ionic clusters leads to a percolation transition only at higher concentrations, whereas the onset of the structural and dynamical crossovers is associated primarily with local ion pairing or small aggregates. Both structural and dynamical behaviors are found to depend sensitively on ion–solvent coupling: implicit-solvent electrolytes exhibit a screening transition between two charge-dominated regimes, accompanied by qualitatively distinct dynamical behavior. Finally, we demonstrate that the diffusion-corrected ion-pair lifetime provides a consistent descriptor linking ionic structure and dynamics across electrolyte systems.

I. INTRODUCTION

Electrolytes are indispensable in diverse systems spanning energy storage and conversion [1–9], environmental processes [10–13], and biological functions [14–16]. Understanding of their physicochemical properties at the molecular level is therefore essential for the development of advanced and next-generation electrolytes. At sufficiently low salt concentrations (typically below $\sim 0.1 \text{ mol}\cdot\text{L}^{-1}$ for aqueous monovalent electrolytes), the Debye–Hückel (DH) theory [17, 18] provides a successful description based mainly on electrostatic interactions among point ions embedded in a uniform dielectric-continuum solvent. However, as the salt concentration increases, deviations from DH behavior emerge due to ion–ion correlations, excluded-volume effects, and ion–solvent coupling; such complex interplay challenges a molecular-level understanding of concentrated electrolytes [19–21].

Underscreening [22–25] represents one of the most intriguing anomalies in concentrated electrolytes, which emerges as a result of competition between electrostatic and steric interactions. Recent surface force balance (SFB) experiments [22, 24, 25] have investigated electrostatic screening across a wide range of electrolytes and concentrations [26–31]. These studies revealed that concentrated electrolytes exhibit a longer electrostatic decay length (λ_s) with higher concentration, in contrast to the prediction of the DH theory, and in some cases λ_s reaches up to $\sim 10 \text{ nm}$, significantly exceeding the Debye screening length λ_D . A clear crossover between dilute to concentrated regimes was found when λ_D becomes comparable to the mean ion size a , with underscreening primarily observed in the concentrated regime. A phenomenon was previously predicted as the Kirkwood crossover [32]. Re-

markably, in the concentrated regime, a universal scaling relation was identified across chemically diverse electrolytes when normalized appropriately:

$$\left(\frac{\lambda_s}{\lambda_D} \right) \sim \left(\frac{a}{\lambda_D} \right)^\alpha, \quad (1)$$

where the scaling exponent $\alpha = 3$ in the SFB experiments. The intriguing scaling relation still lacks a clear physical origin, as many bulk simulations [29, 33, 34] and theoretical studies [30, 35, 36] have reproduced similar screening crossovers, albeit with consistently underestimated exponents ($\alpha \approx 1–2$).

In addition to the structural features, understanding and predicting the dynamic behavior of concentrated electrolytes remain equally challenging. Theoretical approaches, such as mean-spherical approximation (MSA) [37, 38] and stochastic density functional theory (sDFT) [39–41], have extended the classical Debye–Hückel–Onsager theory [42, 43] by incorporating steric ion–ion interactions. Recent applications of sDFT [41, 44, 45] have reported encouraging agreement with experimental trends in the transport properties of moderately concentrated aqueous electrolytes. Nevertheless, a subsequent study [46] indicated that the quantitative accuracy of these predictions may be limited by compensating effects among different theoretical contributions. However, a unified microscopic understanding that consistently connects ion dynamics and electrostatic screening remains elusive, seeking to establish a direct connection between structure and dynamics. That is, how microscopic ion and solvent organization governs macroscopic transport properties, such as electrical conductivity and diffusion.

The formation of ionic clusters, as a result of structural correlations, plays a crucial role in determining ion transport

in concentrated electrolytes by governing correlations in ion motion [47–50]. A striking example is water-in-salt electrolytes [2, 51], where nanoscale phase separation emerges into a salt-rich domain that enhances interfacial stability and a water-rich domain that facilitates lithium-ion transport. The emergence of nanoscale ionic organization has also been observed in model electrolytes [52–55]. Such nonideality becomes particularly significant in nonaqueous electrolytes with low dielectric permittivity, where electrostatic correlations dominate over the thermal fluctuations. These ionic clusters contribute differently to the total ionic conductivity, depending on their diffusivity [50, 56, 57]. With increasing salt concentration, ion association proceeds through the progressive linking of ion pairs into extended networks [58–60]. When the connectivity of these networks spans the entire system, a system-spanning ionic structure emerges, often referred to as percolation or gelation in the context of polymer physics [60–64]. The percolation of ionic domains was also suggested to be closely related to the cubic scaling (Eq. 1 with $\alpha = 3$) observed in SFB experiments [65, 66]. These findings motivate the need to further investigate how percolation in ionic structures, and its onset, relate to potential structural and dynamical crossovers in concentrated systems.

In this work, we employ molecular dynamics simulations of primitive electrolytes with both explicit and implicit solvents to elucidate the relationships between structural and dynamical correlations in dense ionic fluids across a wide range of salt concentrations. Primitive models are chosen because, despite their simplicity, they have proven successful in capturing essential features of electrostatic screening and ionic organization [36, 50, 67–70]. While explaining the microscopic origin of the cubic scaling is beyond the scope of this study, our primary focus is to clarify the mechanistic connections among electrostatic screening, ionic clustering, and charge transport in dense ionic environments.

We identify dynamic crossovers in ion self-diffusion and ion-pair dynamics that accompany the screening crossover and can be unified by scaling with the ratio of the mean ion size to the Debye screening length, as used in the SFB measurements. The nature of the screening crossover depends sensitively on explicit-solvent packing: explicit-solvent systems transition from a charge-dominated dilute regime to a density-dominated concentrated regime, whereas implicit-solvent systems undergo a transition between two charge-dominated regimes. Although enhanced ion–ion correlations promote a percolation transition in ionic clustering, we find that this percolation is not directly coupled to either screening or dynamical crossovers. Instead, it correlates more strongly with ion density, reflecting that percolation requires sufficiently extensive aggregation to form a system-spanning network and therefore typically occurs only at higher salt concentrations, whereas the onset of underscreening is associated with the emergence of local ion pairing or small aggregates. The dynamical crossovers exhibit a marked discontinuity, linked to qualitative changes in short-range ion–counterion structure. Finally, we identify the diffusion-corrected ion-pair lifetime as a unified microscopic descriptor that consistently bridges ionic structure and transport across electrolyte mod-

els.

The remainder of this paper is organized as follows. In Section II, we describe the simulation models and methods, detailing the procedures for calculating structural and dynamical properties as well as identifying ionic clusters. Section III presents the results and discussion of the coupled crossovers of electrostatic screening and dynamic properties, including ion self diffusion and ion-pair lifetime, highlighting the diffusion-corrected ion-pair lifetime as a unified basis for both explicit-solvent electrolytes over a wide range of salt concentration. We also examine the decoupling of the percolation transition from both structural and dynamical crossovers. Finally, Section IV provides concluding remarks.

II. SIMULATION METHODS AND MODEL SYSTEMS

A. Model electrolytes

We consider model electrolytes consisting of neutral LJ solvent particles and ion particles, all of the same size and of the same mass (m) [71]. The particles interact via the LJ and Coulomb interactions. All LJ interactions (U_{LJ}) for solvent and ion particles were truncated and shifted at a cutoff distance r_c .

$$U_{LJ}(r) = 4\epsilon \left[\left(\frac{\sigma}{r} \right)^{12} - \left(\frac{\sigma}{r} \right)^6 - \left(\frac{\sigma}{r_c} \right)^{12} + \left(\frac{\sigma}{r_c} \right)^6 \right], \quad (2)$$

assuming the same LJ energy ϵ , and diameter σ for interactions between all types of particles. Two cutoff distances are chosen: $r_c = 2.5 \sigma$ and 1.222σ . In the former case, both attractive and repulsive LJ interactions are considered, while only the repulsive interactions (WCA) are considered in the latter case. In this study, electrolytes employing cutoff distances of $r_c = 2.5 \sigma$ and 1.222σ are referred as "LJ" and "WCA", respectively. In contrast, the Coulomb interaction (U_C) between the ions is identical across all electrolyte systems, and is given by:

$$U_C(r) = \frac{1}{4\pi\epsilon_0\epsilon_s} \frac{q_i q_j}{r} = k_B T Z_i Z_j \frac{l_B}{r} \quad (3)$$

where ϵ_0 is the vacuum permittivity, and l_B denotes the Bjerrum length with k_B being the Boltzmann constant and T being the temperature. l_B varies with the uniform background dielectric constant ϵ_s , ranging between 0.2 and 5 in this work. The LJ ions are monovalent, *i.e.*, valency $Z_\alpha = 1$ for all ionic species α , carrying either $q_\alpha^* = eZ_\alpha/\sqrt{4\pi\epsilon_0\sigma\epsilon} = +1$ or -1 . Here, the asterisk represents a quantity in reduced LJ units. Regardless of the LJ cutoff r_c , $U_C(r)$ is split into two contributions: The short-range contribution is cut at $r = 3.5 \sigma$, and the long-range contribution is calculated using the particle-particle and particle-mesh (PPPM) method with the Ewald screening parameter chosen for a fixed cutoff distance in order to achieve a given relative error in forces (10^{-4} in this work). All computations were performed in the $N_{\text{solv}}N_{\text{salt}}p^*T^*$ ensemble at $p^* = p\sigma^3/\epsilon = 1$ and $T^* = Tk_B/\epsilon = 1$, which corresponds to a liquid phase [72, 73]. The number of solvent

particles, N_{solv} , was fixed at 5000, while the number of salt pairs, N_{salt} , varied according to solution concentration unless otherwise noted.

During equilibrium MD, the equations of motion were integrated using the velocity Verlet integrator with a timestep $\delta t^* = \delta t \sqrt{\epsilon(m\sigma^2)^{-1}} = 0.001$. The desired pressure $p^* = 1$ and temperature $T^* = 1$ were maintained using the Nosé-Hoover barostat and thermostat, with time constants of 1000 and 100 LJ units, respectively. For each condition, we obtained at least ten independent trajectories starting from different initial states, from which statistical averages and errors were computed.

Implicit-solvent models. As a limiting case to examine explicit space-filling solvent effects, we performed Langevin dynamics (LD) simulations, implemented in LAMMPS [74, 75], for electrolyte systems without explicit solvent particles. The ions interact via the same interaction potentials and were assigned identical LJ parameters, charges, and masses as in the explicit-solvent model. Long-range electrostatic interactions and all other simulation settings were kept identical to those used in the explicit-solvent systems. The friction coefficient was determined from the diffusion coefficient obtained in the explicit-solvent simulations at the smallest salt-to-solvent ratio ($r_{\text{salt}} = 0.01$) and was kept constant throughout all LD simulations. All LD simulations were carried out in the canonical ensemble, with the box size chosen to match the average volume of the equilibrated explicit-solvent systems at each condition, and with the identical temperature maintained at $T^* = 1.0$. We note that the ions in the explicit and implicit solvent models do not follow the same equation of state, which, however, is not the primary focus of the comparison between the two solvent models. We also note that, in concentrated LJ electrolytes, the ions undergo phase segregation [70] when explicit solvent particles are absent. Therefore, only low-concentration cases that show no phase segregation are included in our analysis (see Fig. S7 in the SM [76]).

B. Computation of observables

Structural correlation functions. We investigated the short- and long-range ion structures by computing the radial distribution function (RDF).

$$g_{\alpha\beta}(r) = \frac{\langle V \rangle}{4\pi r^2 N_\alpha N_\beta} \sum_{i,j \neq i} \langle \delta(r - |\vec{r}_i^\alpha - \vec{r}_j^\beta|) \rangle, \quad (4)$$

where $\langle V \rangle$, and N_α denote the average volume of a simulation cell, the number of ionic species α , respectively: the subindices α and $\beta \in \{+, -, s\}$. \vec{r}_i^α represents the position vectors of i^{th} particle of species α . Here, $\langle \dots \rangle$ denotes the ensemble average.

Using the ion-ion RDFs, we also calculated the density-density ($g_{NN}(r)$) and charge-charge ($g_{ZZ}(r)$) correlation function as follows,

$$g_{NN}(r) = \sum_{\alpha} \sum_{\beta} \chi_{\alpha} \chi_{\beta} g_{\alpha\beta}(r), \quad (5)$$

$$g_{ZZ}(r) = \sum_{\alpha} \sum_{\beta} q_{\alpha} q_{\beta} \chi_{\alpha} \chi_{\beta} g_{\alpha\beta}(r), \quad (6)$$

where χ_{α} denotes the number fraction of the ionic species α , respectively. For the 1:1 symmetric electrolytes in the present study, $\chi_{\alpha} = 1/2$ for any species α . We note that $g_{NN}(r \rightarrow \infty) \rightarrow 1$, while $g_{ZZ}(r \rightarrow \infty) \rightarrow 0$. These systems exhibit the charge inversion symmetry, and therefore the charge-density coupling is strictly zero: $g_{ZN}(r) = \sum_{\alpha} \sum_{\beta} q_{\alpha} \chi_{\alpha} \chi_{\beta} g_{\alpha\beta}(r) = \frac{\epsilon}{4} [g_{++}(r) + g_{+-}(r) - g_{-+}(r) - g_{--}(r)] = 0$.

In a range of salt concentrations, an oscillatory exponential function describes the decay of the total correlation functions $h(r)$ at long distances [33, 34]:

$$h(r) \approx A \cdot r^{-1} \exp\left(-\frac{r}{\lambda}\right) \cdot \cos\left(\frac{2\pi r}{l} + \phi\right). \quad (7)$$

Here, the first term represents the Yukawa-type exponential decay characterized by the decay length λ , while the second term captures the oscillatory modulation with amplitude A , phase ϕ , and period l . The total correlation function $h(r)$ corresponds to $h_{ZZ}(r) = g_{ZZ}(r)$, $h_{NN}(r) = g_{NN}(r) - 1$, $h_{s+}(r) = g_{s+}(r) - 1$, or $h_{ss}(r) = g_{ss}(r) - 1$, ensuring $h(r \rightarrow \infty) \rightarrow 0$. In our analysis, each structural correlation function was approximated by a single Yukawa-type decay. In principle, however, multiple decay modes may coexist according to the dressed-ion theory [77–81].

Regarding electrostatic interactions, the exponential term dominates $h_{ZZ}(r)$ in sufficiently dilute electrolytes ($\lesssim 0.1 \text{ mol L}^{-1}$), consistent with Debye–Hückel theory, where the decay length satisfies $\lambda_Z \approx \lambda_D$, with λ_D being the Debye screening length:

$$\lambda_D = \sqrt{\frac{1}{8\pi l_B c_{\text{salt}}}}. \quad (8)$$

In contrast, the oscillatory component of $h_{ZZ}(r)$ becomes prominent at high salt concentrations owing to the strong ion–ion correlations [33]. In this work, we refer to the transition between these two regimes as the electrostatic screening crossover.

In a similar manner, the density-density total correlation $h_{NN}(r)$ was analyzed. The dominant length scale is determined by the longest decay length, not by the presence of the oscillation [33, 68].

Ionic clusters and gelation. We analyzed ionic clusters by constructing an undirected graph $G = (V, E)$ from the instantaneous ionic configuration at a given time using networkX [82]. Each ion $i \in V$ is represented as a node located at position \vec{r}_i , and an edge $(i, j) \in E$ is assigned between ions i and j if their separation is less than a cutoff distance r_c . In other words, we define ionic clusters using a distance-based connectivity. In this work, $r_c = 1.5\sigma$, taken from the first minimum of $g_{+-}(r)$. The ionic clusters are then identified as the connected components of the graph G , where each cluster consists of ions linked through the edges. The size s of a cluster is defined as the sum of the numbers of constituent cations n_+ and anions

n_- : $s = n_+ + n_-$. The charge inversion symmetry in the model electrolytes imposes $n_+ = n_-$.

We analyzed the size distribution of ionic clusters as a function of salt concentration, modeled by an exponential distribution with a power-law tail [61]:

$$P(s) \approx \frac{1}{N_s} s^{-\gamma_s} \cdot \exp\left(-\frac{s}{\xi_s}\right). \quad (9)$$

The normalization constant N_s ensures $\sum_s P(s) = 1$. This analysis is analogous to the scaling approaches used in critical phenomena [60, 83, 84]. Two characteristic length scales, ξ_s and γ_s , describe different parts of the distribution: the former governs the exponential decay, while the latter characterizes the power-law tail. Their relative contributions change across the percolation (or *gelation*) transition. In the pre-gel regime, the exponential part dominates, corresponding to small, localized ion clusters. At the gelation point, $P(s)$ reduces to a pure power-law distribution, implying the emergence of a scale-free ionic network spanning the simulation box. In the post-gel regime, the percolating ionic network coexists with small clusters. Additional analysis of ionic clusters, including association patterns and comparison to the Cayley-tree-based ionic gelation theory [31, 60, 63, 85, 86], is provided in the SM [76].

Ion-pair lifetime. To quantify the lifetime of ion pairs, we computed the ion-pair survival function $H_{\alpha\beta}(t)$ using MD analysis package [87, 88]:

$$H_{\alpha\beta}(t) = \langle h_{ij}^{\alpha\beta}(t) h_{ij}^{\alpha\beta}(0) \rangle, \quad (10)$$

where $h_{ij}^{\alpha\beta}(t)$ is an indicator function defined such that $h_{ij}^{\alpha\beta}(t) = 1$ if ions i of species α and j reside within a certain distance r_h at time t , and 0 otherwise. Here, ions i and j belong to species α and β , respectively. In this work, we used the same distance cutoff (1.5σ) to define neighboring ion pairs at each time. $H_{\alpha\beta}(t)$ follows a stretched exponential function: $H_{\alpha\beta}(t) \approx \exp[-(t/\tau_H)^{\beta_H}]$, where τ_H is a characteristic time constant, and β_H is a stretching exponent. The mean ion-pair lifetime was then estimated as $\tau_{\text{pair}} = \int_0^\infty t H_{\alpha\beta}(t) dt = \tau_H \Gamma(1/\beta_H)/\beta_H$ with Γ denoting the Gamma function.

Diffusion. We computed diffusion of ion and solvent particle using the mean-squared displacement (MSD) $\Delta\vec{r}_{\alpha\beta}(t)$ ($\alpha, \beta \in \{+, -, s\}$): $\Delta\vec{r}_{\alpha\beta}(t) \equiv \langle \Delta\vec{r}_i^\alpha(t) \cdot \Delta\vec{r}_j^\beta(t) \rangle$, where $\Delta\vec{r}_i^\alpha(t)$ ($= \vec{r}_i^\alpha(t) - \vec{r}_i^\alpha(0)$) denotes the displacement of the i^{th} ion of species α during time t [89, 90]. The corresponding diffusion coefficient $D_{\alpha\beta}$ was obtained in the long-time limit where the MSD grows linearly with time.

$$D_{\alpha\beta} = \lim_{t \rightarrow \infty} \frac{\Delta\vec{r}_{\alpha\beta}(t)}{6t}. \quad (11)$$

In this work, we focused on the self-diffusion ($\alpha = \beta$), where the MSD of each species grows linearly with time within the simulation window (see Sec. S7 in the Supplemental Material (SM) [76]). Thanks to the charge inversion symmetry, we used $D_{\text{ion}} = (D_{++} + D_{--})/2 = D_{++} = D_{--}$. Using $D_{\alpha\beta}$, we also estimated the characteristic diffusion timescale over

which an ion diffuses, on average, a distance comparable to its diameter: $\tau_{\text{diff}} = \frac{\sigma^2}{6D_{\text{ion}}}$ [91].

III. RESULTS AND DISCUSSION

In this section, we primarily present the simulation results for the explicit-solvent electrolytes up to Sec. III D, where they are compared with the implicit-solvent models. Results for all other models are provided in the SM [76].

Solvent structure. Figure 1(A) shows the inverse relationship between salt concentration, c_{salt} , and the solvent concentration, c_{solv} , as a function of N_{salt} , clearly illustrating the steric effects in dense electrolytes. Here, $c_{\text{salt}} = N_{\text{salt}}/\langle V \rangle$ and $c_{\text{solv}} = N_{\text{solv}}/\langle V \rangle$, where $\langle \dots \rangle$ denotes the average system volume with $\langle \dots \rangle$ denoting the ensemble average.

In the model systems studied, the non-electrostatic interaction strongly modifies the solvent organization: LJ systems exhibit more pronounced peaks in $g_{ss}(r)$ than WCA systems, indicative of stronger short-range correlations among solvent particles (Figs. 1(B) and 1(C)). At long distances, the decay length λ_s of $\ln(|r \cdot h_{ss}(r)|)$ also differs significantly: $\lambda_s \approx \sigma$ for LJ electrolytes, while it is halved ($\lambda_s \approx \sigma/2$) for WCA ones. Nevertheless, the solvent structures in both systems are largely insensitive to variations in ϵ_s and c_{salt} . We note that the ion-solvent interaction is also different in LJ and WCA systems.

A. Structural crossover from a charge-dominated dilute regime to a density-dominated concentrated regime with c_{salt}

The decay of charge-charge correlations (Figs. 2(A) and 2(B)) reveals that two distinct regimes emerge for both LJ and WCA electrolytes with varying c_{salt} , similar to those reported in previous studies [36, 68, 92]. $\ln(|r \cdot h_{ZZ}(r)|)$ follows a simple exponential decay in the dilute regime with low c_{salt} , and its decay length λ_Z decreases with c_{salt} , being $\lambda_Z \approx \lambda_D$, consistent with Debye–Hückel theory [93]. Beyond a threshold salt concentration ($a\lambda_D^{-1} \gtrsim 1$), however, the oscillatory contribution to $\ln(|r \cdot h_{ZZ}(r)|)$ emerges. This threshold marks a screening crossover between the dilute and concentrated regimes. While the mean-field theories such as Debye–Hückel theory describes the dilute regime well, it breaks down in the concentrated regime, where strong electrostatic and steric correlations become significant. In the concentrated regime, the so-called underscreening takes place: λ_Z increases with c_{salt} , exceeding λ_D [25, 29]. We note that most simulation results, including ours, exhibits the concurrent emergence of underscreening and oscillations in $\ln(|r \cdot h_{ZZ}(r)|)$, in clear contrast to the purely exponential decay of surface forces measured in SFB experiments [28]; the oscillatory features are often regarded as signatures of *overscreening* [94, 95].

Figure 2(C) summarizes our results for both LJ and WCA electrolytes, which reproduce the electrostatic screening crossovers observed in SFB experiments, yet yield underestimated scaling exponents ($\alpha \approx 1.5–2$). Notably, the range of measured λ_Z extends only up to $\sim 10 \lambda_D$, whereas

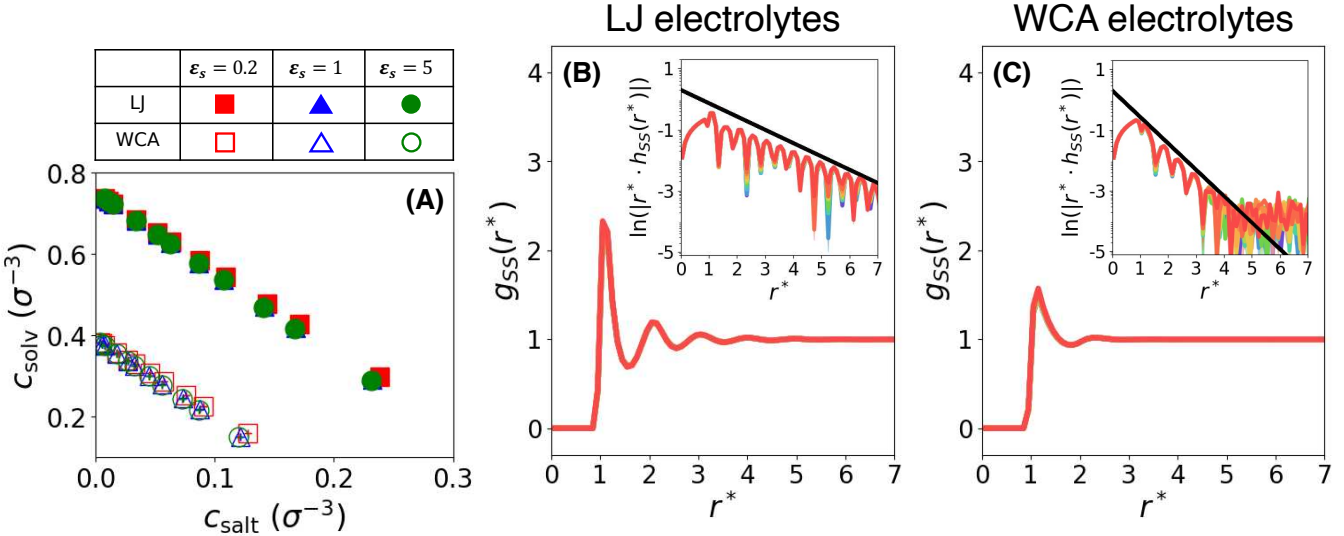


FIG. 1. Space-filling solvent effects. (A) Dependence of solvent concentration (c_{solv}) and salt concentration (c_{salt}) on the number of salt pairs N_{salt} , with the number of solvent particles fixed at $N_{\text{solv}} = 5000$. (B) Solvent–solvent radial distribution function $g_{\text{ss}}(r)$ for LJ electrolytes and (C) for WCA electrolytes. In both cases, the results collapse onto a single curve across all c_{salt} . Insets show the distinct decay behavior of $g_{\text{ss}}(r)$, with black solid lines indicating decay lengths $\lambda_s = 1 \sigma$ and $\sigma/2$, respectively. In this work, “LJ” and “WCA” refer to electrolytes with and without Lennard–Jones attractive interactions (Eq. 2), corresponding to cutoff distances of $r_c = 2.5 \sigma$ and 1.122σ , respectively.

anomalous underscreening in SFB experiments has been reported to reach $\sim 100 \lambda_D$. Consistent with previous bulk molecular simulations [29, 33, 34] and classical DFT studies [30, 35, 36], this underestimation leaves the physical basis of the experimental scaling unresolved, a discrepancy that persists across both chemically detailed models and coarse-grained systems such as primitive electrolytes. Recent studies [53, 68, 96] have further suggested that confinement- or interface-induced effects, including enhanced ion association, may contribute to the anomalous cubic scaling observed in SFB experiments, but investigating these effects is beyond the scope of the present study.

The LJ electrolytes exhibit strong density–density correlations across all c_{salt} , evidenced by the oscillatory exponential decay of $\ln(|r h_{\text{NN}}(r)|)$ (Fig. 2(D)), in marked contrast to the Debye–Hückel assumption that $g_{\text{NN}}(r) = 1$ at all distances. For $c_{\text{salt}} \gtrsim 0.0343 \sigma^{-3}$ ($r_{\text{salt}} = 0.05$), both the decay length and the oscillation period remain nearly constant, with $\lambda_N \approx \sigma$ and $l_N \approx \sigma/2$, largely independent of c_{salt} . The WCA electrolytes also exhibit oscillatory behavior (Fig. 2(E)), though with comparatively weaker oscillations. Non-electrostatic attractions strongly influence long-range density packing, as reflected in the decay lengths: at all c_{salt} , the WCA systems show $\lambda_N \approx \sigma/2$, approximately half of that in the LJ systems. This trend is consistent with the long-range decay of the solvent structure $h_{\text{ss}}(r)$ (Fig. 1). In contrast, the oscillation period of $h_{\text{NN}}(r)$ remains largely unchanged regardless of attractive interactions, consistent with that of $h_{\text{ss}}(r)$: $l_N \approx l_s \approx \sigma/2$. Overall, these results underscore the crucial role of solvent packing and, more broadly, ion-solvent coupling in determining the structural organization of ions.

The comparison of the decay lengths (λ_N versus λ_Z ,

Fig. 2(F)) shows that both explicit-solvent electrolytes exhibit a structural crossover at $a/\lambda_D \approx 1$, from a charge-dominated dilute regime ($\lambda_Z \gtrsim \lambda_N$) to a density-dominated concentrated regime ($\lambda_Z \lesssim \lambda_N$). This transition is consistent with previous predictions from a hard-sphere ion–solvent mixture (HISM) at high solvent density [97] and from simulations of primitive models with a variable solvent dielectric function [70]. Our results further confirm these predictions: in the density-dominated regime, most decay lengths collapse onto a common value, except for λ_Z . Supporting this, the oscillatory decays of $h_{\text{ss}}(r)$ give $\lambda_{\text{ss}} \approx \sigma$ in the LJ systems and $\lambda_{\text{ss}} \approx \sigma/2$ in the WCA systems (see Fig. S6 in the SM [76]). Taken together, these structural signatures highlight the significant influence of ion–solvent coupling across concentration regimes and its strong dependence on the non-electrostatic interactions.

B. Formation of a percolating ionic network is not directly coupled to the structural crossover

In an attempt to examine a connection between the screening crossover and the formation of a percolating ionic network, we quantify the growing size of ionic clusters with increasing c_{salt} due to increased ion-ion correlations (Figs. 3). In defining an ionic cluster, a pair of a cation and an anion belongs to the same cluster if their interionic distance is within the cutoff distance $r_{\text{cut}} = 1.5 \sigma$ taken from the first minimum of $g_{+-}(r)$ (see Figs. S10 and S14–S15 in the SM [76]). Due to the charge symmetry in the systems of interest, the numbers of constituent cations n_+ and anions n_- of an ionic cluster are the same. We characterize the ionic clusters by their

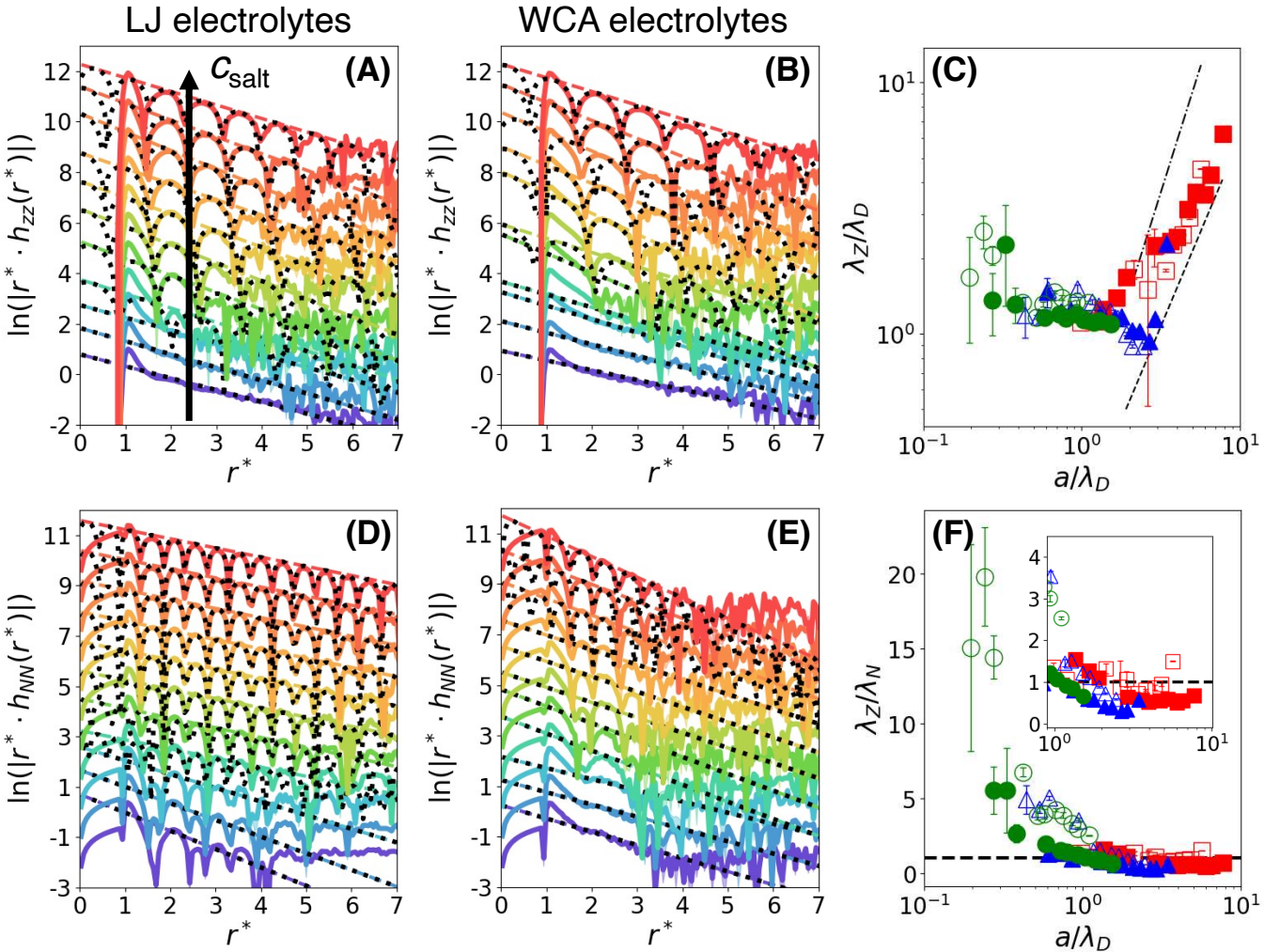


FIG. 2. Crossover in structural correlations of explicit-solvent electrolytes. (A) Charge–charge correlation functions, $\ln(|r \cdot h_{ZZ}(r)|)$, for LJ electrolytes with $\epsilon_s = 0.2$, and (B) the corresponding results for WCA electrolytes. (C) Decay length λ_Z of $h_{ZZ}(r)$ as a function of a/λ_D , where a is the ion size and λ_D is the Debye screening length (Eq. 8). Black dash-dot ($\alpha = 2$) and dashed ($\alpha = 1.5$) lines serve as visual guides to the scaling behavior described in Eq. 1. (D) Density–density correlation functions, $\ln(|r \cdot h_{NN}(r)|)$, for LJ electrolytes with $\epsilon_s = 0.2$, and (E) the corresponding results for WCA electrolytes. (F) Ratio of decay lengths, λ_Z/λ_N , as a function of a/λ_D . The black dashed horizontal line indicates $\lambda_Z/\lambda_N = 1$. The inset shows a magnified view of the transition region. In panels (A–B, D–E), c_{salt} increases with the color changing from purple to green to red. Panels (C) and (F) present results across all explicit-solvent systems examined in this study, with the colors and markers consistent with those in Fig. 1. Structural correlation functions and their corresponding fitting results for the other systems are provided in the SM [76].

size distribution $P(s)$ (Fig. 3 and Tab. I). Two characteristic length scales (γ_s and ξ_s in Eq. 9) describe different parts of the distribution: the former governs the exponential decay, while the latter characterizes the power-law tail. At sufficiently low c_{salt} , $P(s)$ is well described by the exponential part alone with its decay length ξ_s . Far below the threshold salt concentration (the pre-gel regime), γ_s increases with c_{salt} as more ionic clusters form, while the contribution of the power-law tail grows with γ_s , approaching the threshold. At the threshold concentration c_{gel} , $P(s)$ follows a pure power-law distribution, indicating the emergence of a scale-free ionic *network* spanning the simulation box. This threshold corresponds to the gelation or percolation point ($c_{\text{salt}} \approx 0.063 \sigma^{-3}$ for LJ electrolytes with

$\epsilon_s = 0.2$). In the post-gel regime, the power-law tail diminishes with increasing salt concentration, as a larger fraction of ions participates in the spanning network, thereby reducing the relative contribution of small ionic clusters.

Despite the intriguing c_{salt} dependence of $P(s)$, the formation of an ionic network does not appear to be strongly correlated with the screening crossover (Fig. 3(B)). Instead, the emergence of a percolating network seems to be primarily governed by the spatial proximity of ions, as it occurs even in relatively dilute electrolytes (e.g., $\epsilon_s = 5$), with gelation taking place at a similar transition concentration, c_{gel} (Tab. I). Therefore, the screening crossover appears to be decoupled from the ionic network formation in these solvent-dense con-

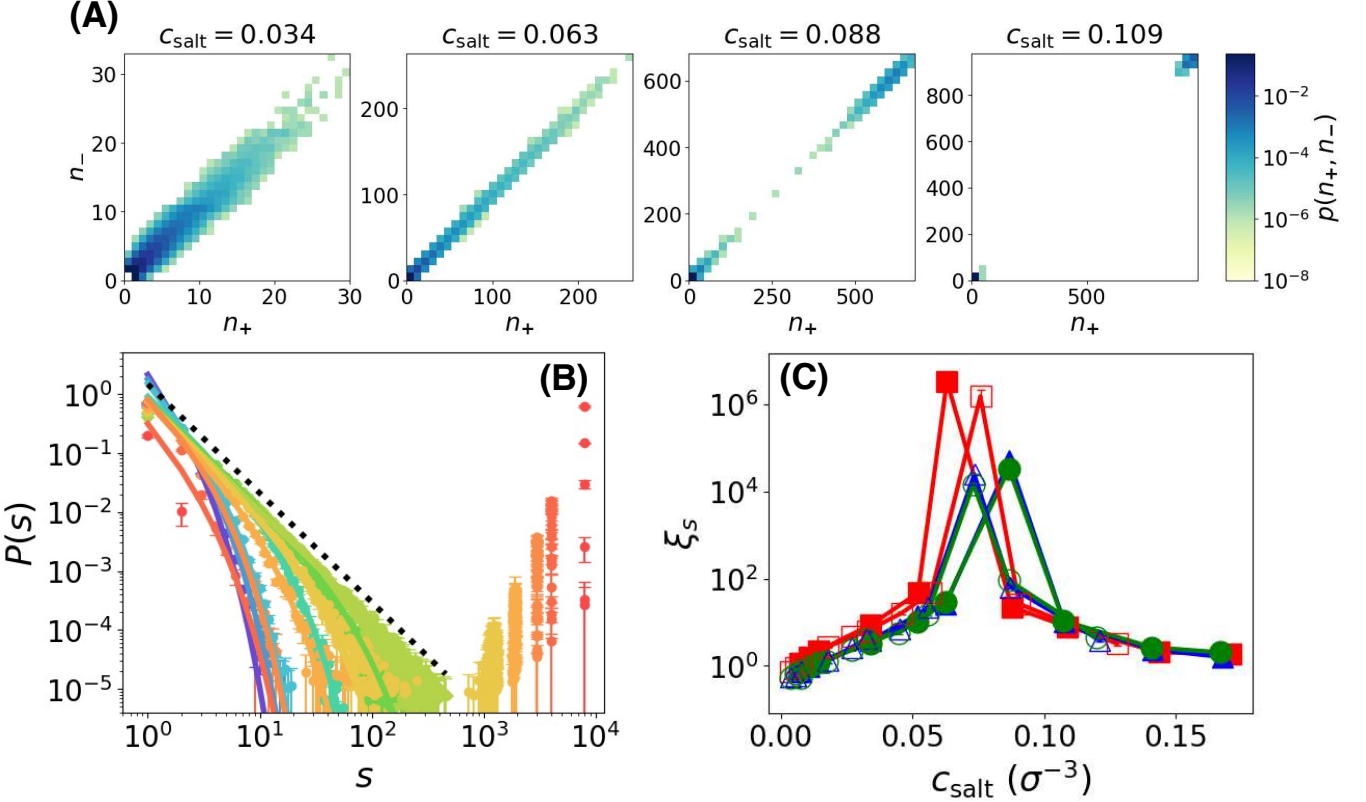


FIG. 3. Percolation transition of ionic clusters in explicit-solvent electrolytes. (A) Evolution of ionic clusters with salt concentration c_{salt} . The composition of each cluster is defined by the number pair (n_+, n_-) . (B) Size distribution $P(s)$ (Eq. 9) of ionic clusters with $s = n_+ + n_-$. c_{salt} increases with the color changing from purple to green to red. The black dotted line indicates the power-law decay at the percolation threshold, $c_{\text{gel}} \approx 0.063 \sigma^{-3}$, $P(s) \sim s^{-1.85}$. Panels (A) and (B) show results for explicit-solvent LJ electrolytes with $\varepsilon_s = 0.2$. (C) Dependence of the exponential decay length ξ_s , extracted from $P(s)$, on salt concentration c_{salt} across all explicit-solvent electrolytes. In all subpanels of panel (A), the probability at the point $(n_+, n_-) = (0, 0)$ is zero; the apparent non-zero value indicated by the dark blue color arises solely from the finite binning used in constructing the heat map. In panel (C), the colors and markers are consistent with those in Fig. 1.

System	ε_s	$c_{\text{gel}} (\sigma^{-3})$	$\gamma_s(c_{\text{gel}}) (\sigma)$
LJ	5	0.087	1.84 ± 0.03
LJ	1	0.087	1.84 ± 0.05
LJ	0.2	0.063	1.85 ± 0.01
WCA	5	0.073	1.85 ± 0.06
WCA	1	0.074	1.89 ± 0.07
WCA	0.2	0.076	1.97 ± 0.01

TABLE I. Formation of a percolating ionic network near the gelation point, c_{gel} , in the explicit-solvent electrolytes. The exponent $\gamma_s(c_{\text{gel}})$ quantifies the power-law tail of the size distribution, $P(s)$ (see Eq. 9 and Fig. 3(B)).

centrated electrolytes. This decoupling can be rationalized by the distinct physical requirements of the two phenomena: percolation requires sufficiently extensive aggregation to form a system-spanning network and thus typically occurs only at higher salt concentrations, whereas the onset of underscreening is associated with the emergence of local ion pairing or small aggregates. We note that the emergence of a percolating network, in general, provides a structural basis for strong correlations in ionic motion [60, 62–64]. Recent studies [65, 66]

have further suggested its relation to the cubic scaling observed in SFB experiments. In connection with the growing ionic domains, two competing length scales were introduced—the screening length, defined in terms of renormalized charges, and the average cluster size, which increases up to the percolation threshold—whose larger value is proposed to govern the scaling behavior.

The Cayley-tree-based ionic gelation theory [31, 60, 63, 85, 86] provides a theoretical framework for describing ionic clusters in concentrated electrolytes at the mean-field level, thereby linking structural changes—particularly gelation—to other physical properties. This framework has been successfully applied to a range of concentrated electrolytes, including (diluted) ionic liquids and their electrochemical interfaces. A key assumption of the theory is that ions form Cayley-tree clusters among other possible morphologies, such as chains, rings, and branched ionic aggregates. In contrast, owing to the simplicity of our electrolyte models, which employ isotropic interaction potentials between all ions and solvent particles, the resulting association patterns are more complex than ideal Cayley-tree-like structures (see Figs. S30-S31 in the SM [76]), particularly owing to the presence of co-ion associ-

ations and intra-cluster loops. These deviations, together with ambiguities in defining the ion-association functionality - a crucial input parameter of the theory - hinder the theory from accurately locating the gelation threshold c_{gel} of our simple models over the estimated counterion-association functionality range of 2-5.

Similar limitations of the ionic gelation theory have been reported previously; for example, theoretical predictions of gelation points were found to be systematically lower than those estimated from simulations for nonaqueous LiPF_6 and LiBF_4 electrolytes, a discrepancy likewise attributed to deviations from ideal Cayley-tree clusters [63]. Nevertheless, we find that below c_{gel} the ionic gelation theory captures the counterion association constant reasonably well, yielding values of comparable order of magnitude to those observed in simulations when an appropriate ion-association functionality is chosen (see Fig. S32 in the SM [76]). A detailed analysis and discussion of ionic association, together with its comparison with the ionic gelation theory, are provided in Sec. S10 of the SM [76].

C. Dynamic crossover of ion self-diffusion and ion-pair lifetime

We examine c_{salt} -dependent dynamic properties, including ion self-diffusion and ion-pair lifetime across the structural crossover from the charge-dominated dilute regime to the density-dominated concentrated regime. In particular, the dynamic properties are organized with respect to the ratio a/λ_D , in the same manner as for the structural correlations, enabling a systematic investigation across a wide range of c_{salt} (top row of Fig. 4). This representation is also consistent with the Debye–Hückel–Onsager (DHO) and DFT theories [39, 41, 44], where a/λ_D serves as a physically meaningful variable for describing ionic transport.

Figure 4(A) displays the diffusion relaxation time defined by ion self-diffusion, $\tau_{\text{diff}} = \sigma^2/6D_{\text{ion}}$, which exhibits crossover behavior (see Fig. S19(A,D) for ion self-diffusion coefficients D_{ion} in the SM [76]). It is clear that plotting the results against a/λ_D is better than c_{salt} for systematic comparison (see Fig. S19 in the SM [76]). Ions in the LJ electrolytes diffuse approximately four times more slowly than those in the WCA electrolytes, as expected from the increased viscosity arising from non-electrostatic attractive interactions (see Fig. S18 for solvent diffusion coefficients in the SM [76]). The relaxation time τ_{diff} exhibits a discontinuous change across the crossover. When $a\lambda_D^{-1} \lesssim 1$, τ_{diff} depends only weakly on c_{salt} (green and blue markers in Fig. 4), whereas in the concentrated regime, strong ion–ion electrostatic interactions further suppress ion diffusion, as clearly demonstrated for $\epsilon_s = 0.2$ (red markers in Fig. 4). In the concentrated WCA electrolytes with $\epsilon_s = 0.2$, the ratio $D_{\text{ion}}/D_{\text{solv}}$ decreases noticeably, implying a breakdown of the Stokes–Einstein relation (see Fig. S19(C, F) in the SM [76]).

A clear crossover is also observed in the ion-pair lifetime τ_{pair} when plotted against a/λ_D (Fig. 4(B)). The lifetime was estimated using the ion-pair survival function $H(t)$

(Eq. 10, see Figs. S23 and S24 in the SM [76]). Both dilute LJ and WCA electrolytes exhibits the nearly constant lifetime of cation–anion pairs, independent of both c_{salt} and ϵ_s . Upon entering the concentrated regime, however, this behavior changes markedly with a notable discontinuity. For both LJ and WCA electrolytes with $\epsilon_s = 0.2$, τ_{pair} decreases at a fast rate, i.e., a rapid decay of $H(t)$ with increasing c_{salt} despite the enhanced ion–ion correlations and increased viscosity. The short-lived nature of ion pairs is often presumed to manifest the formation of an ionic network that enables frequent partner exchange [50, 63, 98]. Whereas ion pairs in dilute electrolytes can persist until they encounter other pairs or free ions, the dense ionic environment in concentrated systems can promote facile partner exchange without compromising the integrity of the network [50].

Instead of being indirectly linked to the percolating ion network, these dynamic crossovers are more directly encoded in the underlying ion structures at short distances, particularly in the potential of mean force between cations and anions: $\beta w_{+-}(r) = -\ln[g_{+-}(r)]$ (see Fig. S14, S15 in the SM [76]). Each minimum in $w_{+-}(r)$ corresponds to a distinct solvation state of the ion pair, such as contact, solvent-shared, solvent-separated, or separated ones [99–101]. Thus, the profile of $\beta w_{+-}(r)$ represents the free-energy landscape governing ion-pair association and dissociation, which can be viewed as a barrier-crossing process [102]. The non-electrostatic attractive interactions result in a clear distinction in $w_{+-}(r)$ between LJ and WCA electrolytes, similar to the differences observed in $g_{NN}(r)$ and $g_{ss}(r)$: $w_{+-}(r)$ is more structured in LJ systems at short distances. Despite this difference, both LJ and WCA electrolytes exhibit $w_{+-}(r)$ that remains largely insensitive to c_{salt} in the dilute regime ($\epsilon_s = 1$ and 5).

In contrast, in the density-dominated concentrated regime ($\epsilon_s = 0.2$), $w_{+-}(r)$ becomes strongly dependent on c_{salt} . This dependence is most clearly reflected in the free energy barrier ΔF between the first and second solvation states of the ion pair (Fig. 4(C)). While ΔF remains nearly constant in dilute electrolytes, it progressively decreases with increasing c_{salt} in concentrated electrolytes, driven by pronounced ion–ion correlations. The reduction in $\beta\Delta F$ accelerates the cation–anion dissociation, leading to a shorter τ_{pair} . Notably, the barrier itself also exhibits a discontinuity between the dilute and concentrated systems, as observed in τ_{pair} and τ_{diff} . These trends are consistently observed for both LJ and WCA electrolytes.

In the case of ionic conductivity σ (see Sec. S9 in the SM [76] for the results and computational details), it is more appropriately represented as a function of c_{salt} because of the differences in l_B , as conventionally employed following the DHO theory and its extensions [44, 103]. Across all explicit-solvent systems, σ exhibits no turnover; instead, it increases monotonically with increasing c_{ion} within the range examined. This observation indicates that the screening crossover does not necessarily result in a decrease in ionic conductivity. The monotonic behavior of σ primarily reflects the relatively modest changes in D_{ion} with c_{salt} across the crossover (Fig. 4).

The ionicity $\sigma/\sigma_{\text{NE}}$ exhibits an intriguing c_{salt} dependence, quantifying the degree of correlated ion motion (see Fig. S29 in the SM [76]). Unlike the ionic conductivity, $\sigma/\sigma_{\text{NE}}$ is bet-

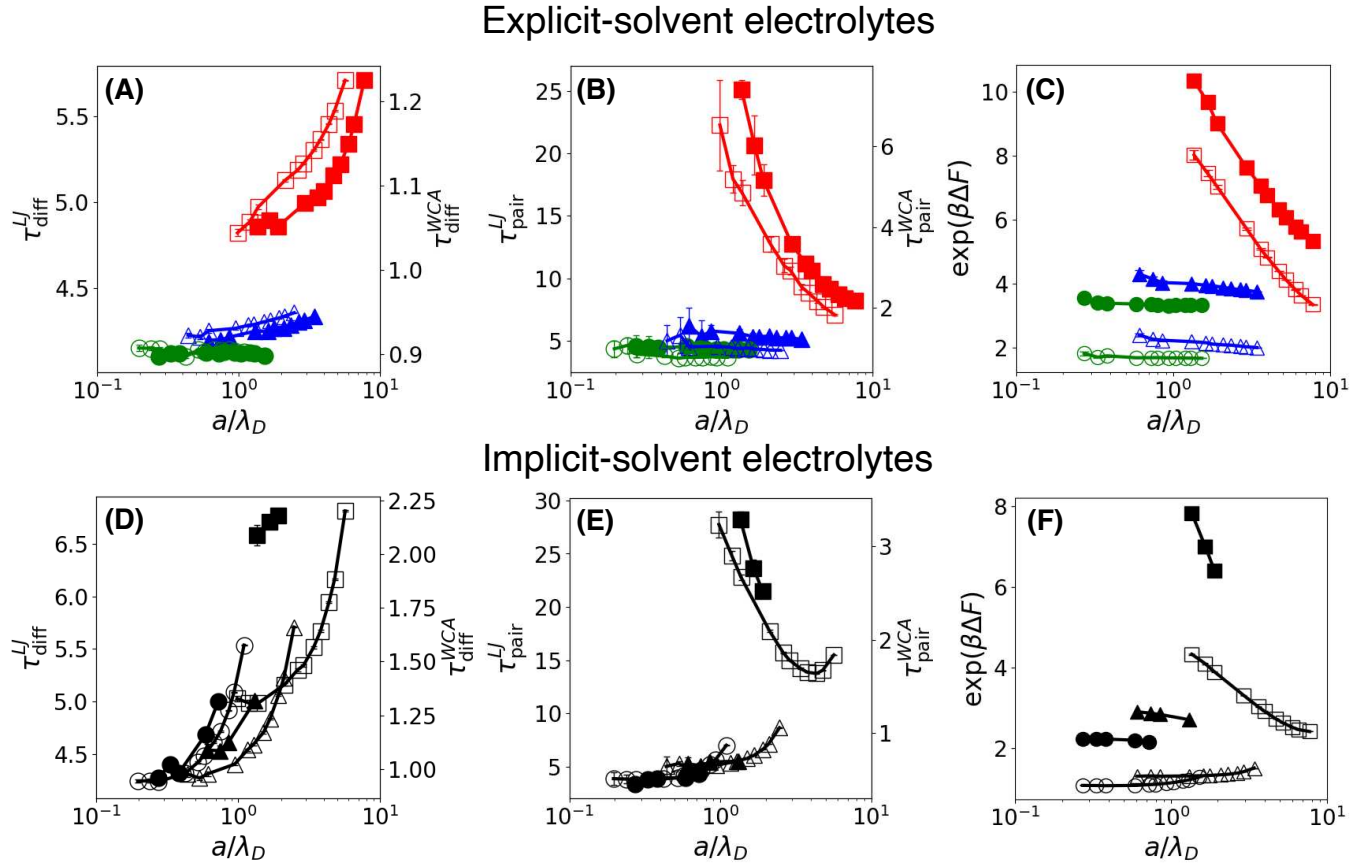


FIG. 4. Crossovers in ion dynamics and their structural origins as a function of the ratio a/λ_D across all electrolytes examined. (A, D) Diffusion relaxation time, τ_{Diff} . (B, E) Mean ion-pair lifetime, τ_{pair} . (C, F) Free-energy barrier for ion-counterion dissociation, $\beta\Delta F$. Panels (A–C) on the top row correspond to explicit-solvent models, while panels (D–F) on the bottom row correspond to implicit-solvent models. In panels (A–B) and (D–E), the left and right axes represent results for LJ (filled markers) and WCA (open markers), respectively. For the LJ electrolytes, the colors and markers are consistent with those in Fig. 1, and the black counterparts correspond to the WCA electrolytes.

ter represented with a/λ_D than with c_{salt} , clearly showing that it gradually decreases from unity to ~ 0.5 as the screening crossover is approached. This decrease indicates the breakdown of the Nernst-Einstein approximation due to dynamic correlations, particularly through the ion-counterion association. The ionicity appears to remain nearly constant in the concentrated regime, with no further decrease or upturn observed within the c_{salt} window examined. Overall, this behavior reflects enhanced dynamic correlations and collective ion motion with increasing c_{salt} , arising from the growth of underlying structural correlations.

D. Screening crossover between two charge-dominated regimes in implicit-solvent electrolytes

To examine the effects of strong solvent-ion coupling, we performed Langevin dynamics (LD) simulations without explicit, space-filling solvent particles as a limiting case. The implicit-solvent models successfully reproduce the essential ion-ion structural features observed in the explicit-solvent systems at both short and long distances (see Sec. S4 in the

SM [76]). As in the explicit-solvent models, differences in non-electrostatic attractions account for the variations in short-range ion structure: WCA ions display minimal short-range density correlations in $g_{NN}(r)$, whereas LJ ions exhibit pronounced short-range structuring, indicative of the onset of phase segregation [70]. Consequently, because $h_{NN}(r)$ does not exhibit a well-defined exponential or oscillatory exponential decay in these cases, λ_N could not be extracted for some implicit-solvent systems.

In the absence of explicit solvent, a similar screening crossover also emerges (Fig. 5(A)), with a slight difference in the scaling exponent in Eq. 1, consistent with predictions from classical density functional theory [30]. However, the screening transition occurs between two charge-dominated regimes—from a dilute to a concentrated one in the implicit-solvent WCA systems with $\epsilon_s = 0.2$. This is evidenced by the ratio $\lambda_Z/\lambda_N > 1$ (Fig. 5(B)), in clear contrast to the behavior observed in the explicit-solvent systems (Fig. 2(F)). This difference underscores the role of ion–solvent coupling in the screening transition, consistent with previous theoretical predictions [97].

Ion dynamics also show notable differences depending on

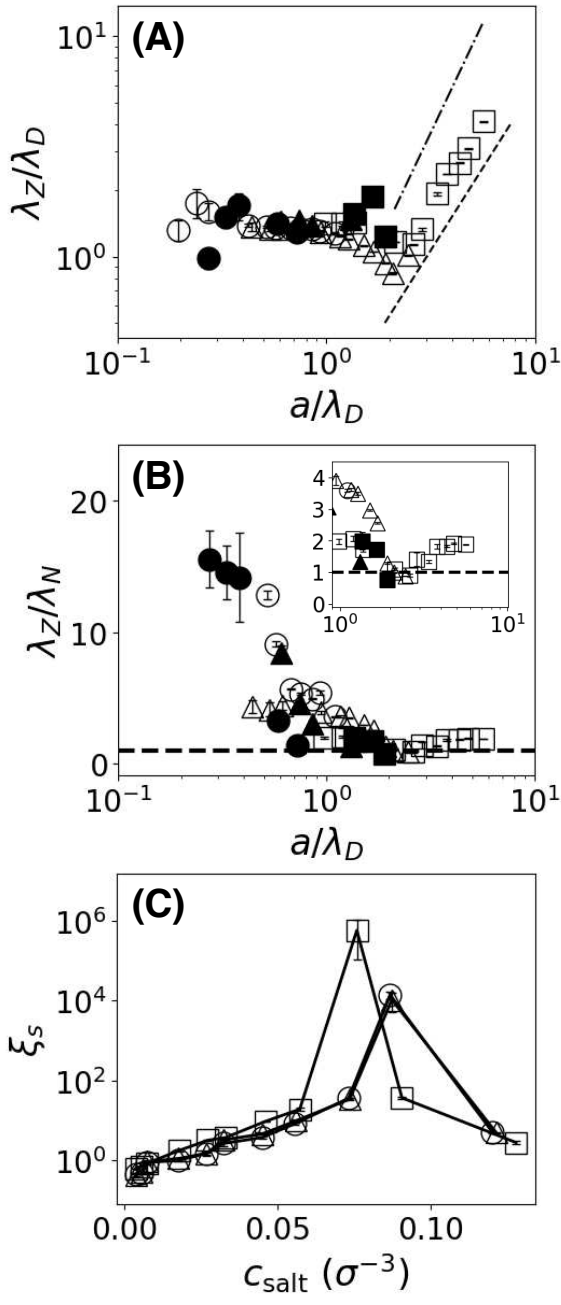


FIG. 5. Crossover in structural correlations of implicit-solvent electrolytes. (A) Decay length λ_Z of $h_{ZZ}(r)$ as a function of a/λ_D , where a is the ion size and λ_D is the Debye screening length (Eq. 8). Black dash-dot ($\alpha = 2$) and dashed ($\alpha = 1.5$) lines serve as visual guides for the scaling behavior described in Eq. 1. (B) Ratio of decay lengths λ_Z/λ_N as a function of a/λ_D . Black dashed horizontal line indicates $\lambda_Z/\lambda_N = 1$. The inset shows a magnified view of the transition region. (C) The growth and percolation of ionic clusters with salt concentration c_{salt} , characterized by the exponential decay length ξ_s extracted from $P(s)$ (Eq. 9). The colors and markers are consistent with those in Fig. 4(D-F). Structural correlation functions and their corresponding fitting results for the implicit-solvent systems are provided in the SM [76].

the presence of explicit solvent. Ion self-diffusion in the implicit-solvent models (bottom row in Fig. 4) slows down with increasing c_{salt} at a markedly faster rate than in the explicit-solvent systems. This slowdown is gradual in both the dilute and concentrated regimes, leading to a smooth increase in τ_{diff} . Ion-pair lifetimes exhibit a similar trend in the dilute systems ($\varepsilon_s = 1$ and 5), where τ_{pair} increases slowly with salt concentration.

Notably, τ_{pair} exhibits a turnover in the concentrated WCA electrolytes ($\varepsilon_s = 0.2$), a behavior not observed in the other systems: it initially decreases—consistent with the explicit-solvent counterparts—but increases again at the highest salt concentrations. This increase cannot be attributed to changes in the ion–counterion local structure $w_{+-}(r)$, as ΔF decreases monotonically over the entire range of c_{salt} . Instead, the turnover may reflect the emergence of a transition to a charge-dominated concentrated regime, rather than to a density-dominated one, or it may be associated with the percolation transition. Further systematic studies are warranted to resolve this intriguing behavior, which is beyond the scope of the present work.

E. Diffusion-corrected ion-pair lifetime combines ion structure and dynamics

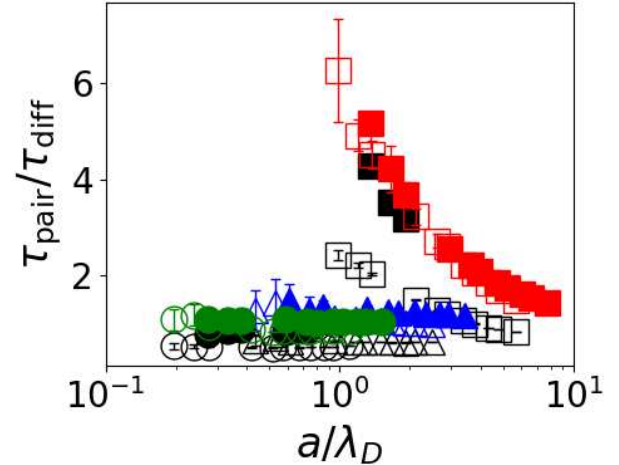


FIG. 6. Diffusion-corrected ion-pair lifetime $\tau_{\text{pair}}/\tau_{\text{diff}}$ as a function of the ratio a/λ_D across all electrolytes examined in this work. For the LJ electrolytes, the colors and markers are consistent with those in Fig. 1, and the black counterparts correspond to the WCA electrolytes.

The distinct c_{salt} -dependence of ion-pair dynamics and ion self-diffusion, as shown in Fig. 4, gives rise to a *bifurcation* in the relaxation times across the crossover. In the charge-dominated dilute regime, both ion diffusion and ion-pair dynamics in explicit-solvent systems depend relatively weakly on c_{salt} . By contrast, in the concentrated regime, either density- or charge-dominated, ion diffusion slows down while the ion-pair lifetime decreases with increasing c_{salt} . This bi-

furcation behavior is consistently observed across all electrolytes systems studied in this work.

To capture this behavior consistently, we propose the diffusion-corrected ion-pair lifetime, $\tau_{\text{pair}}/\tau_{\text{diff}}$, which provides a unified basis for interpreting ion dynamics in relation to the underlying ion structure (Fig. 6). The ratio effectively compensates for viscosity-related effects that primarily arise from differences in non-electrostatic interactions in explicit-solvent systems. Remarkably, the dependence of $\tau_{\text{pair}}/\tau_{\text{diff}}$ on the structural parameter a/λ_D parallels that of the barrier-crossing factor $\exp(\beta\Delta F)$, underscoring the close connection between ion-pair dynamics and the short-range potential of mean force, $\beta w_{+-}(r)$.

Consistent with the behavior of $\exp(\beta\Delta F)$, the ratio $\tau_{\text{pair}}/\tau_{\text{diff}}$ exhibits a clear discontinuity across different ϵ_s : it remains nearly constant in the dilute regime ($\epsilon_s = 1$ and 5), but decreases systematically in the concentrated regime ($\epsilon_s = 0.2$). Notably, $\tau_{\text{pair}}/\tau_{\text{diff}}$ further enables qualitative comparison across models with and without explicit solvents, despite quantitative deviations that are more pronounced in the charge-dominated concentrated regime (black open squares in Fig. 6). The comparatively small decrease observed for the implicit-solvent WCA electrolytes can be attributed to their relatively small free-energy barrier ΔF (Fig. 4(F)). These quantitatively distinct dynamical behavior between charge-dominated and density-dominated concentrated regimes warrants further detailed investigation.

IV. CONCLUSIONS

Using molecular dynamics simulations of model electrolytes with and without explicit solvent, we systematically investigated the relationships between structural and dynamical correlations in dense ionic fluids across a wide range of salt concentrations. We find that the electrostatic screening crossover depends sensitively on ion-solvent coupling. In explicit-solvent electrolytes, the crossover occurs between a charge-dominated dilute regime and a density-dominated concentrated regime, whereas in implicit-solvent electrolytes, it occurs between two charge-dominated regimes—from dilute to concentrated. Both explicit- and implicit-solvent systems display dynamical crossovers in ion self-diffusion and ion-pair lifetimes that are coupled to the screening transition, although the detailed dynamical behaviors differ depending on the presence of solvent. The notable discontinuity across the dynamical transition is well encoded in the ion–counterion short-range structures. Ionic clusters grow with increasing salt concentration and eventually form a percolating network beyond a threshold concentration. However, the percolation transition is not strongly coupled to the onset of either the structural or dynamical crossovers and appears instead to be governed primarily by salt concentration. This decoupling can be rationalized by the distinct physical requirements of the two phenomena: percolation requires sufficiently extensive aggregation to form a system-spanning network and thus

typically occurs only at higher salt concentrations, whereas the onset of underscreening reflects the emergence of local ion pairing or small aggregates. These observations also suggest that spatial proximity alone is insufficient to explain the connection between ionic clustering and transport in these model systems.

For consistent comparison across systems, we demonstrate that the diffusion-corrected ion-pair lifetime, $\tau_{\text{pair}}/\tau_{\text{diff}}$, serves as a unified descriptor that bridges ionic structure and dynamics. The ratio effectively compensates for viscosity-related effects arising from non-electrostatic attractions, while its dependence on the structural parameter a/λ_D mirrors the behavior of the barrier-crossing factor $\exp(\beta\Delta F)$ associated with short-range ion–counterion structure, particularly the discontinuity across the dynamical crossover. Moreover, $\tau_{\text{pair}}/\tau_{\text{diff}}$ enables consistent qualitative comparison between explicit- and implicit-solvent electrolytes, despite quantitative differences that become more pronounced at high salt concentrations, which is worth future systematic investigation.

Our simple models inevitably carry limitations, primarily due to the assumption of a continuum dielectric medium, which can lead to excessive screening of electrostatic interactions at unphysically short distances. Future studies may further explore the coupling and decoupling among electrostatic screening, ionic clustering, and charge transport using chemically more detailed models.

SUPPLEMENTAL MATERIAL

Supplemental Material provides detailed summaries and fitting results of structural, dynamical, and transport properties across all electrolyte conditions examined in this study. These include charge–charge, density–density, solvent–solvent, cation–anion, cation–solvent correlation functions, cluster-size distributions, mean-squared displacements of ions and solvent, ion-pair survival functions, ionic conductivity, and a detailed analysis of ionic associations.

ACKNOWLEDGMENT

This work was supported by the National Supercomputing Center with supercomputing resources including technical support(KSC-2025-CRE-0142). This research was supported by the Regional Innovation System & Education(RISE) program through the Jeju RISE center, funded by the Ministry of Education(MOE) and the Jeju Special Self-Governing Province, Republic of Korea(2025-RISE-17-001).

DATA AVAILABILITY STATEMENT

The data that support the findings of this article are openly available [105].

[1] Y. Yamada, K. Furukawa, K. Sodeyama, K. Kikuchi, M. Yae-gashi, Y. Tateyama, and A. Yamada, Unusual stability of acetonitrile-based superconcentrated electrolytes for fast-charging lithium-ion batteries, *J. Am. Chem. Soc.* **136**, 5039 (2014).

[2] L. Suo, O. Borodin, T. Gao, M. Olgun, J. Ho, X. Fan, C. Luo, C. Wang, and K. Xu, “water-in-salt” electrolyte enables high-voltage aqueous lithium-ion chemistries, *Science* **350**, 938 (2015).

[3] Y. Wang and W.-H. Zhong, Development of electrolytes towards achieving safe and high-performance energy-storage devices: a review, *ChemElectroChem* **2**, 22 (2015).

[4] L. Long, S. Wang, M. Xiao, and Y. Meng, Polymer electrolytes for lithium polymer batteries, *J. Mater. Chem. A* **4**, 10038 (2016).

[5] J. Wang, Y. Yamada, K. Sodeyama, C. H. Chiang, Y. Tateyama, and A. Yamada, Superconcentrated electrolytes for a high-voltage lithium-ion battery, *Nat. Commun.* **7**, 12032 (2016).

[6] L. Xia, L. Yu, D. Hu, and G. Z. Chen, Electrolytes for electrochemical energy storage, *Mater. Chem. Front.* **1**, 584 (2017).

[7] Y. Yamada, J. Wang, S. Ko, E. Watanabe, and A. Yamada, Advances and issues in developing salt-concentrated battery electrolytes, *Nat. Energy* **4**, 269 (2019).

[8] T. Ye, L. Li, and Y. Zhang, Recent progress in solid electrolytes for energy storage devices, *Adv. Funct. Mater.* **30**, 2000077 (2020).

[9] H. Kwon, H. Kim, J. Hwang, W. Oh, Y. Roh, D. Shin, and H.-T. Kim, Borate–pyran lean electrolyte-based li-metal batteries with minimal li corrosion, *Nat. Energy* **9**, 57 (2024).

[10] K. Kim, D. Raymond, R. Candeago, and X. Su, Selective cobalt and nickel electrodeposition for lithium-ion battery recycling through integrated electrolyte and interface control, *Nat. Commun.* **12**, 6554 (2021).

[11] S. Hand and R. D. Cusick, Electrochemical disinfection in water and wastewater treatment: identifying impacts of water quality and operating conditions on performance, *Environ. Sci. Technol.* **55**, 3470 (2021).

[12] M. A. Alkhadra, X. Su, M. E. Suss, H. Tian, E. N. Guyes, A. N. Shocron, K. M. Conforti, J. P. De Souza, N. Kim, M. Tedesco, a. W. I. G. Khoiruddin, Khoiruddin, J. G. Santiago, T. A. Hatton, and M. Z. Bazant, Electrochemical methods for water purification, ion separations, and energy conversion, *Chem. Rev.* **122**, 13547 (2022).

[13] Q. Dang, W. Zhang, J. Liu, L. Wang, D. Wu, D. Wang, Z. Lei, and L. Tang, Bias-free driven ion assisted photoelectrochemical system for sustainable wastewater treatment, *Nat. Commun.* **14**, 8413 (2023).

[14] M. Oliot, S. Galier, H. R. de Balmann, and A. Bergel, Ion transport in microbial fuel cells: key roles, theory and critical review, *Appl. Energy* **183**, 1682 (2016).

[15] J. M. Kefauver, A. B. Ward, and A. Patapoutian, Discoveries in structure and physiology of mechanically activated ion channels, *Nature* **587**, 567 (2020).

[16] H. Chen, O. Simoska, K. Lim, M. Grattieri, M. Yuan, F. Dong, Y. S. Lee, K. Beaver, S. Welawatte, E. M. Gaffney, and S. D. Minteer, Fundamentals, applications, and future directions of bioelectrocatalysis, *Chem. Rev.* **120**, 12903 (2020).

[17] P. Debye and E. Hückel, Zur theorie der elektrolyte. i. gefrierpunktserniedrigung und verwandte erscheinungen. physikalische zeitschrift, *Phys. Z* **24**, 185 (1923).

[18] Kontogeorgis, georgios m. and maribo-mogensen, bjørn and thomsen, kaj, *Fluid Phase Equilibr.* **462**, 130 (2018).

[19] M. A. Gebbie, M. Valtiner, X. Banquy, E. T. Fox, W. A. Henderson, and J. N. Israelachvili, Ionic liquids behave as dilute electrolyte solutions, *Proc. Natl. Acad. Sci. U. S. A.* **110**, 9674 (2013).

[20] R. M. Adar, S. A. Safran, H. Diamant, and D. Andelman, Screening length for finite-size ions in concentrated electrolytes, *Phys. Rev. E* **100**, 042615 (2019).

[21] M. Dinpajooh, N. N. Intan, T. T. Duignan, E. Biasin, J. L. Fulton, S. M. Kathmann, G. K. Schenter, and C. J. Mundy, Beyond the debye–hückel limit: Toward a general theory for concentrated electrolytes, *J. Chem. Phys.* **161** (2024).

[22] M. A. Gebbie, H. A. Dobbs, M. Valtiner, and J. N. Israelachvili, Long-range electrostatic screening in ionic liquids, *Proc. Natl. Acad. Sci. U. S. A.* **112**, 7432 (2015).

[23] M. A. Gebbie, A. M. Smith, H. A. Dobbs, A. A. Lee, G. G. Warr, X. Banquy, M. Valtiner, M. W. Rutland, J. N. Israelachvili, S. Perkin, and R. Atkin, Long range electrostatic forces in ionic liquids, *Chem. Commun.* **53**, 1214 (2017).

[24] A. A. Lee, C. S. Perez-martinez, M. Smith, and S. Perkin, Underscreening in concentrated electrolytes, *Faraday Discuss.* **199**, 239 (2017).

[25] H. Jäger, A. Schlaich, J. Yang, C. Lian, S. Kondrat, and C. Holm, A screening of results on the decay length in concentrated electrolytes, *Faraday Discuss.* **246**, 520 (2023).

[26] Y. Avni, R. M. Adar, and D. Andelman, Charge oscillations in ionic liquids : A microscopic cluster model, *Phys. Rev. E* **101**, 010601 (2020).

[27] Z. A. Goodwin and A. A. Kornyshev, Underscreening, over-screening and double-layer capacitance, *Electrochim. Commun.* **82**, 129 (2017).

[28] A. A. Lee, C. S. Perez-Martinez, A. M. Smith, and S. Perkin, Scaling analysis of the screening length in concentrated electrolytes, *Phys. Rev. Lett.* **119**, 026002 (2017).

[29] E. Krucker-Velasquez and J. W. Swan, Underscreening and hidden ion structures in large scale simulations of concentrated electrolytes, *J. Chem. Phys.* **155**, 134903 (2021).

[30] B. Rotenberg, O. Bernard, and J.-P. Hansen, Underscreening in ionic liquids: a first principles analysis, *J. Phys. Condens. Matter* **30**, 054005 (2018).

[31] X. Zhang, Z. A. Goodwin, A. G. Hoane, A. Deptula, D. M. Markiewitz, N. Molinari, Q. Zheng, H. Li, M. McEldrew, B. Kozinsky, *et al.*, Long-range surface forces in salt-in-ionic liquids, *ACS Nano* **18**, 34007 (2024).

[32] J. G. Kirkwood, Statistical mechanics of liquid solutions, *Chem. Rev.* **19**, 275 (1936).

[33] S. W. Coles, C. Park, R. Nikam, M. Kanduc, J. Dzubiella, and B. Rotenberg, Correlation length in concentrated electrolytes: Insights from all-atom molecular dynamics simulations, *J. Phys. Chem. B* **124**, 1778 (2020).

[34] J. Zeman, S. Kondrat, and C. Holm, Ionic screening in bulk and under confinement, *J. Chem. Phys.* **155**, 204501 (2021).

[35] R. M. Adar, S. A. Safran, H. Diamant, and D. Andelman, Screening length for finite-size ions in concentrated electrolytes, *Phys. Rev. E* **100**, 42615 (2019).

[36] P. Cats, R. Evans, A. Härtel, and R. V. Roij, Primitive model electrolytes in the near and far field : Decay lengths from DFT and simulations, *J. Chem. Phys.* **154**, 124504 (2021).

[37] E. Waisman and J. L. Lebowitz, Mean spherical model integral equation for charged hard spheres i. method of solution,

J. Chem. Phys. **56**, 3086 (1972).

[38] J.-P. Simonin and J. S. Høye, Full solution to the mean spherical approximation (msa) for an arbitrary mixture of ions in a dipolar solvent, J. Chem. Phys. **155** (2021).

[39] V. Démery and D. S. Dean, The conductivity of strong electrolytes from stochastic density functional theory, J. Stat. Mech. **2016**, 023106 (2016).

[40] Y. Avni, D. Andelman, and H. Orland, Conductance of concentrated electrolytes: Multivalency and the wien effect, J. Chem. Phys. **157** (2022).

[41] P. Illien, A. Carof, and B. Rotenberg, Stochastic density functional theory for ions in a polar solvent, Phys. Rev. Lett. **133**, 268002 (2024).

[42] L. Onsager, Report on a revision of the conductivity theory, Trans. Faraday Soc. **23**, 341 (1927).

[43] M. Cetin, Electrolytic conductivity, debye-hückel theory, and the onsager limiting law, Phys. Rev. E **55**, 2814 (1997).

[44] Y. Avni, R. M. Adar, D. Andelman, and H. Orland, Conductivity of concentrated electrolytes, Phys. Rev. Lett. **128**, 098002 (2022).

[45] P. Robin, Correlation-induced viscous dissipation in concentrated electrolytes, The Journal of Chemical Physics **160** (2024).

[46] O. Bernard, M. Jardat, B. Rotenberg, and P. Illien, On analytical theories for conductivity and self-diffusion in concentrated electrolytes, The Journal of Chemical Physics **159** (2023).

[47] G. Feng, M. Chen, S. Bi, Z. A. Goodwin, E. B. Postnikov, N. Brilliantov, M. Urbakh, and A. A. Kornyshev, Free and bound states of ions in ionic liquids, conductivity, and underscreening paradox, Phys. Rev. X **9**, 021024 (2019).

[48] N. Molinari, J. P. Mailoa, and B. Kozinsky, General trend of a negative li effective charge in ionic liquid electrolytes, J. Phys. Chem. Lett. **10**, 2313 (2019).

[49] A. France-Lanord and J. C. Grossman, Correlations from ion pairing and the nernst-einstein equation, Phys. Rev. Lett. **122**, 136001 (2019).

[50] S. Bi and M. Salanne, Cluster analysis as a tool for quantifying structure-transport properties in simulations of superconcentrated electrolyte, Chem. Sci. **15**, 10908 (2024).

[51] Y. Shen, B. Liu, X. Liu, J. Liu, J. Ding, C. Zhong, and W. Hu, Water-in-salt electrolyte for safe and high-energy aqueous battery, Energy Storage Mater. **34**, 461 (2021).

[52] E. Krucker-Velasquez and J. W. Swan, Underscreening and hidden ion structures in large scale simulations of concentrated electrolytes, J. Chem. Phys. **155** (2021).

[53] S. Wang, H. Tao, J. Yang, J. Cheng, H. Liu, and C. Lian, Structure and screening in confined electrolytes: The role of ion association, J. Phys. Chem. Lett. **15**, 7147 (2024).

[54] X. Liu and X. Kong, Minimal coarse-grained models of polar solvent for electrolytes: Stockmayer versus dumbbell, J. Phys. Chem. B **128**, 3953 (2024).

[55] D. M. Markiewitz, Z. A. H. Goodwin, Q. Zheng, M. McEldrew, R. M. Espinosa-Marzal, and M. Z. Bazant, Ionic associations and hydration in the electrical double layer of water-in-salt electrolytes, ACS Appl. Mater. Interfaces. **17**, 29515 (2025).

[56] G. Feng and P. T. Cummings, Supercapacitor capacitance exhibits oscillatory behavior as a function of nanopore size, J. Phys. Chem. Lett. **2**, 2859 (2011).

[57] Y. Lee, J. Cho, J. Kim, W. B. Lee, and Y. Jho, Anomalous diffusion of lithium-anion clusters in ionic liquids, The European Physical Journal E **46**, 105 (2023).

[58] O. Borodin and G. D. Smith, Litfci structure and transport in ethylene carbonate from molecular dynamics simulations, J. Phys. Chem. B **110**, 4971 (2006).

[59] O. Borodin, L. Suo, M. Gobet, X. Ren, F. Wang, A. Faraone, J. Peng, M. Olgun, M. Schroeder, M. S. Ding, *et al.*, Liquid structure with nano-heterogeneity promotes cationic transport in concentrated electrolytes, ACS nano **11**, 10462 (2017).

[60] M. McEldrew, Z. A. Goodwin, S. Bi, M. Z. Bazant, and A. A. Kornyshev, Theory of ion aggregation and gelation in super-concentrated electrolytes, J. Chem. Phys. **152**, 234506 (2020).

[61] M. Rubinstein and R. H. Colby, *Polymer physics* (Oxford university press, 2003).

[62] M. McEldrew, Z. A. Goodwin, S. Bi, A. A. Kornyshev, and M. Z. Bazant, Ion clusters and networks in water-in-salt electrolytes, J. Electrochem. Soc. **168**, 050514 (2021).

[63] M. McEldrew, Z. A. Goodwin, N. Molinari, B. Kozinsky, A. A. Kornyshev, and M. Z. Bazant, Salt-in-ionic-liquid electrolytes: Ion network formation and negative effective charges of alkali metal cations, J. Phys. Chem. B **125**, 13752 (2021).

[64] Z. A. H. Goodwin, M. McEldrew, J. Pedro de Souza, M. Z. Bazant, and A. A. Kornyshev, Gelation, clustering, and crowding in the electrical double layer of ionic liquids, J. Chem. Phys. **157** (2022).

[65] S. A. Safran and P. A. Pincus, Scaling perspectives of underscreening in concentrated electrolyte solutions, Soft Matter **19**, 7907 (2023).

[66] I. Skarmoutsos and S. Mossa, Length scales in electrolytes, The Journal of Chemical Physics **163** (2025).

[67] B. Giera, N. Henson, E. M. Kober, M. S. Shell, and T. M. Squires, Electric double-layer structure in primitive model electrolytes: comparing molecular dynamics with local-density approximations, Langmuir **31**, 3553 (2015).

[68] A. Härtel, M. Bültmann, and F. Coupette, Anomalous underscreening in the restricted primitive model, Phys. Rev. Lett. **130**, 108202 (2023).

[69] J. Yang, S. Kondrat, C. Lian, H. Liu, A. Schlaich, and C. Holm, Solvent effects on structure and screening in confined electrolytes, Phys. Rev. Lett. **131**, 118201 (2023).

[70] D. Ribar, C. E. Woodward, S. Nordholm, and J. Forsman, Cluster formation induced by local dielectric saturation in restricted primitive model electrolytes, The Journal of Physical Chemistry Letters **15**, 8326 (2024).

[71] L. Joly, C. Ybert, E. Trizac, and L. Bocquet, Liquid friction on charged surfaces: From hydrodynamic slippage to electrokinetics, The Journal of Chemical Physics **125**, 204716 (2006).

[72] L. Scalfi, B. Coasne, and B. Rotenberg, On the gibbs-thomson equation for the crystallization of confined fluids, J. Chem. Phys. **154** (2021).

[73] J. Kim and B. Rotenberg, Donnan equilibrium in charged slit-pores from a hybrid nonequilibrium molecular dynamics/monte carlo method with ions and solvent exchange, The Journal of Chemical Physics **161**, 054107 (2024).

[74] A. Brünger, C. L. Brooks III, and M. Karplus, Stochastic boundary conditions for molecular dynamics simulations of st2 water, Chem. Phys. Lett. **105**, 495 (1984).

[75] B. Dünweg and W. Paul, Brownian dynamics simulations without gaussian random numbers, Int. J. Mod. Phys. C **2**, 817 (1991).

[76] See Supplemental Material at [URL will be inserted by publisher] for summaries of simulation results, additional figures, structural and dynamical correlation-function analyses, fitting procedures, and a detailed analysis of ionic associations, which includes Ref. [104] [Ref. S8 in Supplemental Material].

[77] R. Kjellander and D. J. Mitchell, Dressed-ion theory for electrolyte solutions: A debye-hückel-like reformulation of the

exact theory for the primitive model, *J. Chem. Phys.* **101**, 603 (1994).

[78] R. J. F. Leote de Carvalho and R. Evans, The decay of correlations in ionic fluids, *Mol. Phys.* **83**, 619 (1994).

[79] J. Ennis, R. Kjellander, and D. J. Mitchell, Dressed ion theory for bulk symmetric electrolytes in the restricted primitive model, *J. Chem. Phys.* **102**, 975 (1995).

[80] J. Ulander and R. Kjellander, The decay of pair correlation functions in ionic fluids: a dressed ion theory analysis of monte carlo simulations, *J. Chem. Phys.* **114**, 4893 (2001).

[81] B. Forsberg, J. Ulander, and R. Kjellander, Dressed ion theory of size-asymmetric electrolytes: Effective ionic charges and the decay length of screened coulomb potential and pair correlations, *J. Chem. Phys.* **122** (2005).

[82] A. A. Hagberg, D. A. Schult, and P. J. Swart, Exploring network structure, dynamics, and function using NetworkX, in *Proceedings of the 7th Python in Science Conference (SciPy2008)*, edited by G. Varoquaux, T. Vaught, and J. Millman (SciPy, 2008) pp. 11–15.

[83] P.-G. De Gennes, *Scaling concepts in polymer physics* (Cornell university press, 1979).

[84] D. Stauffer and A. Aharony, *Introduction to percolation theory* (Taylor & Francis, 2018).

[85] M. McEldrew, Z. A. Goodwin, H. Zhao, M. Z. Bazant, and A. A. Kornyshev, Correlated ion transport and the gel phase in room temperature ionic liquids, *J. Phys. Chem. B* **125**, 2677 (2021).

[86] Z. A. Goodwin, M. McEldrew, B. Kozinsky, and M. Z. Bazant, Theory of cation solvation and ionic association in nonaqueous solvent mixtures, *Phys. Rev. X Energy* **2**, 013007 (2023).

[87] N. Michaud-Agrawal, E. J. Denning, T. B. Woolf, and O. Beckstein, Mdanalysis: a toolkit for the analysis of molecular dynamics simulations, *J. Comput. Chem.* **32**, 2319 (2011).

[88] R. J. Gowers, M. Linke, J. Barnoud, T. J. E. Reddy, M. N. Melo, S. L. Seyler, D. L. Dotson, J. Domanski, S. Buchoux, I. M. Kenney, and O. Beckstein, Mdanalysis: A python package for the rapid analysis of molecular dynamics simulations, in *Proceedings of the 15th Python in Science Conference (SciPy 2016)* (2016) pp. 98–105.

[89] K. D. Fong, J. Self, B. D. McCloskey, and K. A. Persson, Ion correlations and their impact on transport in polymer-based electrolytes, *Macromolecules* **54**, 2575 (2021).

[90] K. D. Fong, J. Self, B. D. McCloskey, and K. A. Persson, Onsager transport coefficients and transference numbers in polyelectrolyte solutions and polymerized ionic liquids, *Macromolecules* **53**, 9503 (2020).

[91] T. Hoang Ngoc Minh, J. Kim, G. Pireddu, I. Chubak, S. Nair, and B. Rotenberg, Electrical noise in electrolytes: a theoretical perspective, *Faraday Discuss.* **246**, 198 (2023).

[92] H. Park, B. J. Sung, and J. Kim, Bridging electrostatic screening and ion transport in lithium salt-doped ionic liquids, *J. Chem. Phys.* **163** (2025).

[93] A. M. Smith, A. A. Lee, and S. Perkin, The electrostatic screening length in concentrated electrolytes increases with concentration, *J. Phys. Chem. Lett.* **7**, 2157 (2016).

[94] J. M. Dean, S. W. Coles, W. R. Saunders, A. R. McCluskey, M. J. Wolf, A. B. Walker, and B. J. Morgan, Overscreening and underscreening in solid-electrolyte grain boundary space-charge layers, *Phys. Rev. Lett.* **127**, 135502 (2021).

[95] S. S. Lee, A. Koishi, I. C. Bourg, and P. Fenter, Ion correlations drive charge overscreening and heterogeneous nucleation at solid-aqueous electrolyte interfaces, *Proc. Natl. Acad. Sci. U. S. A.* **118**, e2105154118 (2021).

[96] S. Kumar, P. Cats, M. B. Alotaibi, S. C. Ayirala, A. A. Yousef, R. V. Roij, I. Siretanu, and F. Mugele, Absence of anomalous underscreening in highly concentrated aqueous electrolytes confined between smooth silica surfaces saravana, *J. Colloid Interface Sci.* **622**, 819 (2022).

[97] F. Coupette, A. A. Lee, and A. Härtel, Screening lengths in ionic fluids, *Phys. Rev. Lett.* **121**, 075501 (2018).

[98] L. Kazmierczak, I. Janik, M. Wolszczak, and D. Swiatla-Wojciek, Dynamics of ion pairing in dilute aqueous hcl solutions by spectroscopic measurements of hydroxyl radical conversion into dichloride radical anions, *J. Phys. Chem. B* **125**, 9564 (2021).

[99] E. Guardia, R. Rey, and J. A. Padró, Potential of mean force by constrained molecular dynamics: a sodium chloride ion-pair in water, *Chem. Phys.* **155**, 187 (1991).

[100] E. Guardia, R. Rey, and J. Padró, Na+–na+ and cl–cl- ion pairs in water: mean force potentials by constrained molecular dynamics, *J. Chem. Phys.* **95**, 2823 (1991).

[101] L. R. Pratt, G. Hummer, and A. E. Garcia, Ion pair potentials-of-mean-force in water, *Biophys. Chem.* **51**, 147 (1994).

[102] P. L. Geissler, C. Dellago, and D. Chandler, Kinetic pathways of ion pair dissociation in water, *J. Phys. Chem. B* **103**, 3706 (1999).

[103] N. N. Kalikin and Y. A. Budkov, Modified debye–hückel–onsager theory for electrical conductivity in aqueous electrolyte solutions: Account of ionic charge nonlocality, *J. Chem. Phys.* **161** (2024).

[104] J.-H. Choi, H. R. Choi, J. Jeon, and M. Cho, Ion aggregation in high salt solutions. VII. The effect of cations on the structures of ion aggregates and water hydrogen-bonding network, *J. Chem. Phys.* **147**, 154107 (2017).

[105] All simulation data and all figure-plotting scripts are available at the GitHub repository (<https://github.com/daehyeok48/Structural-and-Dynamical-Crossovers-in-Dense-Electrolytes>).

Supplemental Material for
Structural and Dynamical Crossovers in Dense Electrolytes

Daehyeok Kim,¹ Taejin Kwon^{†,2} and Jeongmin Kim^{*3}

¹*Department of Energy Engineering, Korea Institute of Energy
Technology (KENTECH), Naju 58330, Republic of Korea*

²*Department of Chemistry and Cosmetics,
Jeju National University, Jeju 63243, Republic of Korea*

³*Department of Chemistry Education and Graduate Department of Chemical Materials,
Pusan National University, Busan 46241, Republic of Korea*

(^{**}jeongmin@pusan.ac.kr)

(^{*†}tjkwon@jejunu.ac.kr)

CONTENTS

S1. Salt concentration as a function of salt-to-solvent ratio	3
S2. Decay length and oscillation period of structural correlation functions	4
S3. Fitting results of structural correlation functions for explicit-solvent electrolytes	5
S4. Fitting results of structural correlation functions for implicit-solvent electrolytes	11
S5. Evolution of ionic clusters and their fitting results	15
S6. Potential of mean force between cations and anions	17
S7. Fitting results of mean-squared displacement for ions and solvent	19
A. Explicit-solvent electrolytes	19
B. Implicit-solvent electrolytes	23
S8. Fitting results of ion-pair survival function	26
S9. Ionic conductivity	29
S10. Ionic cluster analysis: comparison between Cayley-tree-based theory and simulation	34
A. Ion association patterns	34
B. Comparison of ionic association between theory and simulations	36
References	41

S1. SALT CONCENTRATION AS A FUNCTION OF SALT-TO-SOLVENT RATIO

Table S1 lists the salt concentration c_{salt} as a function of the salt-to-solvent ratio r_{salt} for all explicit-solvent electrolytes examined.

r_{salt}	$c_{\text{salt}} (\epsilon_s = 0.2)$	$c_{\text{salt}} (\epsilon_s = 1)$	$c_{\text{salt}} (\epsilon_s = 5)$
0.01	0.007± 0.001	0.007± 0.001	0.007± 0.001
0.015	0.011± 0.001	0.011± 0.001	0.011± 0.001
0.02	0.014± 0.001	0.014± 0.001	0.014± 0.001
0.05	0.034± 0.001	0.034± 0.001	0.034± 0.001
0.08	0.052± 0.001	0.052± 0.001	0.052± 0.001
0.1	0.063± 0.001	0.063± 0.001	0.063± 0.001
0.15	0.088± 0.001	0.087± 0.001	0.087± 0.001
0.2	0.109± 0.001	0.108± 0.001	0.107± 0.001
0.3	0.144± 0.001	0.141± 0.001	0.141± 0.001
0.4	0.171± 0.001	0.168± 0.001	0.167± 0.001
0.8	0.239± 0.001	0.233± 0.001	0.231± 0.001
<hr/>			
0.01	0.004± 0.001	0.004± 0.001	0.004± 0.001
0.015	0.006± 0.001	0.006± 0.001	0.006± 0.001
0.02	0.008± 0.001	0.007± 0.001	0.007± 0.001
0.05	0.018± 0.001	0.018± 0.001	0.018± 0.001
0.08	0.027± 0.001	0.027± 0.001	0.027± 0.001
0.1	0.033± 0.001	0.033± 0.001	0.032± 0.001
0.15	0.046± 0.001	0.045± 0.001	0.045± 0.001
0.2	0.057± 0.001	0.056± 0.001	0.056± 0.001
0.3	0.076± 0.001	0.074± 0.001	0.073± 0.001
0.4	0.091± 0.001	0.087± 0.001	0.087± 0.001
0.8	0.128± 0.001	0.121± 0.001	0.120± 0.001

TABLE S1. Variation of salt concentration c_{salt} as a function of the salt-to-solvent ratio r_{salt} for various ϵ_s values: LJ (top) and WCA (bottom) electrolytes.

S2. DECAY LENGTH AND OSCILLATION PERIOD OF STRUCTURAL CORRELATION FUNCTIONS

Figure S1 displays the decay lengths and oscillation periods across all electrolytes examined. The charge–charge correlation function $h_{ZZ}(r)$ exhibits a simple Yukawa decay in the dilute regime, with the decay length decreasing as $\lambda_Z \sim 1/\sqrt{c_{\text{salt}}}$. At higher concentrations, however, an oscillatory contribution emerges, characterized by the oscillation period l_Z . In contrast, the density–density correlation function $h_{NN}(r)$ exhibits an oscillatory exponential decay in both dilute and concentrated regimes. The decay length λ_N and oscillation period l_N remain nearly constant over the range of c_{salt} examined.

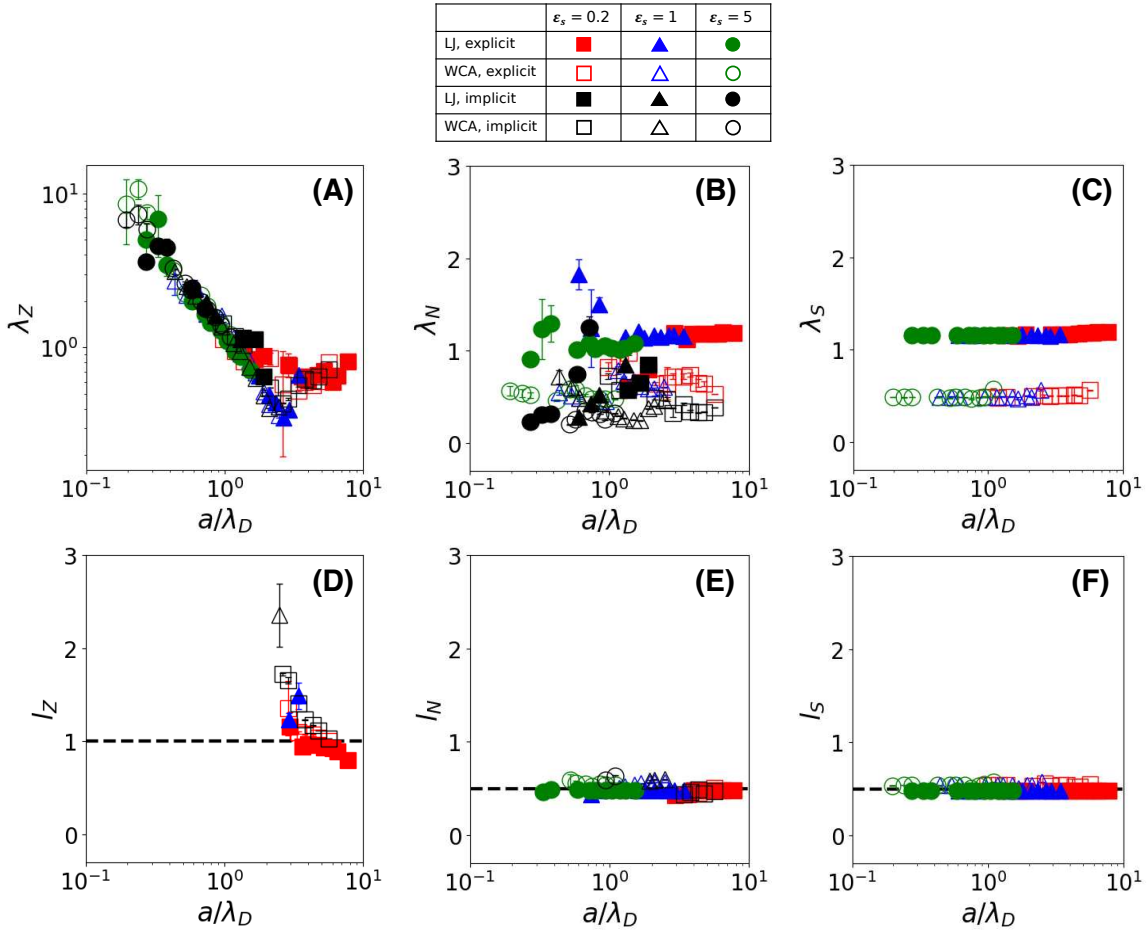


FIG. S1. Decay lengths and oscillation periods across all electrolytes examined. (A) Decay length λ_Z and (D) oscillation period l_Z of $h_{ZZ}(r)$. (B) Decay length λ_N and (E) oscillation period l_N of $h_{NN}(r)$. (C) Decay length λ_S and (F) oscillation period l_S of $h_{SS}(r)$. Black dashed lines serve as guides to the eye.

S3. FITTING RESULTS OF STRUCTURAL CORRELATION FUNCTIONS FOR EXPLICIT-SOLVENT ELECTROLYTES

This section presents the simulation results of structural correlation functions for explicit-solvent LJ and WCA electrolytes, together with the fitting results obtained using a single Yukawa function (Eq. 7 in the main text). The results include:

- the solvent–solvent structural correlation functions, $r|h_{SS}(r)|$ (Fig. S3),
- the charge–charge correlation functions, $r|h_{ZZ}(r)|$ (Fig. S3),
- the density–density correlation functions, $r|h_{NN}(r)|$ (Fig. S4),
- the cation–anion correlation functions, $r|h_{+-}(r)|$ (Fig. S5), and
- the cation–solvent correlation functions, $r|h_{S+}(r)|$ (Fig. S6).

These results collectively illustrate the systematic evolution of structural correlations with ϵ_s and concentration, demonstrating the transition from monotonic to oscillatory decay across electrolyte systems, from charge-dominated dilute to density-dominated concentrated regimes.

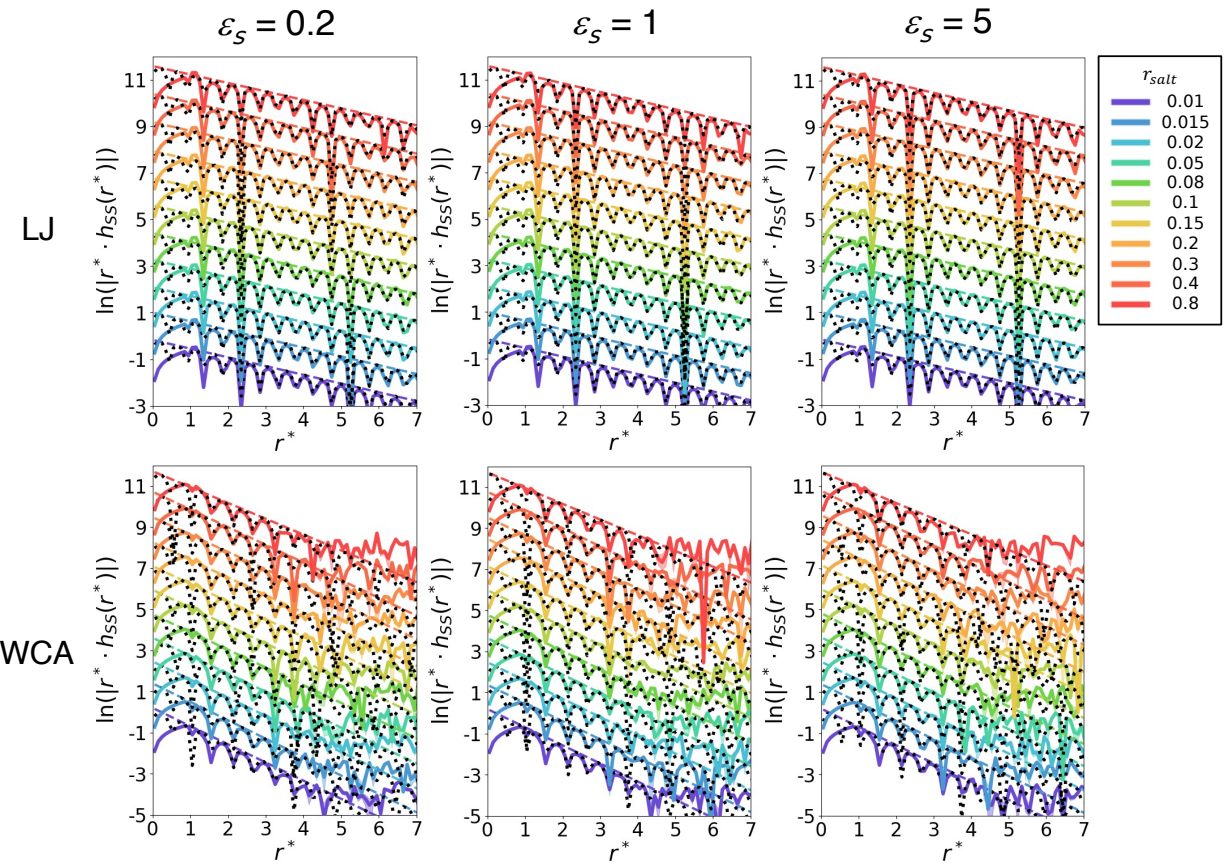


FIG. S2. Solvent–solvent structural correlation functions, $|\mathbf{r} \cdot \mathbf{h}_{SS}(\mathbf{r})|$, of explicit-solvent LJ and WCA electrolytes at various ϵ_s .

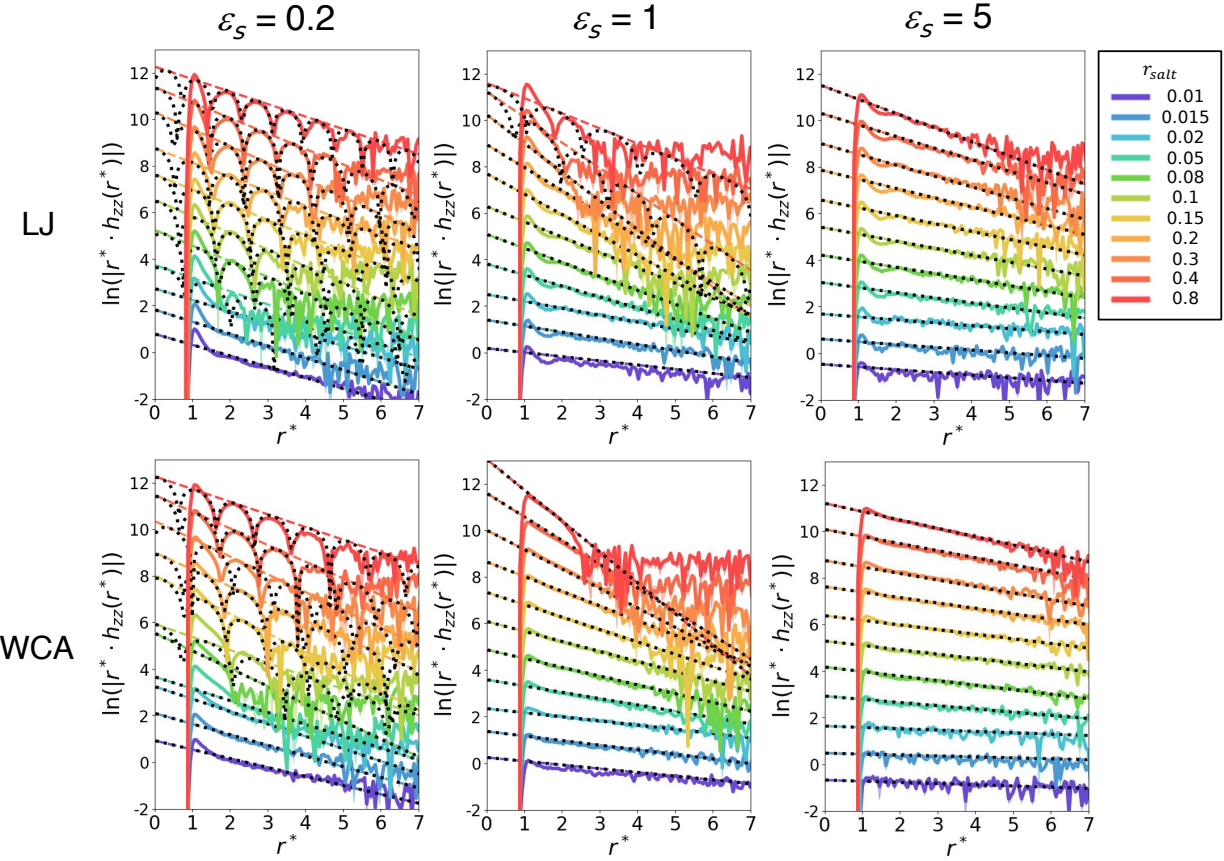


FIG. S3. Charge-charge correlation functions, $|r \cdot h_{ZZ}(r)|$, of explicit-solvent LJ and WCA electrolytes at various ϵ_s .

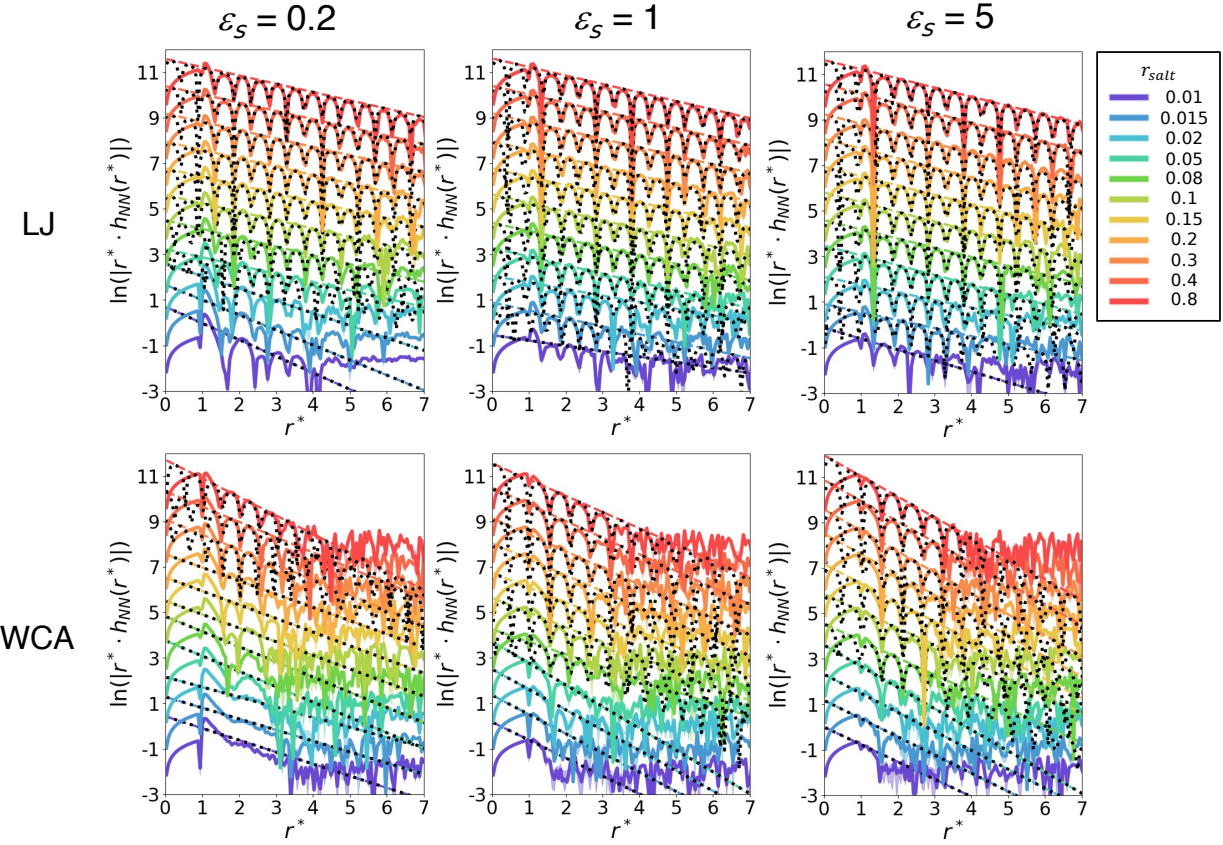


FIG. S4. Density-density correlation functions, $|r \cdot h_{NN}(r)|$, of explicit-solvent LJ and WCA electrolytes at various ε_s .

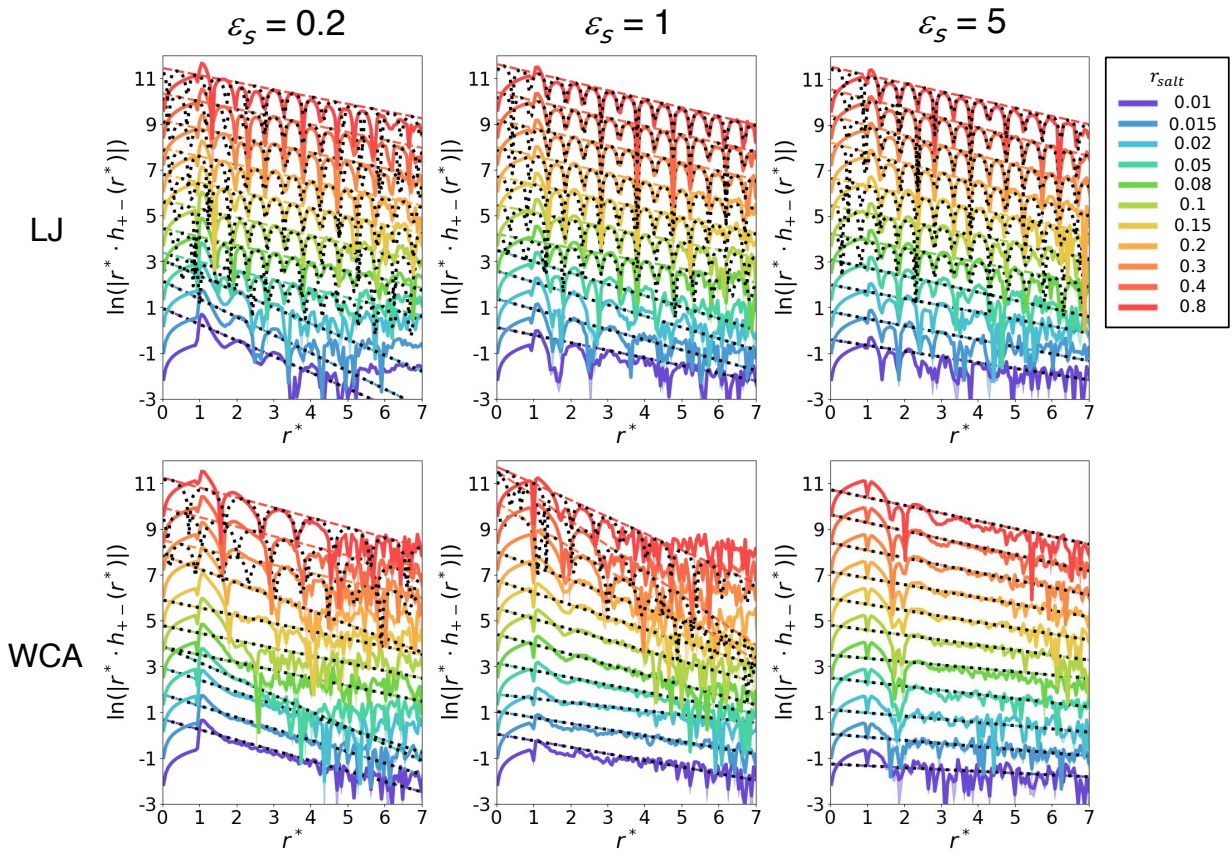


FIG. S5. Cation-anion correlation functions, $|r \cdot h_{+-}(r)|$, of explicit-solvent LJ and WCA electrolytes at various ε_s .

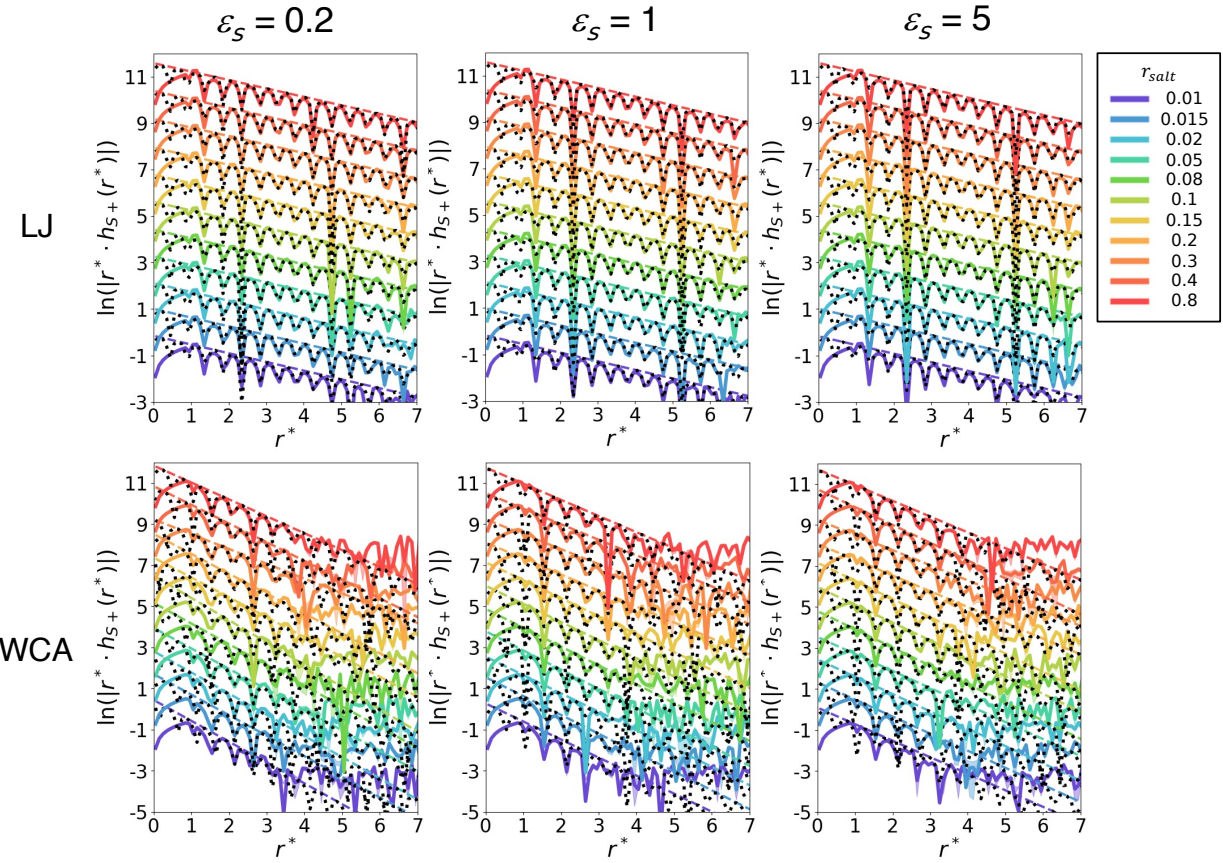


FIG. S6. Cation-solvent correlation functions, $|r \cdot h_{S+}(r)|$, of explicit-solvent LJ and WCA electrolytes at various ϵ_s .

S4. FITTING RESULTS OF STRUCTURAL CORRELATION FUNCTIONS FOR IMPLICIT-SOLVENT ELECTROLYTES

This section, similar to Sec. S3, presents the simulation results of structural correlation functions for implicit-solvent LJ and WCA electrolytes, together with the fitting results obtained using a single Yukawa function (Eq. 7 in the main text). The results include:

- the charge–charge correlation functions, $r|h_{ZZ}(r)|$ (Fig. S8),
- the density–density correlation functions, $r|h_{NN}(r)|$ (Fig. S9), and
- the cation–anion correlation functions, $r|h_{+-}(r)|$ (Fig. S10).

As discussed in the main text and shown in Fig. S7, some implicit-solvent electrolytes exhibits phase segregation.

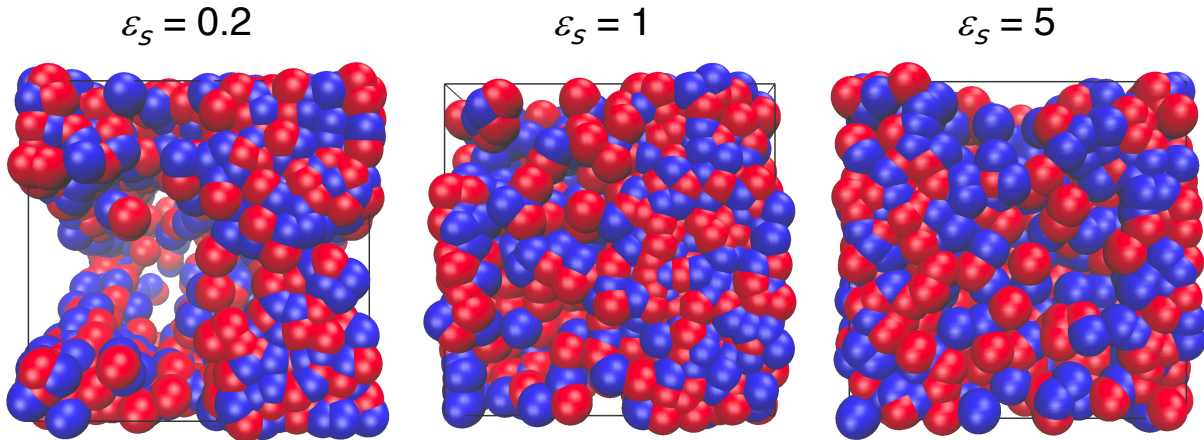


FIG. S7. Simulation snapshots representing phase segregation for implicit-solvent LJ electrolytes at $c_{\text{salt}} = 0.171 \sigma^{-3}$ with diverse ε_s .

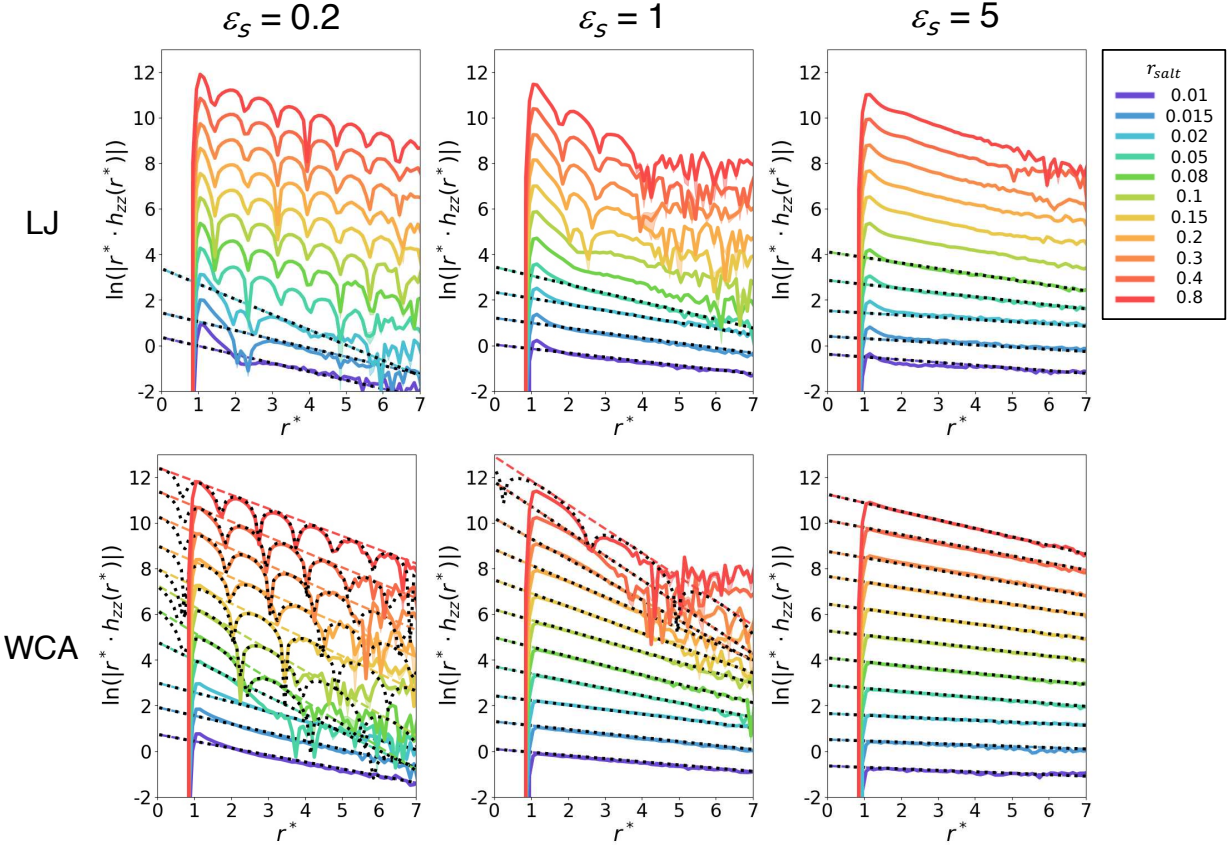


FIG. S8. Charge-charge correlation functions, $|r \cdot h_{zz}(r)|$, of implicit-solvent LJ and WCA electrolytes at various ε_s . The fit curves are not shown for the cases that exhibit phase segregation.

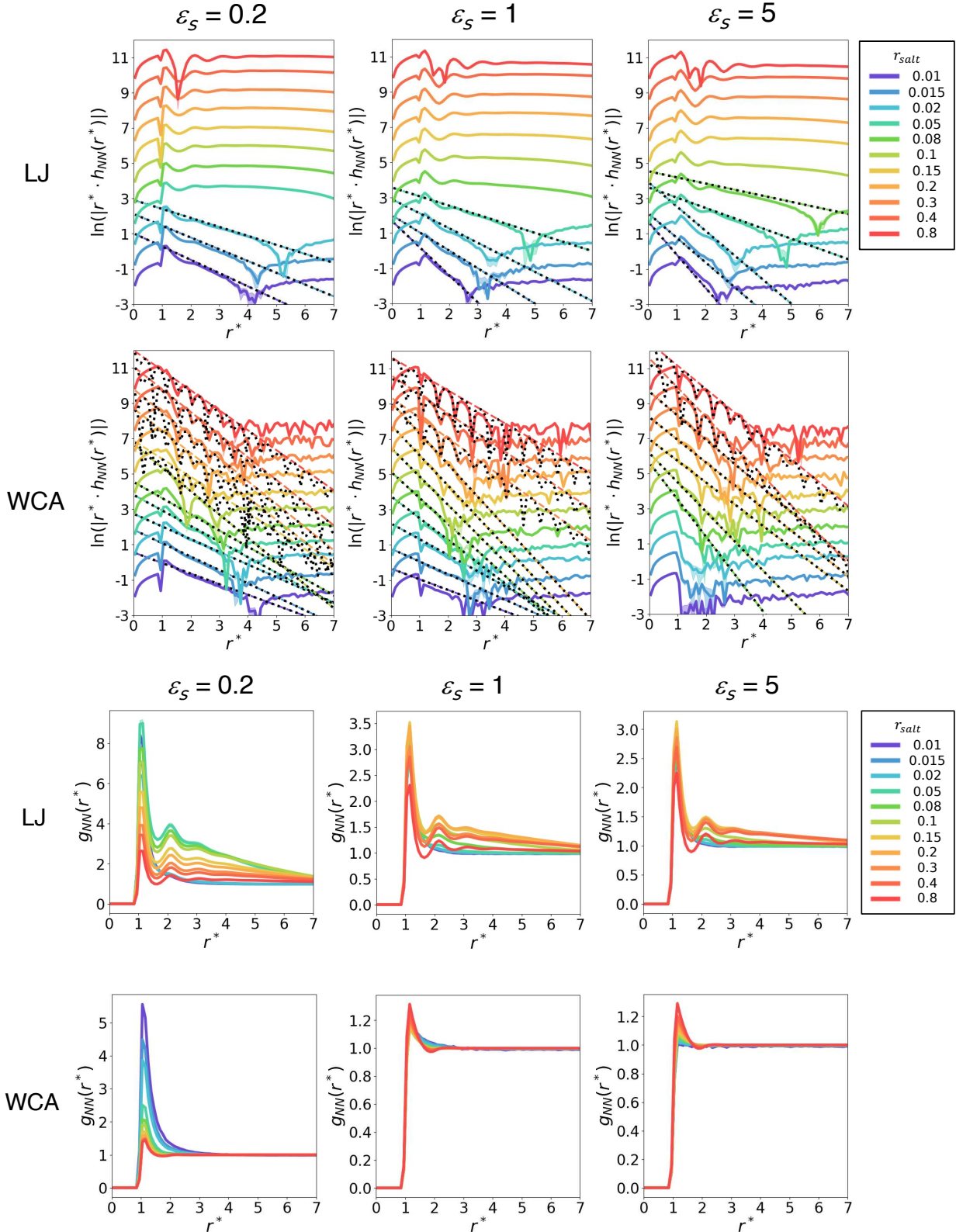


FIG. S9. Density-density correlation functions, $|r \cdot h_{NN}(r)|$, and $g_{NN}(r)$, of implicit-solvent LJ and WCA electrolytes at various ε_s . The fit curves are not shown for the cases that exhibit phase segregation.

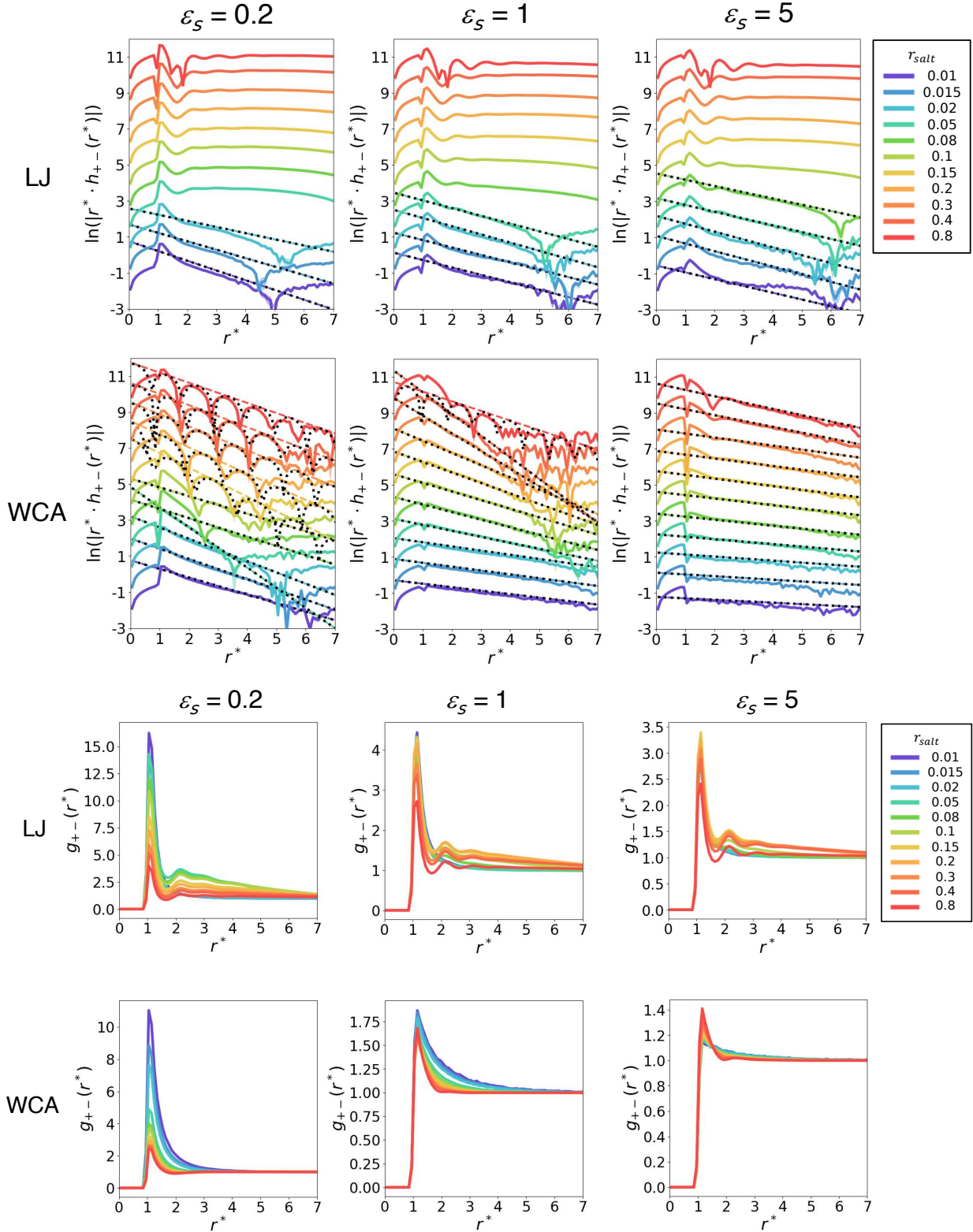


FIG. S10. Cation-anion correlation functions, $|r \cdot h_{+-}(r)|$, and $g_{+-}(r)$, of implicit-solvent LJ and WCA electrolytes at various ε_s . The fit curves are not shown for the cases that exhibit phase segregation.

S5. EVOLUTION OF IONIC CLUSTERS AND THEIR FITTING RESULTS

This section presents the results showing the evolution of ionic clusters across various electrolytes over a wide range of salt concentrations.

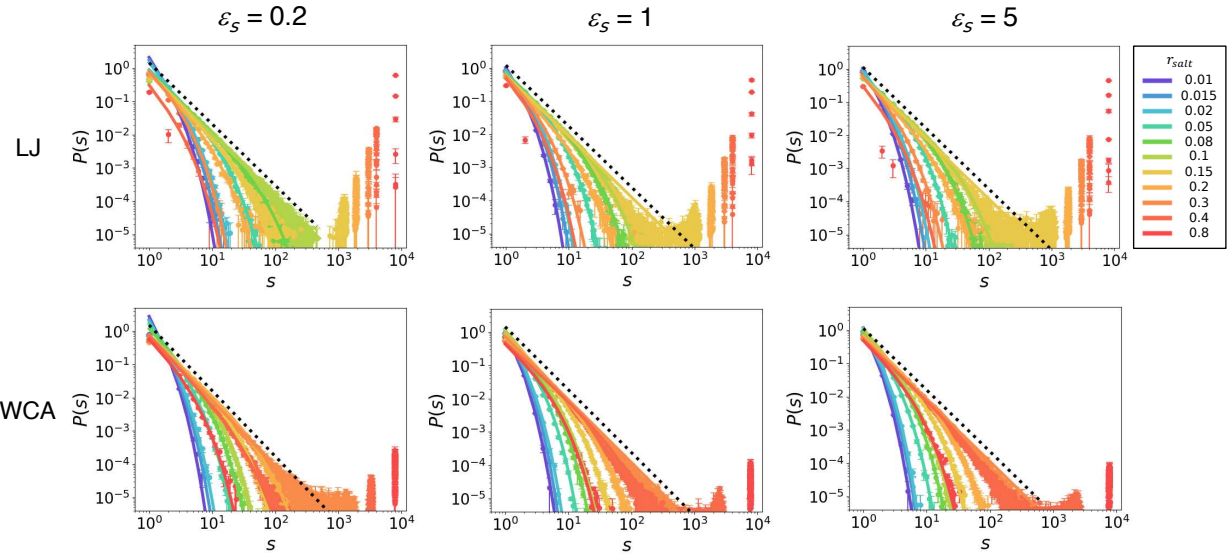


FIG. S11. Size distribution $P(s)$ (Eq. 9 in the main text) of ionic clusters for explicit-solvent LJ and WCA electrolytes at various ϵ_s .

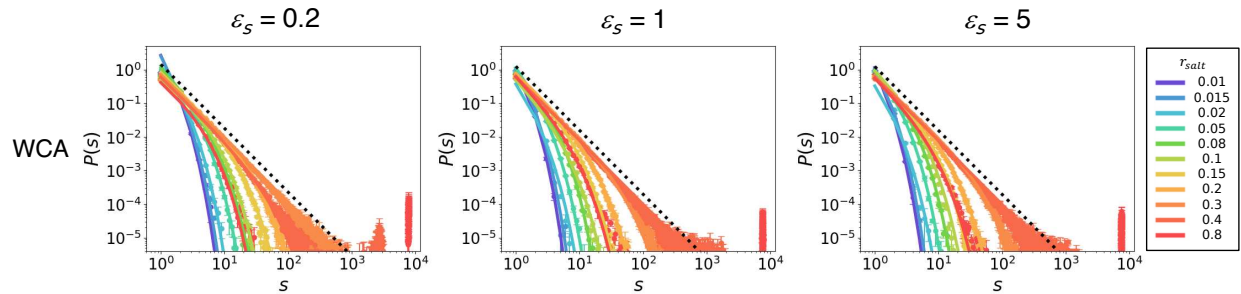


FIG. S12. Size distribution $P(s)$ (Eq. 9 in the main text) of ionic clusters for implicit-solvent WCA electrolytes at various ϵ_s .

	$\varepsilon_s = 0.2$	$\varepsilon_s = 1$	$\varepsilon_s = 5$
LJ, explicit	■	▲	●
WCA, explicit	□	△	○
WCA, implicit	□	△	○

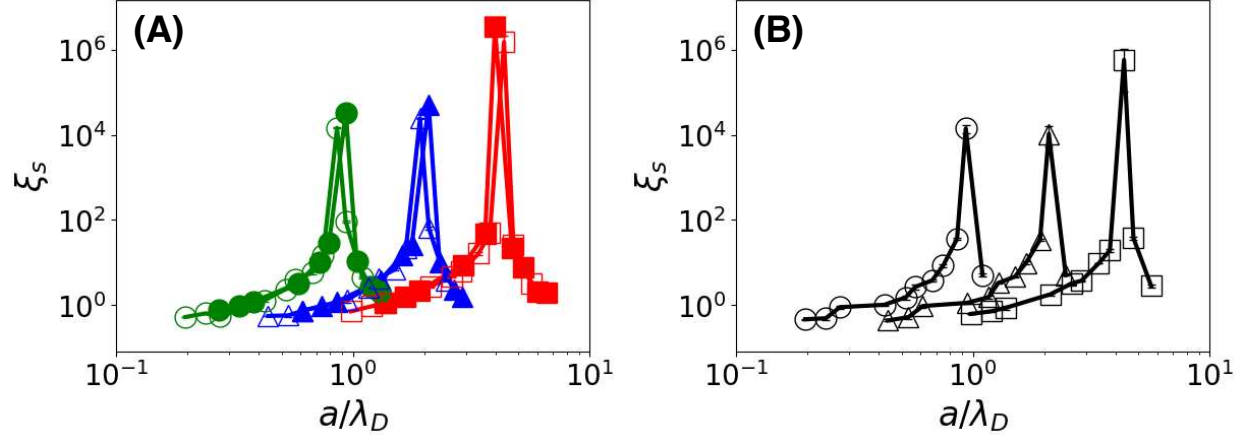


FIG. S13. Exponential decay length ξ_s , extracted from $P(s)$, as a function of a/λ_D . Each panels (A) and (B) show results for explicit-solvent LJ, WCA electrolytes, and implicit-solvent WCA electrolytes.

S6. POTENTIAL OF MEAN FORCE BETWEEN CATIONS AND ANIONS

This section presents the potential of mean force (PMF) between cations and anions, defined as $\beta w_{+-}(r) = -\ln[g_{+-}(r)]$, for various electrolytes over a wide range of salt concentrations.

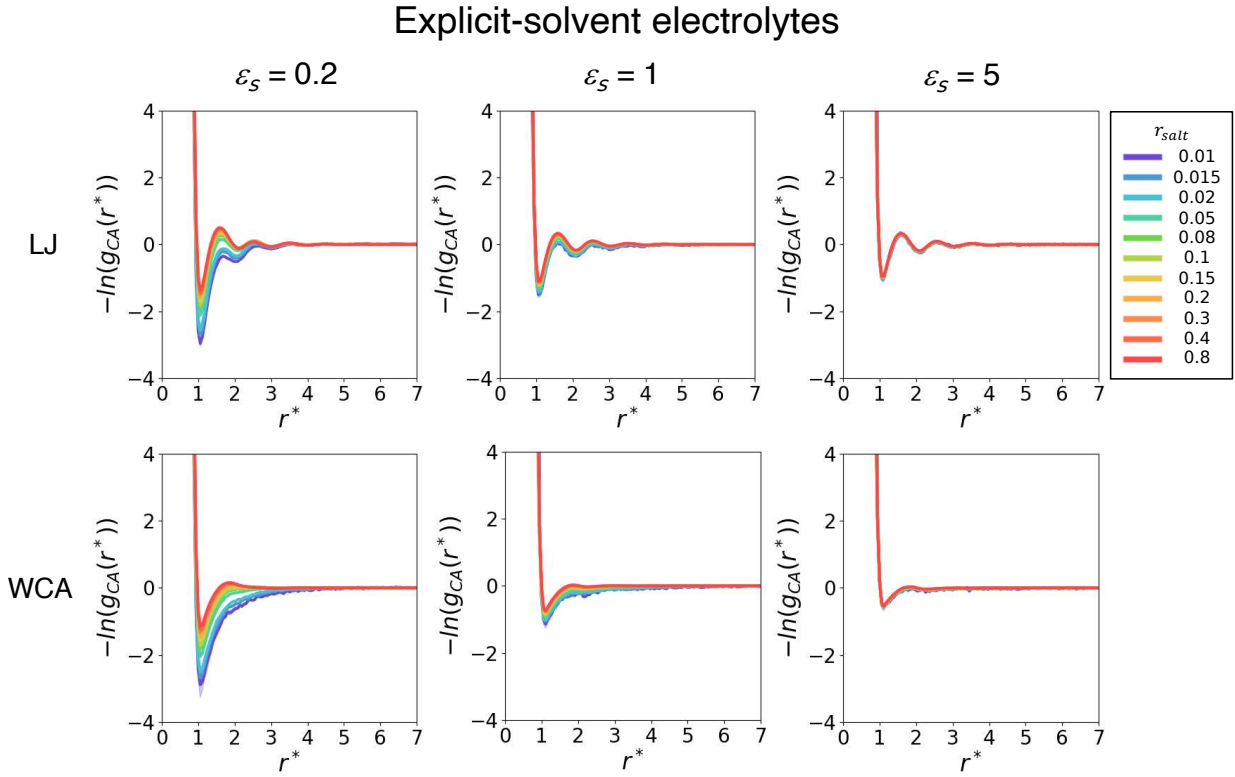


FIG. S14. Potential of mean force between cations and anions, $\beta w_{+-}(r) = -\ln[g_{+-}(r)]$, for explicit-solvent LJ and WCA electrolytes at various ϵ_s .

Implicit-solvent electrolytes

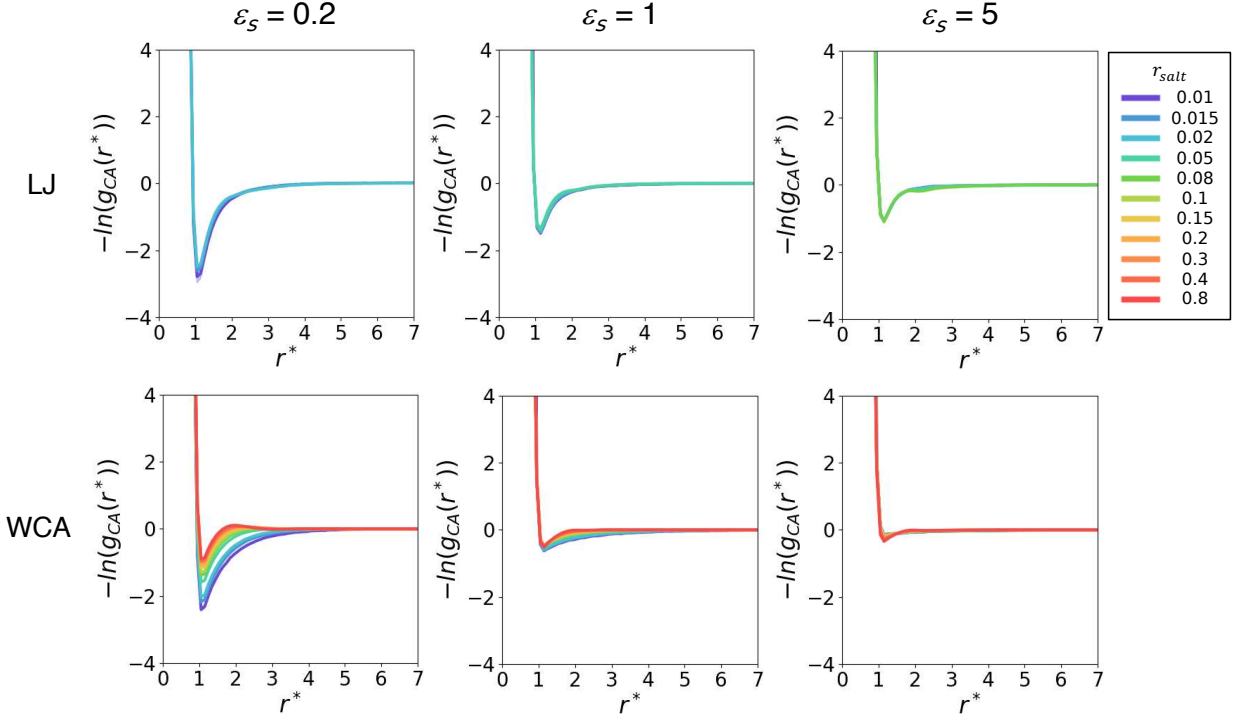


FIG. S15. Potential of mean force between cations and anions, $\beta_{W+-}(r) = -\ln[g_{+-}(r)]$, for implicit-solvent LJ and WCA electrolytes at various ϵ_s . The implicit-solvent electrolytes, exhibiting the phase segregation, are excluded.

S7. FITTING RESULTS OF MEAN-SQUARED DISPLACEMENT FOR IONS AND SOLVENT

This section presents the fitting results of the mean-squared displacement (MSD) of both ions and solvent, from which the corresponding diffusion coefficients are obtained.

A. Explicit-solvent electrolytes

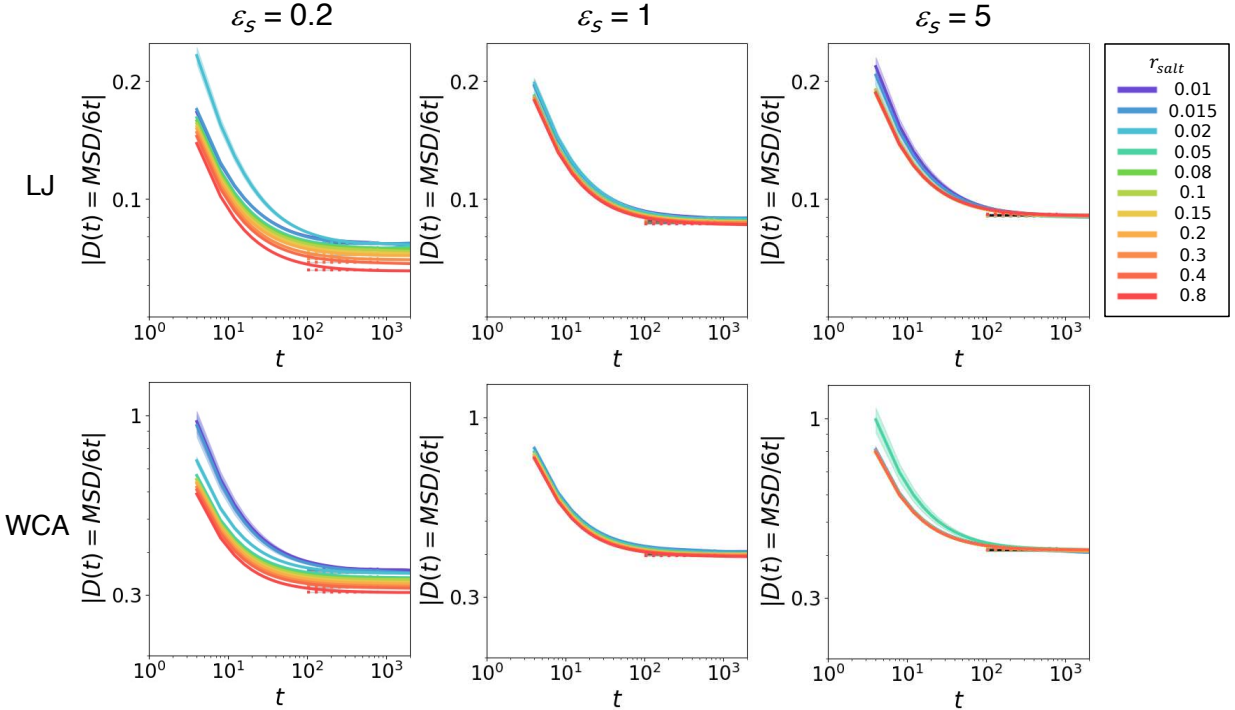


FIG. S16. Mean-squared displacement of cations in explicit-solvent electrolytes at various ϵ_s . Top and bottom rows show the results for LJ and WCA systems, respectively. Horizontal lines indicate the diffusion coefficients extracted from the linear-regime fitting within a time interval of [100,800].

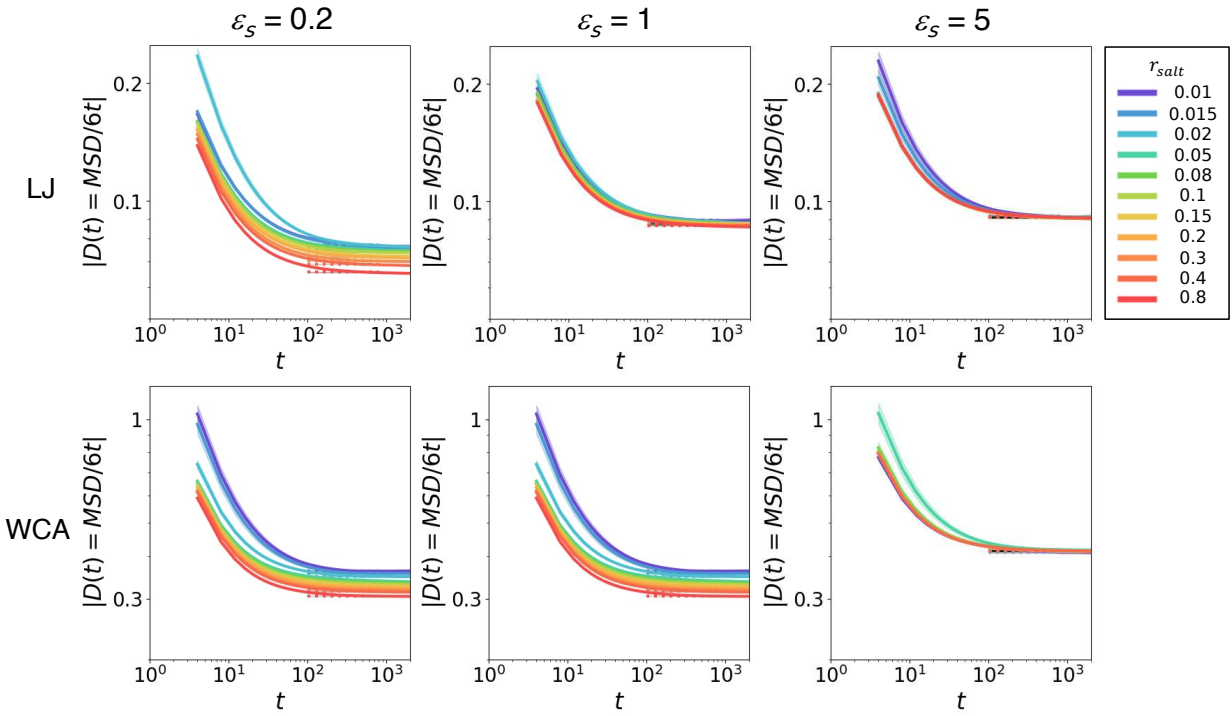


FIG. S17. Mean-squared displacement of anions in explicit-solvent electrolytes at various ε_s . Top and bottom rows show the results for LJ and WCA systems, respectively. Horizontal lines indicate the diffusion coefficients extracted from the linear-regime fitting within a time interval of [100,800].

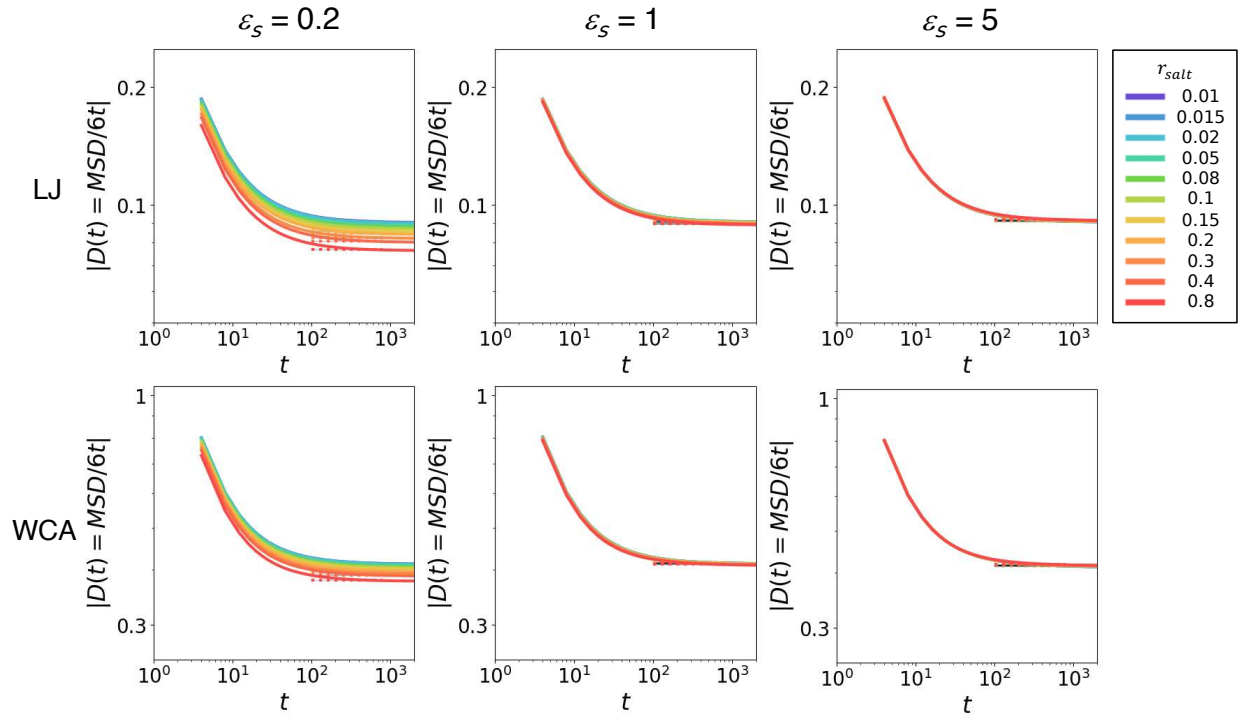


FIG. S18. Mean-squared displacement of solvent in explicit-solvent electrolytes at various ε_s . Top and bottom rows show the results for LJ and WCA systems, respectively. Horizontal lines indicate the diffusion coefficients extracted from the linear-regime fitting within a time interval of [100,800].

	$\varepsilon_s = 0.2$	$\varepsilon_s = 1$	$\varepsilon_s = 5$
LJ, explicit	■	▲	●
WCA, explicit	□	△	○

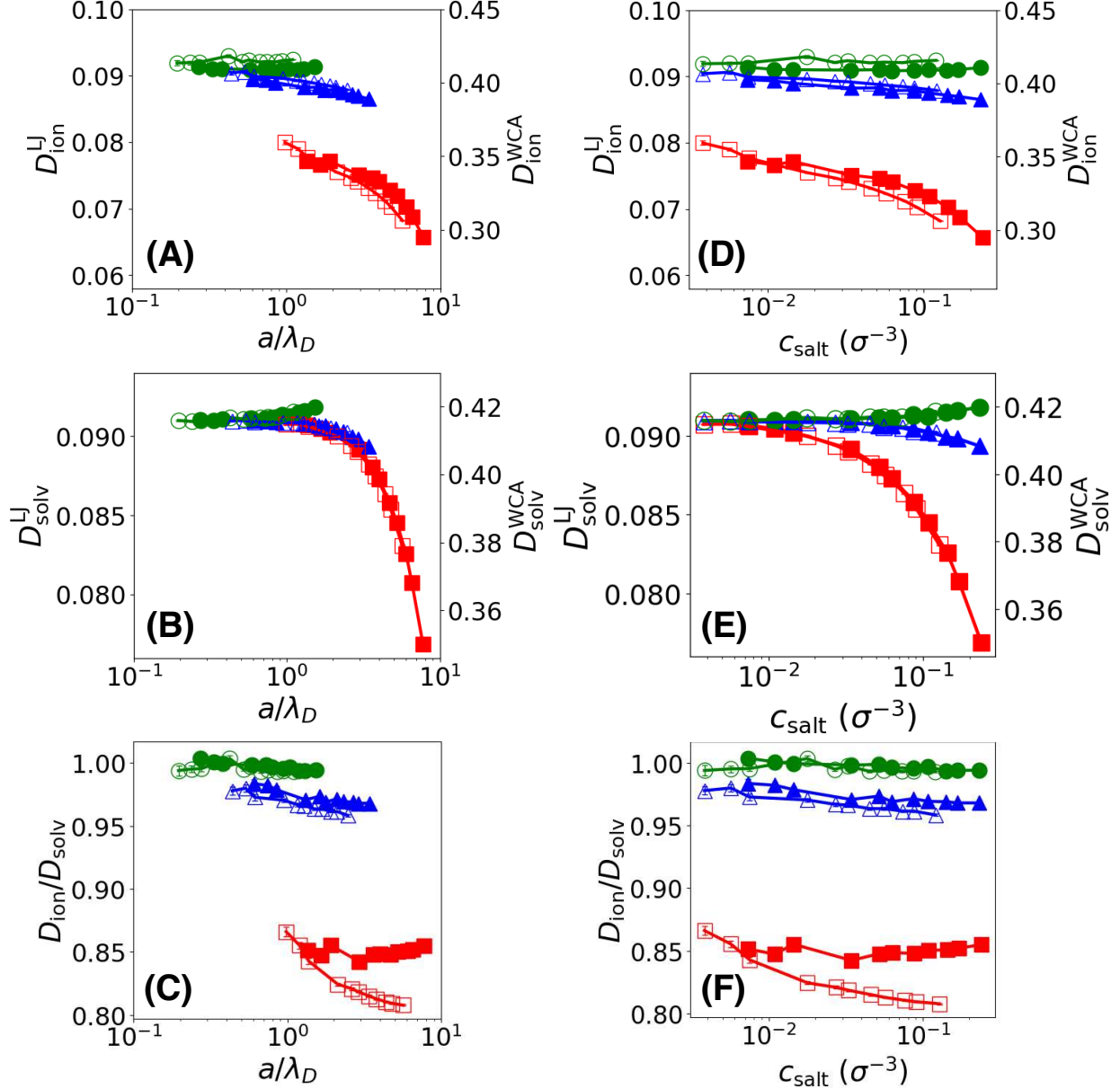


FIG. S19. Diffusion coefficients in explicit-solvent LJ and WCA electrolytes at various ε_s . (A, D) Ion diffusion coefficient, D_{ion} . (B, E) Solvent diffusion coefficient, D_{solv} . (C, F) The ratio $D_{\text{ion}}/D_{\text{solv}}$. Left and right columns show the result as a function of a/λ_D and c_{salt} , respectively.

B. Implicit-solvent electrolytes

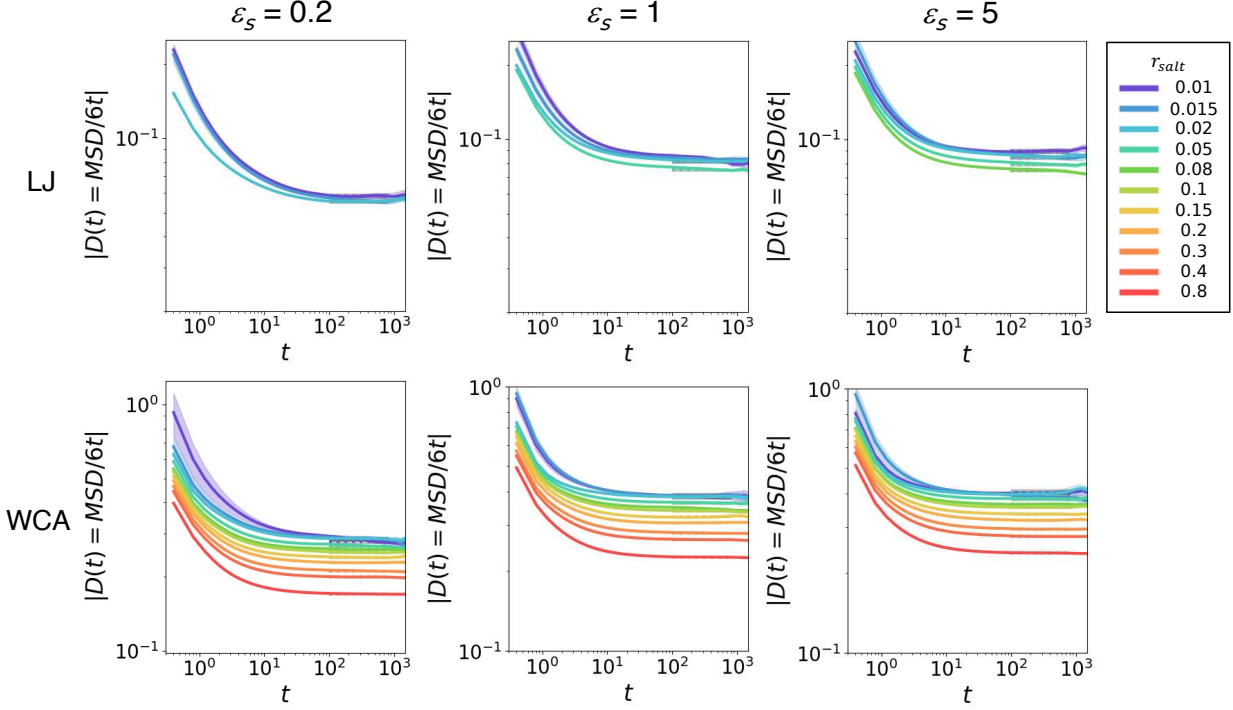


FIG. S20. Mean-squared displacement of cations in implicit-solvent electrolytes at various ϵ_s . Top and bottom rows show the results for LJ and WCA systems, respectively. Horizontal lines indicate the diffusion coefficients extracted from the linear-regime fitting within a time interval of [100,800].

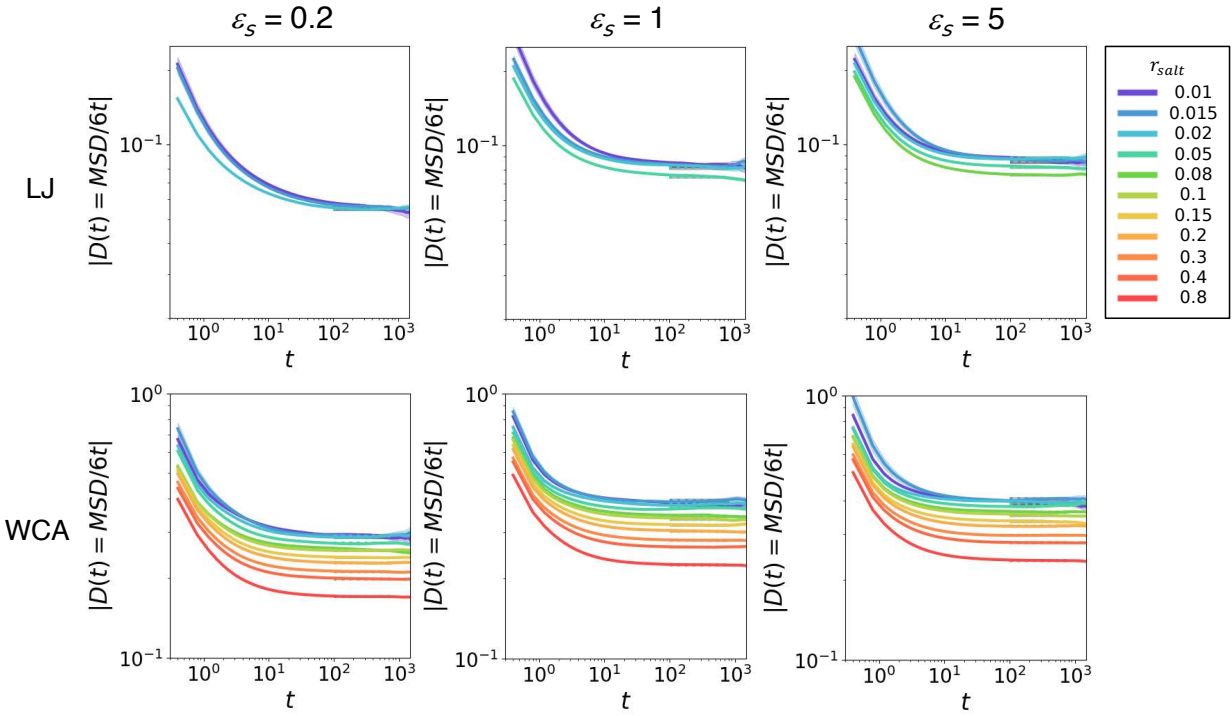


FIG. S21. Mean-squared displacement of anions in implicit-solvent electrolytes at various ϵ_s . Top and bottom rows show the results for LJ and WCA systems, respectively. Horizontal lines indicate the diffusion coefficients extracted from the linear-regime fitting within a time interval of [100,800].

	$\varepsilon_s = 0.2$	$\varepsilon_s = 1$	$\varepsilon_s = 5$
LJ, explicit	■	▲	●
WCA, explicit	□	△	○
LJ, implicit	■	▲	●
WCA, implicit	□	△	○

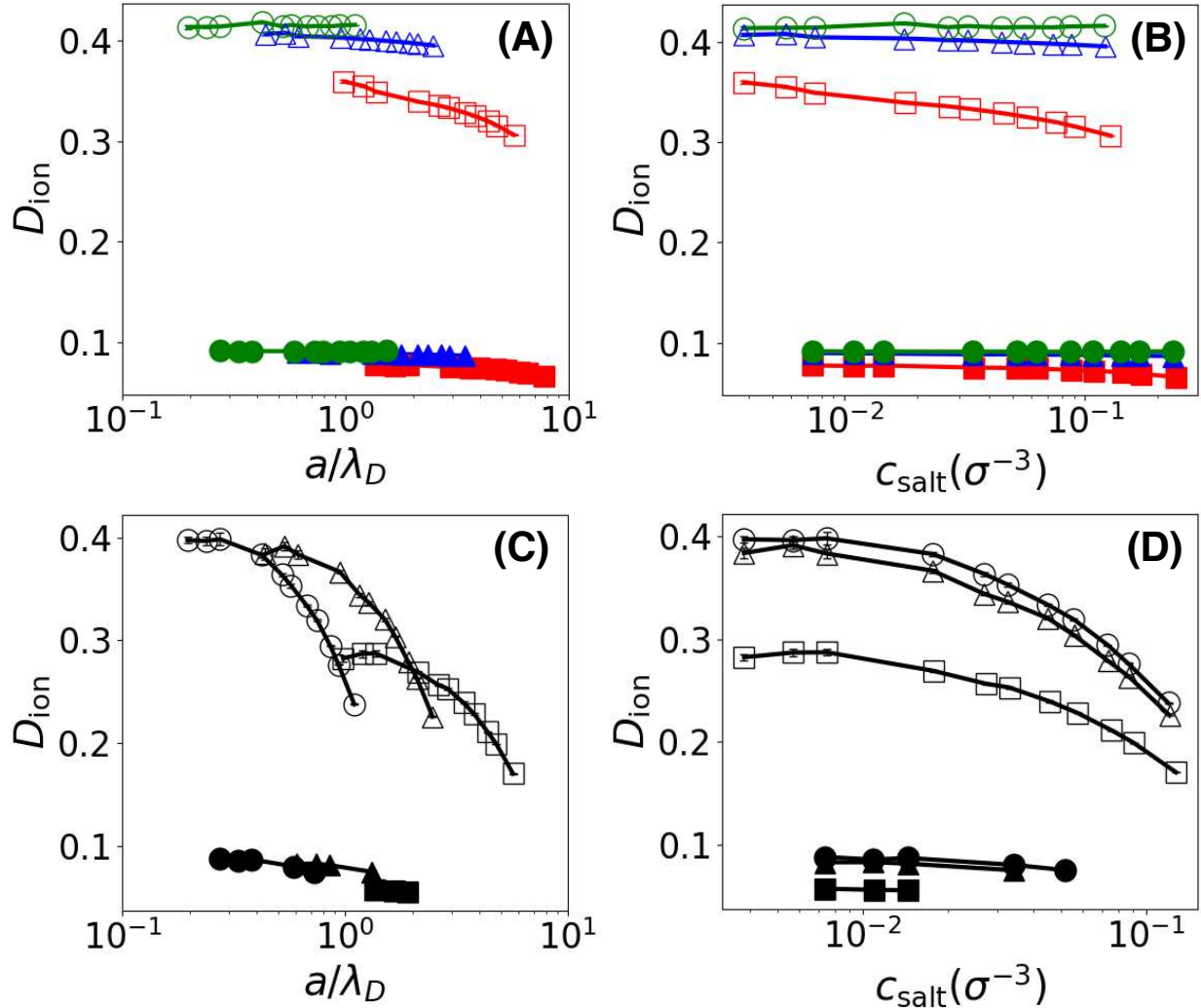


FIG. S22. Ion diffusion coefficient D_{ion} as a function of (A, C) a/λ_D , and (B, D) c_{salt} . Top and bottom rows show the results of explicit- and implicit-solvent electrolytes, respectively.

S8. FITTING RESULTS OF ION-PAIR SURVIVAL FUNCTION

This section presents the fitting results of the ion-pair survival function $H(t)$, from which the ion-pair lifetime τ_{pair} is obtained. Unlike other structural and dynamical quantities, $H(t)$ was computed using frequently saved trajectories.

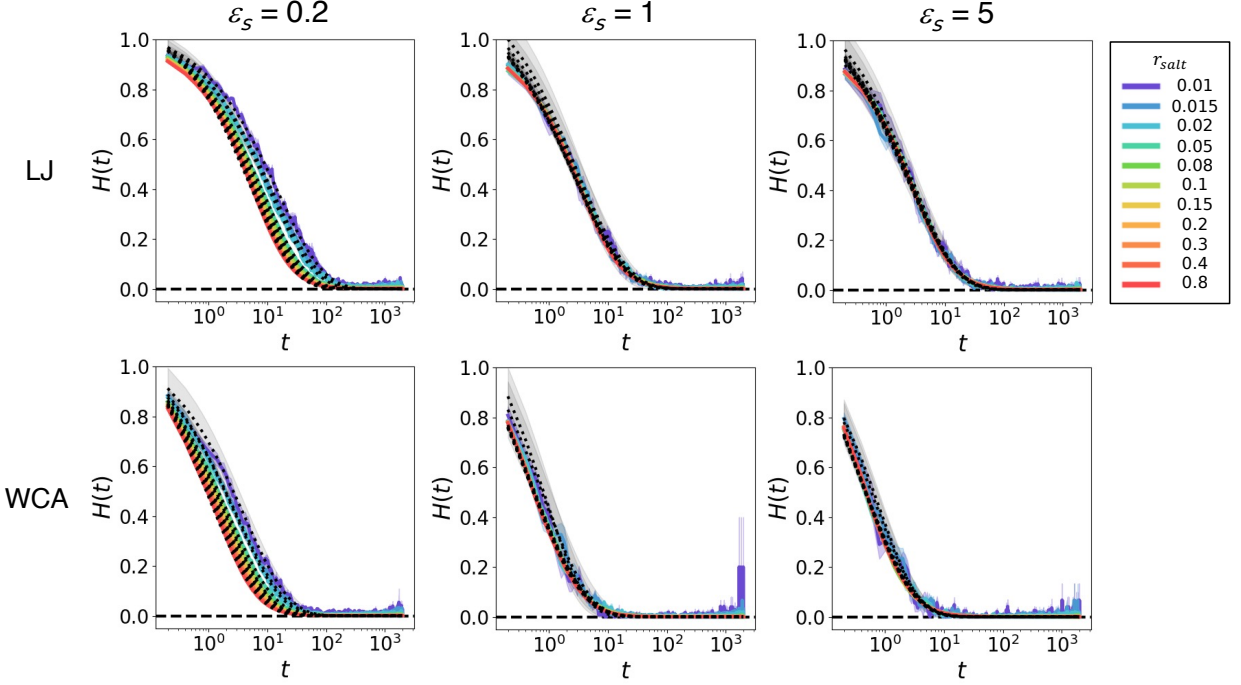


FIG. S23. Ion-pair survival function $H(t)$ (Eq. 10 in the main text) for explicit-solvent LJ and WCA electrolytes at various ε_s .

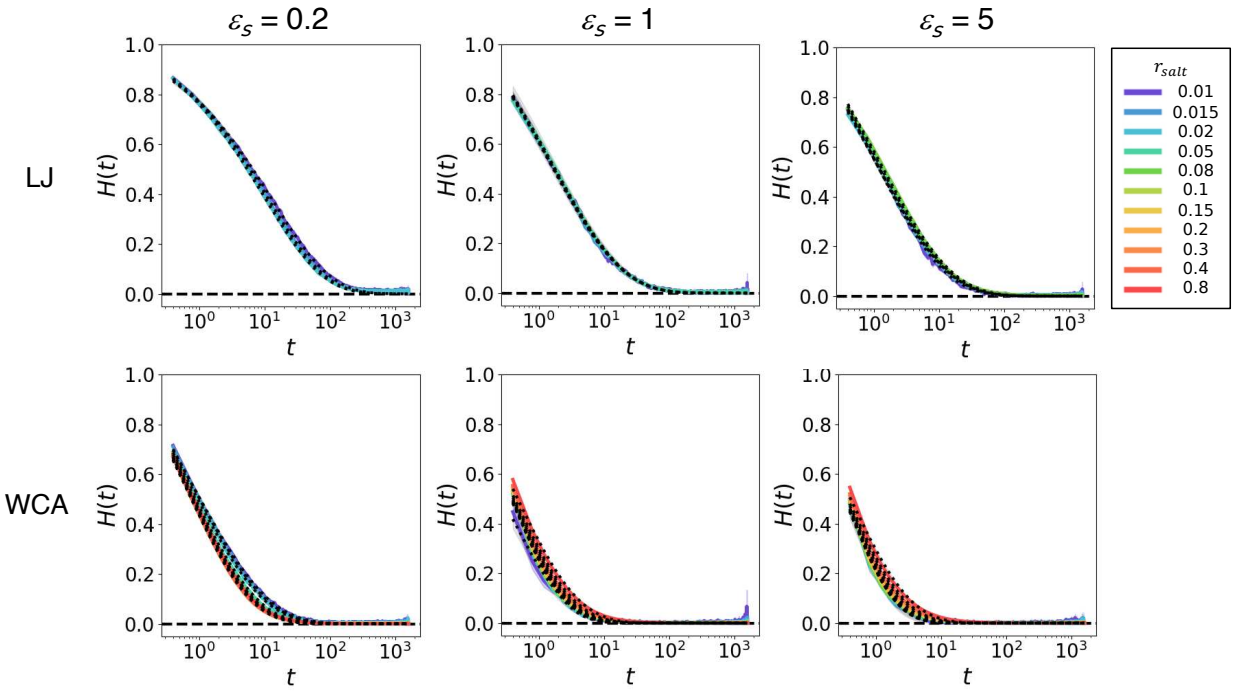


FIG. S24. Ion-pair survival function $H(t)$ (Eq. 10 in the main text) for implicit-solvent LJ and WCA electrolytes at various ϵ_s .

Explicit-solvent electrolytes

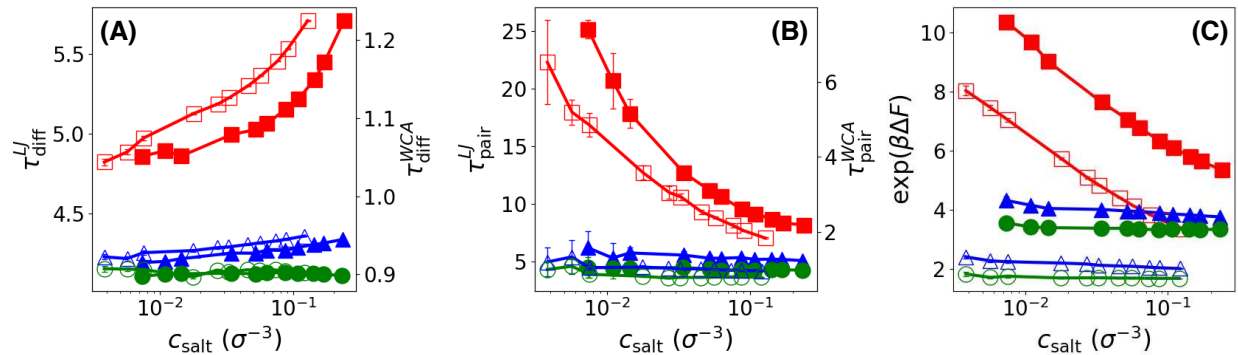


FIG. S25. Crossovers in ion dynamics and their structural origins as a function of the ratio c_{salt} across all electrolytes examined. (A, D) Diffusion relaxation time, τ_{Diff} . (B, E) Mean ion-pair lifetime, τ_{pair} . (C, F) Free-energy barrier for ion-counterion dissociation, $\beta\Delta F$. Panels (A–C) on the top row correspond to explicit-solvent models, while panels (D–F) on the bottom row correspond to implicit-solvent models. In panels (A–B) and (D–E), the left and right axes represent results for LJ (filled markers) and WCA (open markers), respectively.

S9. IONIC CONDUCTIVITY

We computed ion conductivity σ , which includes all dynamic correlations using the Onsager coefficients $\Delta\vec{r}_{\alpha\beta}$ [1, 2]. The mean-squared charge displacement Σ can be computed as follows:

$$\begin{aligned}\Sigma(t) &= \sum_{\alpha} \sum_{\beta} \frac{q_{\alpha}q_{\beta}}{\langle V \rangle k_B T} \Delta\vec{r}_{\alpha\beta}(t) \\ &= \frac{e^2}{\langle V \rangle k_B T} (\Delta\vec{r}_{++}(t) + \Delta\vec{r}_{--}(t) - 2\Delta\vec{r}_{+-}(t)) \\ &= \Sigma_{++}(t) + \Sigma_{--}(t) + \Sigma_{+-}(t) \\ &= \Sigma_{+}^s(t) + \Sigma_{+}^d(t) + \Sigma_{-}^s(t) + \Sigma_{-}^d(t) + \Sigma_{+-}(t).\end{aligned}\quad (\text{S1})$$

Here, the superscripts s and d denote the self and distinct part, respectively. In the long-time limit, $\Sigma(t)$ grow linearly with time t and its slope is the ionic conductivity, σ :

$$\sigma = \lim_{t \rightarrow \infty} \frac{\Sigma(t)}{6t}, \quad (\text{S2})$$

which includes all the contributions of the correlated motions. The ionic conductivity (σ) has its five contributions, as do the $\Sigma(t)$, $\Delta\vec{r}_{\alpha\beta}$ and $D_{\alpha\beta}$: $\sigma = \sigma_{+}^s + \sigma_{-}^s + \sigma_{+}^d + \sigma_{-}^d + 2\sigma_{+-}$.

$$\sigma = \sigma_{+}^s + \sigma_{-}^s + \sigma_{+}^d + \sigma_{-}^d + 2\sigma_{+-}. \quad (\text{S3})$$

That is, the delicate balance between those five components determine the overall conductivity σ .

Nernst-Einstein approximation. By neglecting all the correlations, only self-terms of Onsager coefficients contribute to the ionic conductivity under the Nernst-Einstein relation.

$$\begin{aligned}\sigma_{NE} &= \sigma_{+}^s + \sigma_{-}^s = \frac{e^2 \rho_{\text{ion}}}{k_B T} \left(\chi_{+} D_{+} + \chi_{-} D_{-} \right) \\ &= \frac{e^2 \rho_{\text{ion}}}{k_B T} D_{\text{ion}}.\end{aligned}\quad (\text{S4})$$

Here, $\rho_{\text{ion}} = (N_{+} + N_{-})/\langle V \rangle = 2N_{\text{salt}}/\langle V \rangle$, and $D_{\text{ion}} = \frac{1}{2}(D_{+} + D_{-})$. The contribution σ_{corr} of correlated motions to the ionic conductivity is $\sigma_{\text{corr}} = \sigma - \sigma_{NE}$ and the *ionicity* $\sigma/\sigma_{NE} = 1 + \sigma_{\text{corr}}/\sigma_{NE}$. σ_{corr} is usually negative as the dynamic correlations decrease σ .

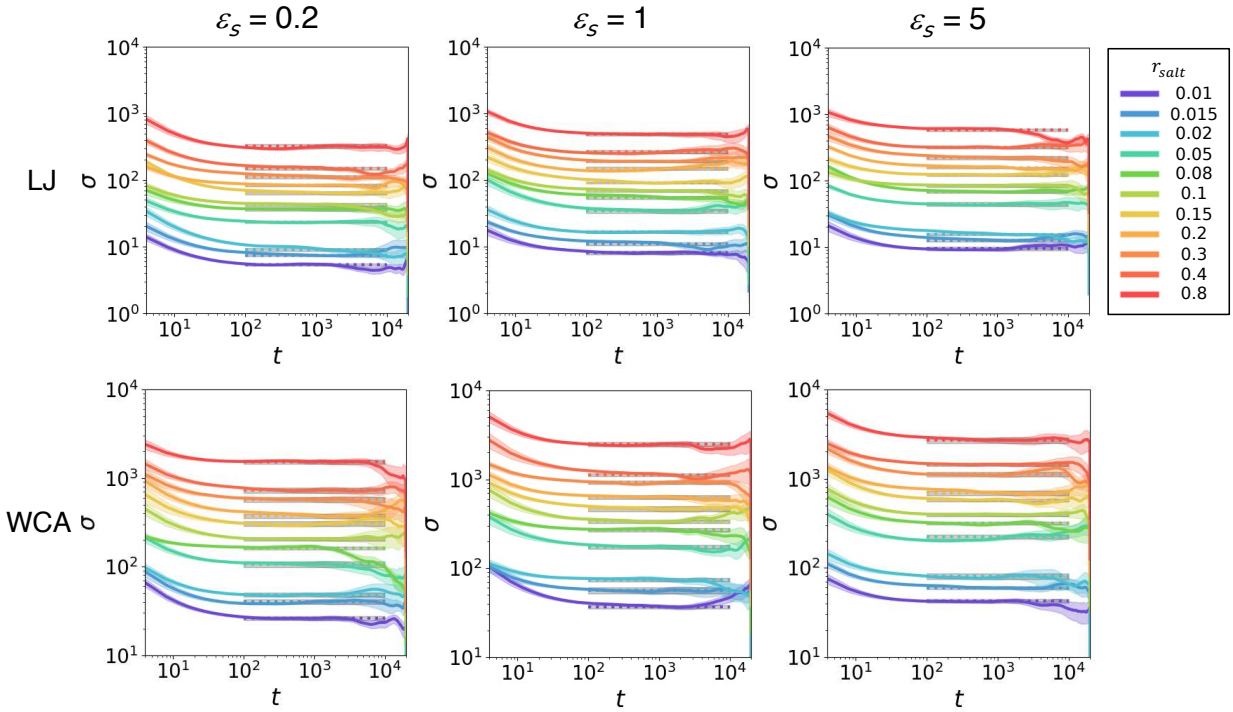


FIG. S26. Time-dependent ionic conductivity ($\sigma(t)$, Eq. S3) for both explicit-solvent LJ and WCA electrolytes with diverse ϵ_s . Horizontal lines indicate the ionic conductivity, extracted from the linear-regime fitting within a time interval of [300, 2000].

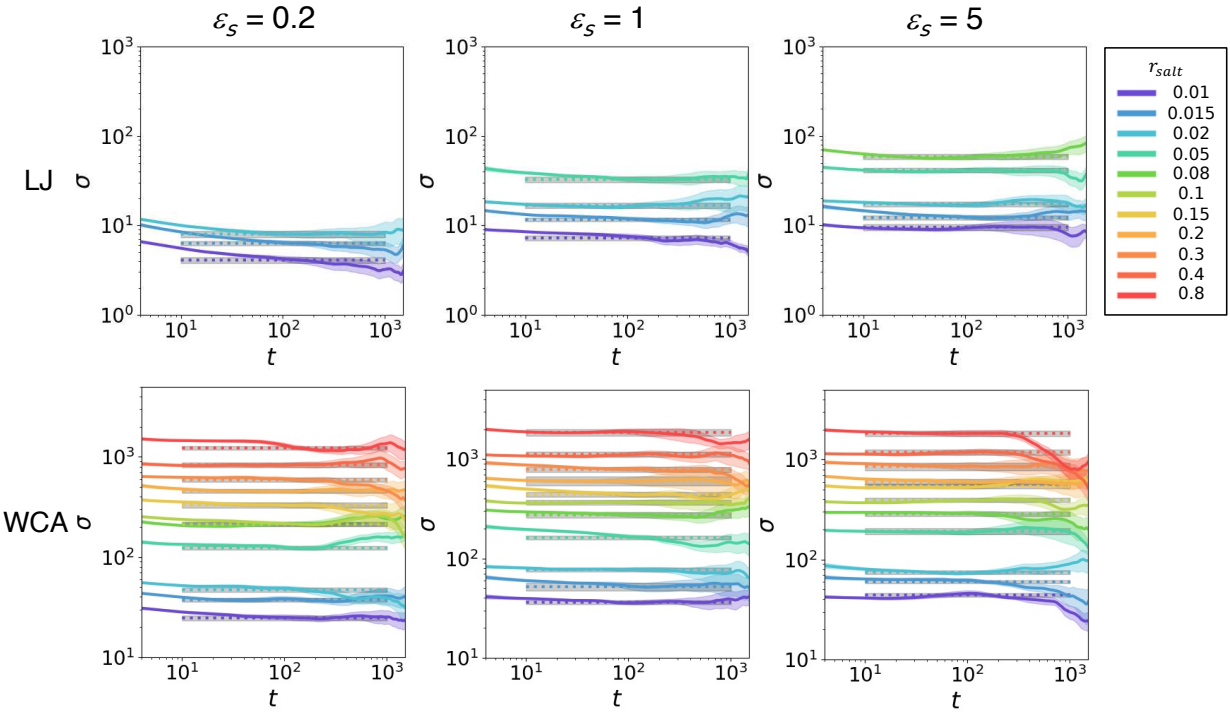


FIG. S27. Time-dependent ionic conductivity ($\sigma(t)$, Eq. S3) for both implicit-solvent LJ and WCA electrolytes with diverse ϵ_s . Horizontal lines indicate the ionic conductivity, extracted from the linear-regime fitting within a time interval of [20, 200].

	$\epsilon_s = 0.2$	$\epsilon_s = 1$	$\epsilon_s = 5$
LJ, explicit	■	▲	●
WCA, explicit	□	△	○
LJ, implicit	■	▲	●
WCA, implicit	□	△	○

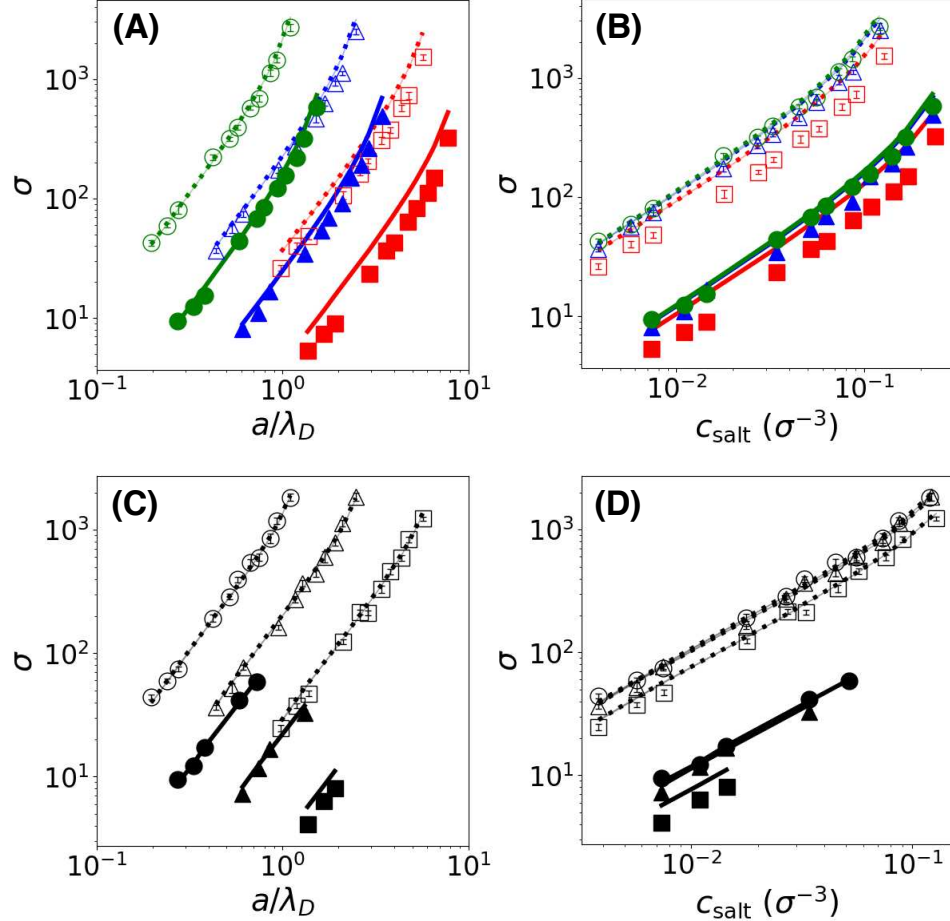


FIG. S28. Ionic conductivity (σ , markers) and its Nernst-Einstein (NE) approximation σ_{NE} (Eq. S4, dashed and solid lines) as a function of (A, C) a/λ_D and (B, D) c_{salt} . Top and bottom rows show the results of explicit- and implicit-solvent electrolytes, respectively.

	$\epsilon_s = 0.2$	$\epsilon_s = 1$	$\epsilon_s = 5$
LJ, explicit	■	▲	●
WCA, explicit	□	△	○
LJ, implicit	■	▲	●
WCA, implicit	□	△	○

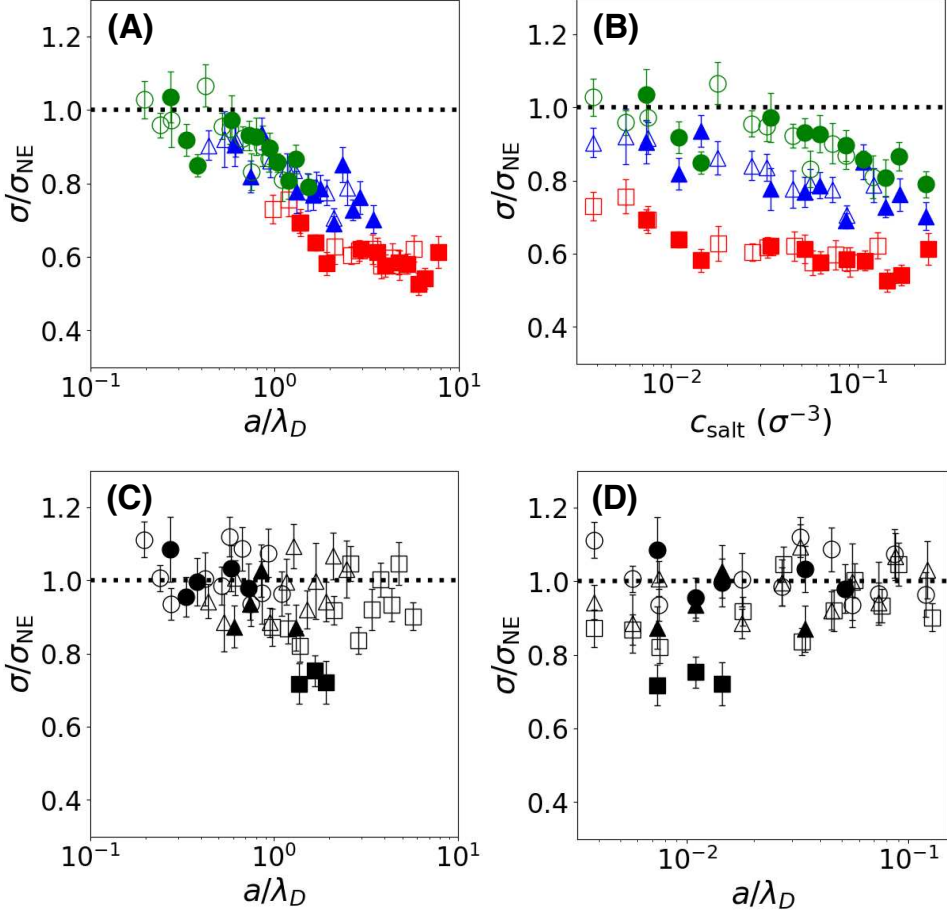


FIG. S29. Ionicity ($\sigma/\sigma_{\text{NE}}$) as a function of (A, C) a/λ_D and (B, D) c_{salt} . Top and bottom rows show the results of explicit- and implicit-solvent electrolytes, respectively.

S10. IONIC CLUSTER ANALYSIS: COMPARISON BETWEEN CAYLEY-TREE-BASED THEORY AND SIMULATION

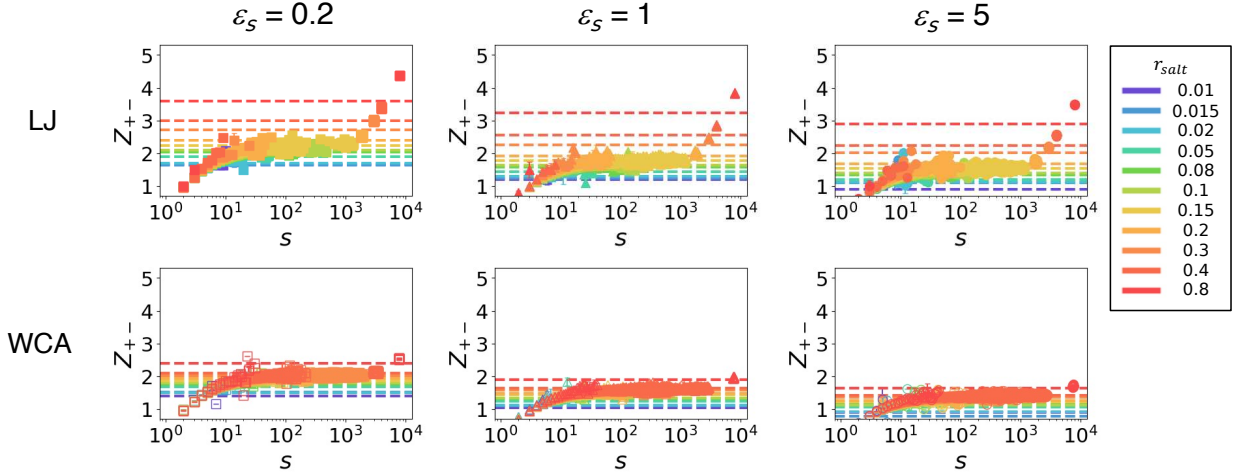
In this section, we provide a more detailed analysis of ionic clusters, focusing on ion association patterns and their comparison with the Cayley-tree-based mean-field theory proposed by McEldrew *et al.* [3–7]. Here, we focus in particular on the LJ and WCA electrolytes with $\epsilon_s = 0.2$, where the degree of ionic association exhibits a clear dependence on the salt concentration c_{salt} . In contrast, for systems with $\epsilon_s = 1$ and 5, we observe ion association that is independent of c_{salt} (Fig. S30). This behavior clearly violates the assumptions of speciation and strong dynamical correlations among ions within aggregates, thereby limiting the applicability of such Cayley-tree-based mean-field theories in these cases. We therefore exclude these systems from the analysis below.

A. Ion association patterns

The counterion association patterns suggest that the ionic clusters are initially tree-like and evolve into more highly branched networks with weak loop formation. Figure S30 shows the number Z_{+-} of cation-anion associations for individual ionic clusters. The ions are considered associated if their ionic distance is less than a cutoff distance of 1.5σ , as was used in defining ionic clusters in the original manuscript. We find that Z_{+-} depends on the cluster size s , taking values approximately between 1 and 4. In small clusters, Z_{+-} increases with s , while it exhibits a plateau at $Z_{+-} \approx 2$ over a broad intermediate range of cluster size ($10 \lesssim s \lesssim 10^3$). For the largest clusters, Z_{+-} increases again, which implies the order formation as for NaCl electrolytes [8].

In addition, we find clear deviations from the Cayley-tree assumption in the ionic gelation theory: (i) the presence of co-ion association and (ii) the formation of intra-cluster loops. We observe that a comparable number of co-ion associations emerges within each ionic cluster (Fig. S30), highlighting the non-counterion associations in our charge-symmetric simple electrolytes. We also observe that the ionic clusters form intra-cluster loops, whose number increases with increasing c_{salt} (Fig. S31). For each cluster, the number L of intra-cluster loops was computed from simulations: $L = E - s + 1$, where s is the number of constituent ions within a cluster, and E is the number of edges ($Z = 2E/s$). The increasing $\langle L/E \rangle$ indicates the increasing contribution of co-ion associations in an ionic cluster (Fig. S31(A,D)). Equivalently, we also computed the clus-

Counterion association



Co-ion association

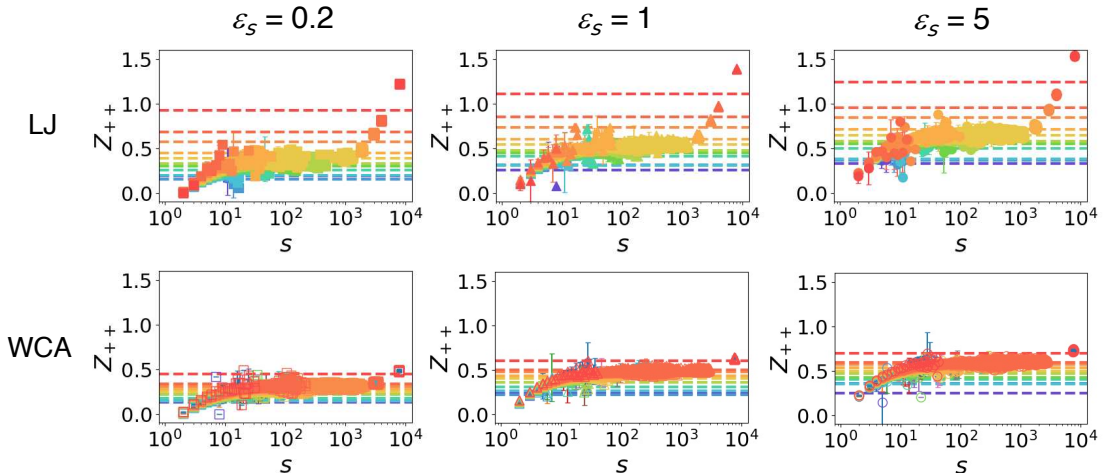


FIG. S30. The counterion association number Z_{+-} for individual ionic clusters in the LJ and WCA electrolytes with explicit solvent. Top and bottom rows show the simulation results accounting for only counterion associations and for co-ion associations, respectively. From left to right, panels correspond to different values of $\epsilon_s = 0.2, 1$, and 5 . Dotted horizontal lines represent the averaged association numbers at each salt concentration.

ter bond density (CBD) $\langle E/s \rangle$ for all ionic clusters (Fig. S31(B-C,E-F)). For ideal Cayley trees, $E/s = 1 - 1/s$ with $L = 0$, and it converges to 1 for large ionic clusters. However, our computation reveals that $\langle E/s \rangle \approx 1.3 - 1.5$, exceeding $1 - 1/s$ even for moderate-size ionic clusters, indicating that they contain intra-cluster loops, being more ordered than ideal Cayley trees. The computed CBD values below the gel point are comparable to those previously reported for NaTFSI elec-

trolytes [7].

Thus, these discrepancies clearly indicate the emergence of nontrivial association patterns ignored in the theory, such as intra-cluster loops [3, 6, 7] and more complex connectivity within ionic aggregates. Similar results were obtained using the counter-ion associations (Fig. S31(B-C)), despite slightly lower gelation thresholds with decreased CBD values (Tab. S2). Consequently, the ionic aggregates are better described as branched, weakly looped ionic networks rather than ideal loop-free Cayley-tree structures.

System	ϵ_s	$c_{\text{gel}} (\sigma^{-3})$	$\gamma_s(c_{\text{gel}}) (\sigma)$
LJ	0.2	0.088	1.85 ± 0.01
WCA	0.2	0.076	1.97 ± 0.01

TABLE S2. Formation of a percolating ionic network near the gelation point c_{gel} in the explicit-solvent electrolytes, accounting only for counterion associations. The exponent $\gamma_s(c_{\text{gel}})$ quantifies the power-law tail of the size distribution, $P(s)$ (see Eq. 9 in the main text).

B. Comparison of ionic association between theory and simulations

Owing to the discrepancies found in the ionic associations, our charge-symmetric solvent primitive models, unlike bulky and asymmetric ionic compounds such as LiTFSI, are not expected to quantitatively follow the ionic gelation theory proposed by McEldrew *et al.* [3, 5], which is based on Cayley-tree-like clusters. In addition, the simplicity of our model, which employs isotropic interaction potentials between all ions and solvent particles, further raises ambiguities in defining the ion-association functionality. Indeed, it has also been shown that simple electrolytes such as NaCl clearly deviate from Cayley-tree-based ionic gelation predictions due to the formation of ordered, loop-rich aggregates [3, 5]. In our case, as shown below, the theory captures the counterion association constant below the gelation point reasonably well, yielding values of comparable order of magnitude to those observed in simulations when an appropriate ion-association functionality is chosen. However, it does not accurately locate the gelation threshold over the estimated range of ion-association functionality.

For comparison with the theory, it is necessary to estimate a single ion-association functionality f that characterizes tree-like, loop-free aggregates at the mean-field level. In this analysis, we focus on the counterion-association functionality f_{+-} ; due to the charge symmetry, the cations

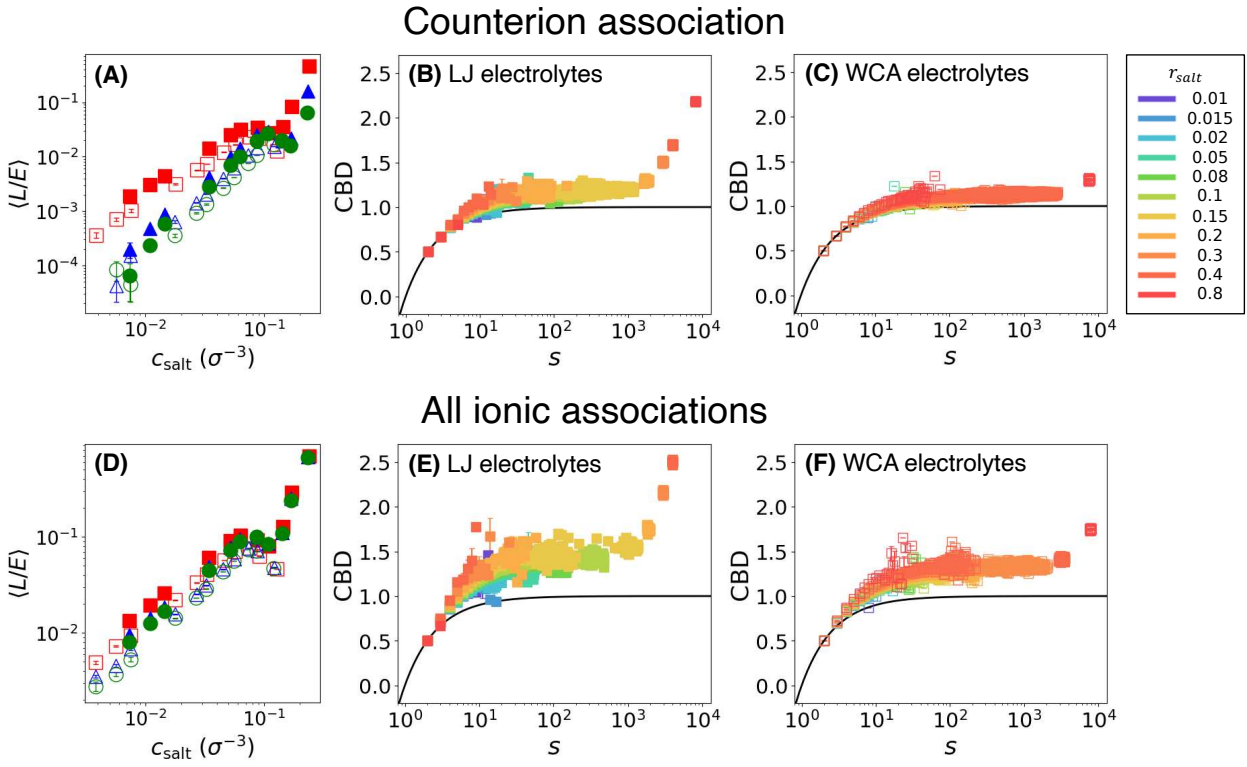


FIG. S31. Quantitative analysis of loop formation in ionic clusters for the LJ and WCA electrolytes with explicit solvent. Top and bottom rows show the simulation results accounting for only counterion associations and for all ionic associations, respectively. (A, D) The relative number $\langle L/E \rangle$ of intra-cluster loops normalized by the total number of edges, averaged over all ionic clusters. (B, C) The cluster bond density (CBD) as a function of cluster size s , accounting for only counterion associations. (E, F) The CBD as a function of cluster size s , accounting for all ionic associations, including co-ion associations. The CBD carries information equivalent to $\langle L/E \rangle$; results for $\epsilon_s = 0.2$ are shown here. In panels (B-C) and (E-F), black solid lines represent the prediction for ideal Cayley-tree clusters (i.e., $CBD = 1 - 1/s$). Filled and open markers correspond to the LJ and WCA electrolytes, respectively. In panels (A, D), colors indicate different values of ϵ_s : red squares for 0.2, blue triangles for 1, and green squares for 5.

and anions share the same functionality. As mentioned above, there are ambiguities in defining f_{+-} due to the simplicity of our model, which employs isotropic interaction potentials between all ions and solvent particles. Here, we estimate an appropriate range of f_{+-} from the simulations using two independent approaches, both yielding a consistent range of values: $f_{+-} \approx 2 - 5$.

First, according to the mean-field theory, the average counterion-association number $\langle Z_{+-} \rangle$

determines f_{+-} via

$$\langle Z_{+-} \rangle^* = \frac{f_{+-}}{f_{+-} - 1}, \quad (S5)$$

where the asterisk denotes the gel point. For both LJ and WCA electrolytes with $\epsilon_s = 0.2$, $\langle Z_{+-} \rangle^* \approx 1.85$ (Fig. S32(A,E)). This value suggests an estimated functionality in the range $f_{+-} \approx 2$ to 5, corresponding to $\langle Z_{+-} \rangle^* \approx 2 - 1.5$. Second, we estimated f_{+-} using the number of ionic neighbors within the first solvation shell. The cumulative counter ion-pair distributions $c_{CA}(r)$, evaluated at the cutoff distance $r_{cut} = 1.5\sigma$, indicate that the number of counterions is $N_{+-} \approx 4$ for the LJ electrolytes and $N_{+-} \approx 2$ for the WCA electrolytes with $\epsilon_s = 0.2$ at the highest c_{salt} investigated. Another parameter used to estimate the ionic association constant λ is the counterion-association probability p_{+-} . This probability is concentration-dependent and can be estimated from the simulations as $p_{+-} = \langle Z_{+-} \rangle / f_{+-}$. For the charge-symmetric electrolytes considered in this work, the theoretical relation reads:

$$\lambda_{th}\zeta = \frac{p_{+-}^2}{(1 - p_{+-})(1 - p_{+-})}, \quad (S6)$$

where $\zeta = f_{+-}p_{+-}c_{salt}$. We note that the definitions of f_{+-} and p_{+-} used in our analysis differ from those of McEldrew *et al.* [5]; in particular, the subscripts here do not imply directionality or asymmetry. From the simulations, the computed association constant λ_{sim} is estimated from the minimum value F_{min} of the cation-anion potential of mean force (see Fig. 4 in the main text) via $\lambda_{sim} = e^{-\beta F_{min}}$. The gelation point c_{gel} is then estimated using the relation:

$$p_{+-}(c_{gel}) = \frac{\langle Z_{+-} \rangle^*}{f_{+-}} = \frac{1}{f_{+-} - 1}. \quad (S7)$$

We find reasonably good agreement between the theoretical and simulated ionic association constants below the gelation threshold for appropriate choices of the functionality, namely $f_{+-} = 4$ (LJ electrolytes) and $f_{+-} = 5$ (WCA electrolytes) (Fig. S32(C, G)). However, the theory cannot predict the gelation threshold, which is expected given that discrepancies in the aggregation patterns emerge with increasing salt concentration.

Similar limitations of the Cayley-tree-based ionic gelation theory have been reported previously. For example, the gelation points predicted by the Cayley-tree-based ionic gelation theory were found to be systematically lower than those estimated from simulations for nonaqueous LiPF₆ and LiBF₄ electrolytes [5]. This discrepancy was attributed to the fact that the ionic clusters in these systems do not strictly satisfy the Cayley tree assumption, owing to the formation

of intra-cluster loops that suppress ideal tree-like associations. In our primitive solvent models, such deviations are even more pronounced, due to the isotropic interionic interactions and the enhanced formation of intra-cluster loops. Consequently, the gelation thresholds predicted by the Cayley-tree-based theory exhibit substantially larger deviations from our simulation results.

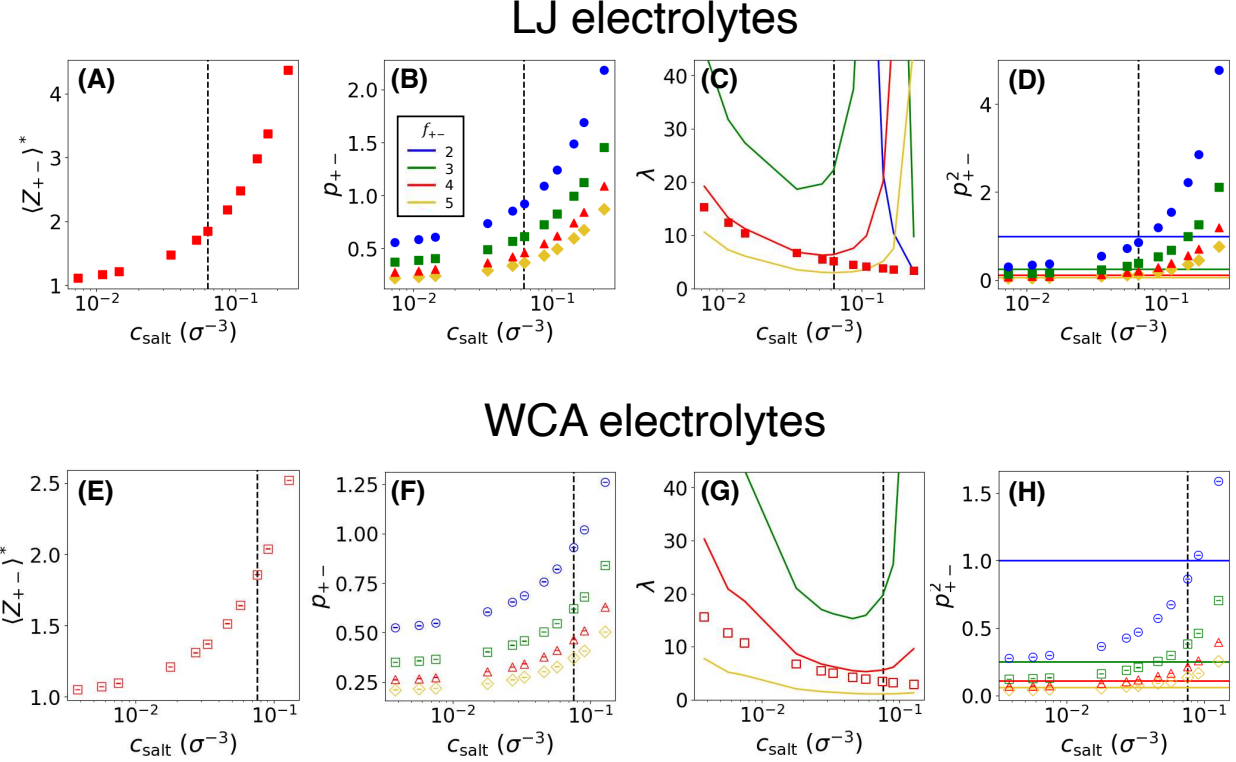
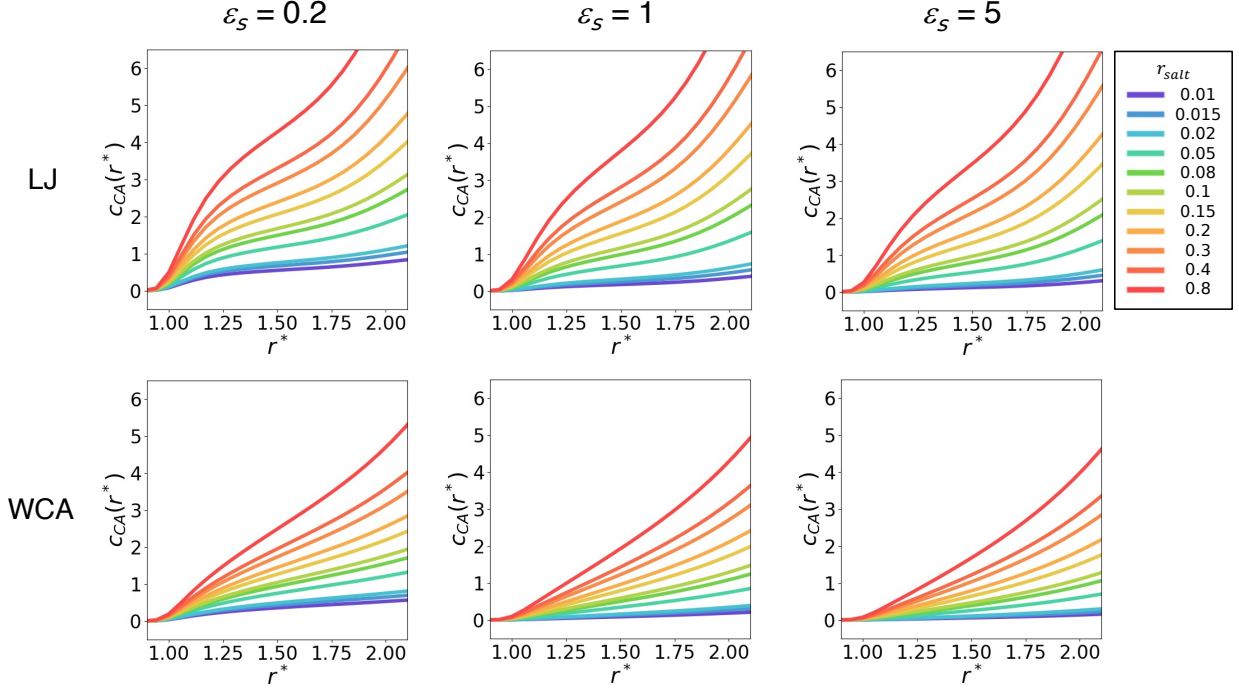


FIG. S32. Comparison of ionic association between theory [3, 5] and simulations for both LJ and WCA electrolytes with $\epsilon_s = 0.2$. The top and bottom rows show the simulation results for the LJ and WCA electrolytes, respectively. (A, E) The counterion association number Z_{+-}^* . (B, F) The corresponding association probability p_{+-} for different values of f_{+-} . (C, G) The ionic association constant λ . (D, H) The squared counterion association probability p_{+-}^2 with the theoretical predictions at the gel point, indicated by the horizontal solid lines. In panels (B-D, F-H), symbols represent simulation results, and different colors denote different values of f_{+-} . In all panels, vertical black dotted lines indicate the gel point estimated from simulations (see Tab. I in the main text).

Counterion association



Co-ion association

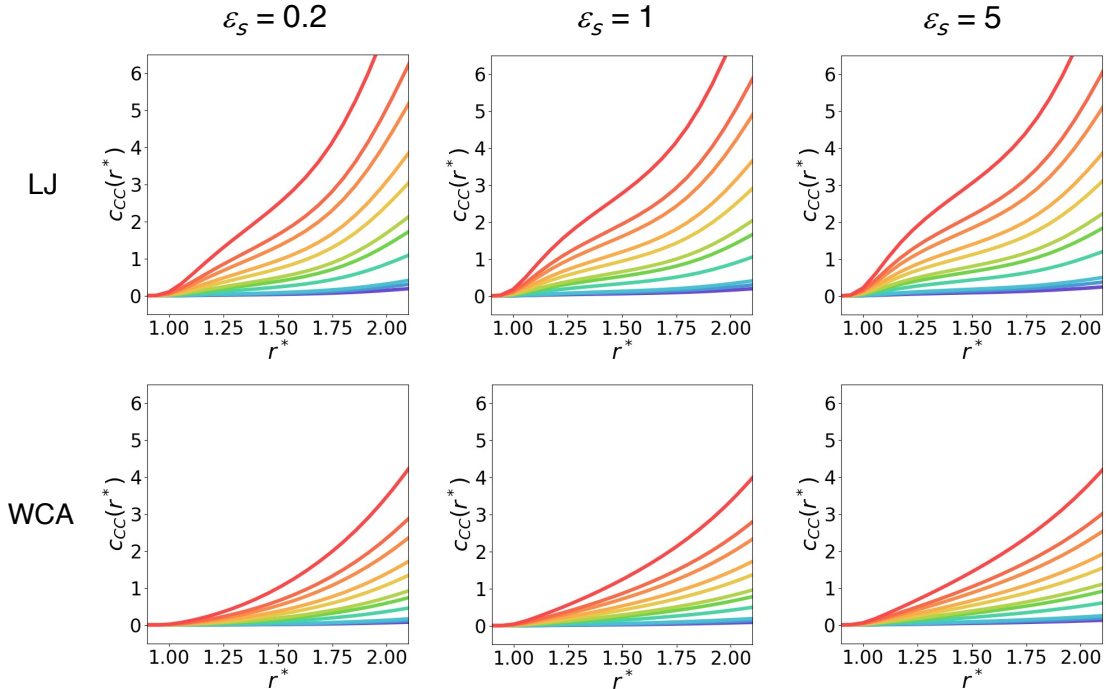


FIG. S33. The cumulative distribution for counterion $c_{CA}(r)$ and co-ion associations $c_{CC}(r)$. The top and bottom rows show the simulation results for the LJ and WCA electrolytes, respectively. From left to right, panels correspond to different values of $\epsilon_s = 0.2, 1$, and 5 . Owing to the charge symmetry, cation-cation associations are only considered here.

- [1] K. D. Fong, J. Self, B. D. McCloskey, and K. A. Persson, Ion correlations and their impact on transport in polymer-based electrolytes, *Macromolecules* **54**, 2575 (2021).
- [2] K. D. Fong, J. Self, B. D. McCloskey, and K. A. Persson, Onsager transport coefficients and transference numbers in polyelectrolyte solutions and polymerized ionic liquids, *Macromolecules* **53**, 9503 (2020).
- [3] M. McEldrew, Z. A. Goodwin, S. Bi, M. Z. Bazant, and A. A. Kornyshev, Theory of ion aggregation and gelation in super-concentrated electrolytes, *J. Chem. Phys.* **152**, 234506 (2020).
- [4] M. McEldrew, Z. A. Goodwin, H. Zhao, M. Z. Bazant, and A. A. Kornyshev, Correlated ion transport and the gel phase in room temperature ionic liquids, *J. Phys. Chem. B* **125**, 2677 (2021).
- [5] M. McEldrew, Z. A. Goodwin, N. Molinari, B. Kozinsky, A. A. Kornyshev, and M. Z. Bazant, Salt-in-ionic-liquid electrolytes: Ion network formation and negative effective charges of alkali metal cations, *J. Phys. Chem. B* **125**, 13752 (2021).
- [6] Z. A. Goodwin, M. McEldrew, B. Kozinsky, and M. Z. Bazant, Theory of cation solvation and ionic association in nonaqueous solvent mixtures, *Phys. Rev. X Energy* **2**, 013007 (2023).
- [7] X. Zhang, Z. A. Goodwin, A. G. Hoane, A. Deptula, D. M. Markiewitz, N. Molinari, Q. Zheng, H. Li, M. McEldrew, B. Kozinsky, *et al.*, Long-range surface forces in salt-in-ionic liquids, *ACS Nano* **18**, 34007 (2024).
- [8] J.-H. Choi, H. R. Choi, J. Jeon, and M. Cho, Ion aggregation in high salt solutions. vii. the effect of cations on the structures of ion aggregates and water hydrogen-bonding network, *J. Chem. Phys.* **147**, 154107 (2017).